Materials and Interfaces to Enable Reversible Mg Electrochemistry for Energy Storage Applications

Thesis by
Steven Hartzel Stradley

In Partial Fulfillment of the Requirements for the
Degree of
Doctor of Philosophy in Chemical Engineering

CALIFORNIA INSTITUTE OF TECHNOLOGY
Pasadena, California

2025
Defended 23 January 2025

Steven Hartzel Stradley
ORCID: 0009-0009-7154-608X

ACKNOWLEDGEMENTS

The course of earning a PhD brings soaring highs and crushing lows. Like all others who have taken this road, I would never have achieved such heights or survived the valleys without an extensive network of support. The following section details my inadequate acknowledgments for all of the people who truly made this work possible.

I'd like to start by thanking my family. I'd like to thank my parents, who worked tirelessly to support my education and who nurtured my early curiosity in topics and areas which were foreign to them. I was certainly not the easiest child to raise, but my parents provided a perfect example of the self sacrifice and care necessary to build a family. They each worked multiple jobs to afford my education, supported my extracurriculars and travels, denied luxuries for themselves, and loved me even when I did not express my love for them. I'd also like to thank my brother, my grandparents, my aunts, and my uncles for their tireless support and encouragement as they watched my blooming endeavors.

I'd like to thank my friends from undergrad who helped nurture a young Steven making his first independent steps in the world. Jesse, who I have known since grammar school, encouraged me to fearlessly embrace myself in a world which would have me be someone else. I'd like to thank my friends in chemical engineering, Monica, Kendal, Renee, Jess, Katie, Bretlyn, Zippy, and Melissa. From the countless nights spent working in the ChemE lounge or relaxing on Jess and Renee's couch, I would not have earned my degree or had nearly as much fun in college without my fellow ChemE girls.

My undergrad professors also played a key role in getting me to where I am today. I'd like to thank Professor Vijay John, who took a chance on an incoming undergrad freshman and gave me my first ever research experiences. Professor Anne Robinson mentored me throughout my senior years. Professor Katie Russell was the first person to tell me I would be a good fit for grad school at a time when I had never considered the possibility.

Next, I'd like to thank the people who supported me throughout grad school. Michelle, who began as a fellow rotator in the See Group, pierced my shell and became my first friend in grad school, my first ally in Mg electrochemistry, my roommate, my confidante, and my closest support during my lowest parts of grad

school. I can only hope to reciprocate the effort and care you have shown me. Brian, another early friend, stayed with me throughout the years. He showed me that I have a capacity for growth that I had never imagined. He was with me throughout the evolution of the misfit subgroup. Wendy provided tireless support and guidance in times when those were hard to come by. I'd also like to thank the rest of the See Group. I would not have had such a rewarding and productive graduate career if I was not surrounded by a group of such supportive and understanding people.

I'd like to thank my advisor, Professor Kimberly See. She took on a first year student with only minimal experience in electrochemistry and made me the scientist I am today. She taught me to formulate and evaluate hypotheses, to take a critical eye to the literature, and how to design studies to probe the mysteries of Mg. My PhD was full of bumps, but Kim stayed with me through them all.

I'd also like to thank my non See Group friends, Sarah, Chandler, and Ana. We shared unforgettable experiences on game shows, at puppet festivals, and throughout southern California. You kept me grounded as I dealt with some of the absurdities of electrochemistry.

Next, I'd like to thank my closest and most constant support, Hazel, my dog. Even on the most difficult of days, she embraced me with the most abundant joy a creature can manifest. Her propensity for love is an example for us all. Though not without stress, caring for Hazel has been one of the most rewarding experiences of my lifetime. She deserves all of the salmon in the world.

Finally, I'd like to thank my husband, Tony Lu. His love and understanding changed my life in ways I would never have thought possible. His support and point of view kept me going when times were tough. He gives me so many joyous moments to look forward to. I clearly lack the words to adequately express what he means to me. I cannot wait to see what the next chapters bring for us.

ABSTRACT

Climate change drives the need for a dramatically increased deployment of electric vehicles and intermittent renewable energy sources. Each of these depends intimately on batteries for range and reliability. Although Li-ion batteries are the current industry standard for electrochemical energy storage, they are based on scarce and unevenly distributed resources. It is thus crucial to develop rechargeable battery chemistries based on more energy dense and resource equitable materials. Orders of magnitude more abundant and energy dense than Li, Mg is an attractive alternative to Li for energy storage. Despite its many attractive properties, deployment of Mg-based chemistries is hindered by a lack of cathode, anode, and electrolyte materials which support Mg electrochemistry and are mutually compatible. This thesis endeavors to deploy new materials to sustain reversible Mg electrochemistry and to understand how certain material properties impact electrochemical performance. First, we investigate new cathode materials based on Earth-abundant transition metal chlorides. These cathodes cycle somewhat reversibly but are prone to rapid capacity fade due to active material dissolution and shuttle. We identify electrolyte modification as a means to combat this fade. Next, we characterize halide-free Mg electrolytes based on weakly coordinating Si-centered anions. These electrolytes display impressively high oxidative stabilities but also relatively high reductive overpotentials and a fatal vulnerability to passivation by H_2O. We then consider a class of electrolytes based on another weakly coordinating anion. These systems show exceptionally low reductive overpotentials among halide-free Mg electrolytes. We increase the bulk of the anion and correspondingly observe a slight increase in the reductive overpotential and an enhancement in rate performance. Finally, we deploy Al as an Earth-abundant, high capacity alloying anode for Mg-based batteries. Though the native kinetics for Mg-Al alloying prove too sluggish for practical systems, we use Bi to enhance the alloying kinetics of Al by two orders of magnitude. Though alloying capacity is limited by a large particle size, we present a viable method for enhancing Al alloying kinetics to relevant rates, thereby unlocking a highly desirable material for future studies. Taken together, this work expands the scope of cathode, electrolyte, and anode materials which support reversible Mg electrochemistry. Though imperfect, the lessons we learn from them may inform future design decisions to enable reversible Mg-based batteries.

PUBLISHED CONTENT AND CONTRIBUTIONS

Laskowski, F. A. L., Stradley, S.H., et al. (2021). "Mg Anode Passivation Caused by the Reaction of Dissolved Sulfur in Mg–S Batteries". In: *ACS Appl. Mater. Interfaces* 13, 25, 29461–29470. DOI: 10.1021/acsami.1c02788.
SHS performed initial experiments establishing cell configuration and S concentration regimes and helped write the manuscript.

Stradley, S.H., Jones, J.P., et al. (2024). "Investigating Capacity Fade Mechanisms in Dual-Ion Mg-MClx Batteries". In: *J. Electrochem. Soc.* 171 060501. DOI: 10.1149/1945-7111/ad4fe4.
SHS designed and performed experiments, analyzed the data, and wrote the manuscript.

Stradley, S.H., and See, K.A.S. "Realizing Al as a water-resistant Mg host for energy storage". *in preparation*.
SHS participated in conception of the project, designed and performed experiments, analyzed the data, and wrote the manuscript.

TABLE OF CONTENTS

Acknowledgements . . . iii
Abstract . . . v
Published Content and Contributions . . . vi
Table of Contents . . . vi
List of Illustrations . . . ix
List of Tables . . . xvii
Nomenclature . . . xviii
Chapter I: Introduction . . . 1
1.1 Background and Motivation . . . 1
1.2 Thesis Outline . . . 3
Chapter II: Investigating capacity fade mechanisms in Mg-MCl_x batteries . . . 5
2.1 Abstract . . . 5
2.2 Introduction . . . 5
2.3 Methods . . . 8
2.4 Results and Discussion . . . 9
2.5 Conclusions . . . 18
2.6 Acknowledgments . . . 19
Chapter III: Electrochemical and analytical characterization of a highly stable, halide free Mg electrolyte based on weakly coordinating silicate anions . . . 20
3.1 Abstract . . . 20
3.2 Introduction . . . 20
3.3 Experimental . . . 23
3.4 Results and discussion . . . 24
3.5 Conclusions . . . 35
3.6 Acknowledgments . . . 35
Chapter IV: Electrochemical and analytical characterization of a Mg electrolyte 36
4.1 Abstract . . . 36
4.2 Introduction . . . 36
4.3 Experimental . . . 38
4.4 Results and Discussion . . . 39
4.5 Conclusions . . . 48
4.6 Acknowledgments . . . 48
Chapter V: Realizing Al as a water-resistant Mg anode for energy storage . . . 49
5.1 Abstract . . . 49
5.2 Introduction . . . 49
5.3 Results and discussion . . . 53
5.4 Conclusions . . . 69
Chapter VI: Conclusions and Outlook . . . 70
Bibliography . . . 73

Appendix A: Supplementary Information for Investigating capacity fade mechanisms in Mg-MCl_x batteries 86
Appendix B: Supplementary Information for Electrochemical and analytical characterization of a highly stable, halide free Mg electrolyte based on weakly coordinating silicate anions 90
Appendix C: Supplementary Information for Electrochemical and analytical characterization of a Mg electrolyte 97
Appendix D: Supplementary Information for Realizing Al as a water-resistant Mg host for energy storage 100

LIST OF ILLUSTRATIONS

Number *Page*

1.1 A schematic of a typical LIB. The anode is graphite, the cathode is $LiCoO_2$, and the electrolyte is $LiPF_6$ dissolved in an organic solvent. . 2

2.1 First charge and discharge profiles of various MCl_x cathodes at 0.12 C with the APC electrolyte: (a) AgCl, (b) CuCl, (c) $FeCl_2$, (d) $CuCl_2$, and (e) $FeCl_3$. AgCl has the highest discharge potential and lowest voltage hysteresis. Charge and discharge proceed through voltage plateaus at comparatively high voltages relative to the other metal chlorides in this study. CuCl and $CuCl_2$ display sloping discharge profiles and charge profiles with a lower potential sloping region and higher potential plateau. $FeCl_2$ and $FeCl_3$ show low voltage discharge plateaus and moderate voltage charge plateaus. 10

2.2 (a) Potential vs time traces of an AgCl cell cycled normally and an AgCl cell with a 24 hour rest after charge. (b) Second cycle capacity retention of MCl_x cathodes with and without a 24 hour rest after charge. AgCl shows essentially no difference in capacity fade. More soluble chlorides show more rapid fade. 12

2.3 Initial discharge curve at 0.12C with the APC electrolyte of (a) AgCl and (b) $CuCl_2$. Ex situ pXRD and refinement for (c) the AgCl cell and (d) the $CuCl_2$ cell, with reflections indicated for Ag and Cu, respectively. Ag is recovered in the AgCl cell, and Cu is recovered in the $CuCl_2$ cell. 13

2.4 (a) SEM image of a Mg anode from a Mg|APC|$CuCl_2$ cell after discharge, the corresponding elemental maps for (b) Mg and (c) Cu, and (d) the sum EDS spectrum for the region. A layer dominated by Mg, O, Cu, and Al is present on the electrode.(e) SEM image of a Mg anode from a Mg|APC|AgCl cell after discharge, the corresponding elemental maps for (f) Mg and (g) the sum EDS spectrum for the region. A layer dominated by Mg and O is present on the electrode. . 15

2.5 Ex situ pXRD patterns for (a) AgCl and (b) $CuCl_2$ cathodes, showing traces for a pristine cathode and cathodes assembled into cells and rested for 7 days with the APC or APC + 20 % $AlCl_3$ electrolyte. APC chemically reduces the metal chloride to the metal. APC + 20% $AlCl_3$ slows the chemical reduction. 17
2.6 (a) First discharge of $CuCl_2$ cells and (b) discharge capacity as function of cycle number for a $CuCl_2$ cathode with a variety of electrolytes. Quenching the Grignard or removing it from the electrolyte while increasing salt concentration moderate capacity fade but does not prevent it in long-term cycling. 18
3.1 Structure of $Mg[^{Me}Si^{F}_{24}]_2$ in DME. 24
3.2 (a) Selected cyclic voltammograms of 0.25 M $Mg[^{Me}Si^{F}_{24}]_2$ + 10 mM Me_2Mg additive in DME. The inset highlights the deposition overpotential region of the CV. (b) Coulombic efficiency for cycles 1 – 75. The $Mg[^{Me}Si^{F}_{24}]_2$ electrolyte shows high efficiencies and minimal electrochemical conditioning. 25
3.3 Linear sweep voltammograms of 0.25 M $Mg[^{Me}Si^{F}_{24}]_2$ + 10 mM Me_2Mg in DME on Pt, Al, stainless steel 316, and Pt without no added Me_2Mg. Scan rate = 5 mV/s, RE/CE = Mg. 26
3.4 Chronopotentiometry traces of symmetric Mg|0.25 M $Mg[^{Me}Si^{F}_{24}]_2$ + 10 mM Me_2Mg|Mg cells at a variety of applied current densities. . 27
3.5 Long term chronopotentiometry trace of a symmetric Mg|0.25 M $Mg[^{Me}Si^{F}_{24}]_2$ + 20 mM Bu_2Mg|Mg cell with an applied current density of 0.5 mA cm^{-2} alternating between oxidation and reduction in 30 minute intervals following a conditioning step at 0.0025 mA cm^{-2}. 28
3.6 (a) Chronopotentiometry trace, (b) SEM micrograph, EDS maps for (c) Mg and (d) Si and the corresponding EDS sum spectrum (bottom) of deposition at -0.5 mA cm^{-2} from 0.25 M $Mg[^{Me}Si^{F}_{24}]_2$ + 20 mM Bu_2Mg for 5 hours on Pt. 29
3.7 (a) Chronopotentiometry traces and corresponding SEM micrographs at (b) -0.5 mA cm^{-2} for 5 hours, (c) at -2.5 mA cm^{-2} for 1 hr, and (d) at -10 mA cm^{-2} for 0.25 hr onto a Pt substrate from 0.25 M $Mg[^{Me}Si^{F}_{24}]_2$ + 15 mM Me_2Mg 30

3.8 Selected cyclic voltammograms of 0.25 M $Mg[^{Me}Si^{F}_{24}]_2$ dissolved in (a) 3MPA, (b) 3MPA:DME 1:10 vol:vol, and (c) DME. 3MPA serves to lower the reductive overpoential of $Mg[^{Me}Si^{F}_{24}]_2$. The use of a mixed solvent system lessens the conditioning process. 30
3.9 (a) Cyclic voltammograms of 0.25 M $Mg[^{Ph}Si^{F}_{24}]_2$ + 20 mM Bu_2Mg additive in DME at a scan rate of 25 mV/s. The inset (b) highlights the deposition overpotential region of the CV. (c) Coulombic efficiency for cycles 1 – 100. 33
4.1 (a) Cyclic voltammograms of WCA-1 dissolved in DME to varying concentrations with the inset (b) highlighting the reductive overpotential region. WE: Pt, CE: Mg, RE: Mg. 25 mV s^{-1}. Cycle 25 shown. 41
4.2 (a) EIS spectra at a variety of WCA-1 electrolyte concentrations in DME and (b) the corresponding conductivities calculated from these spectra. 42
4.3 (a) Potential vs. time trace of deposition from 0.5 M WCA-1 in DME at a rate of 0.5 mA cm^{-2} for five hours with (b) the corresponding SEM micrograph and (c) the EDS map for Mg. WE: Pt, CE: Mg, RE: Mg. 42
4.4 Chronopotentiometry of Mg|Mg symmetric cells with 0.5 M WCA-1 in DME at a variety of applied areal current densities ranging from 0.1 mA cm^{-2} to 2.5 mA cm^{-2}. 43
4.5 (a) Cyclic voltammograms of WCA-2 dissolved in DME to varying concentrations with the inset (b) highlighting the reductive overpotential region and (c) illustrating the anion. WE: Pt, CE: Mg, RE: Mg. 25 mV s^{-1}. Cycle 25 shown. 44
4.6 (a) Potential vs. time trace of deposition from 0.25 M WCA-2 in DME at a rate of 0.5 mA cm^{-2} for five hours with the corresponding SEM micrograph (b) and the EDS map for Mg (c). This electrolyte supports compact Mg^0 deposition. 46
4.7 (a) Galvanostatic cycling of Mg|Mg symmetric cells with 0.25 M WCA-2 in DME at a variety of applied areal current densities ranging from 0.1 mA cm^{-2} to 5.0 mA cm^{-2} and (b) traces for extended cycling at 0.5 mA cm^{-2}. The bulkier anion shows improved performance at faster rates. 46

4.8 Linear sweep voltammograms of 0.25 M WCA-2 in DME at 5 mV s^{-1} on a variety of substrates.The electrolyte shows a relatively low anodic stability. CE/RE: Mg 47
5.1 (a) XRD patterns of the ABX series, where X = wt% Bi along with highlighted regions that showcase reflections associated with (b) Bi and (c) Al. 54
5.2 (a) Cyclic voltammograms of ABX ($0 \leq x \leq 100$) with the APC electrolyte at 1 mV s^{-1}, (b) a highlight of the region from 0.1 V to 0.4 V. 57
5.3 (a) Selected cyclic voltammograms of AB40 at 0.1 mV s^{-1} with the APC electrolyte and (b) inset highlighting cycles 1 and 2. 58
5.4 (a) Galvanostatic trace of an AB40 electrode reduced at C/100 with the APC electrolyte with inset highlighting initial region and (b) ex situ XRD patterns of the reduced electrode presented with that of a pristine electrode for reference. Reflection positions for Bi and Mg are indicated.(c) SEM micrograph and EDS maps for (d) Mg and (e) Al for one site of the same electrode. (f) SEM micrograph and EDS map for (g) Mg for a second site. 63
5.5 (a) Selected cyclic voltammograms of a Pt working electrode with the MACC electrolyte at 5 mV s^{-1} with and without 10 mM H_2O. MACC shows reversible Mg^{2+} plating and stripping. Adding 10 mM H_2O results in irreversible reductions on cycle 1. (b) R_{CT} values measured as a function of cyclic voltammogram cycle number for AB40 in MACC +/- 10 mM H_2O and Mg and Pt in MACC + 10 mM H_2O. Mg and Pt working electrodes show increased R_{CT} with cycling. AB40 is cycled from -0.25 to 0.75 V, Mg is cycled from -0.25 to 0.25 V, and Pt is cycled from -0.75 to 0.75 V 67
5.6 Cyclic polarization of (a) Mg, (b) AB40, (c) Al, and (d)Bi with and without 10 mM H_2O. Nobility trends Bi, Al, AB40, and then Mg. AB40 shows the lowest overall corrosion current. 68
A.1 Cell schematic featuring Mo current collectors, PTFE body components, a Mg anode, GFD separator, and a MClx cathode. 86
A.2 First and second cyclic voltammagrams of (a) AgCl, (b) CuCl, (c) $CuCl_2$, (d) $FeCl_2$, and (d) $FeCl_3$ with a Mg counter/reference electrode and the APC electrolyte. 87

A.3 First five galvanostatic cycles at 0.12C for an (a) AgCl cathode and a (b) $CuCl_2$ cathode. Cells were disassembled after five cycles, and one electrode was replaced. Subsequent discharge curves are shown for (c) AgCl and (d) $CuCl_2$. 87
A.4 Ex situ pXRD patterns of (a) AgCl and (b) $CuCl_2$ cathodes at various states of charge. 88
A.5 GITT curves at 0.12C of (left) AgCl and (right) $CuCl_2$ cathodes with various processing techniques: (a) and (b) AgCl synthesized in the presence of C; (c) and (d) $CuCl_2$ processed in a planetary mill; (e) and (f) AgCl and (g) and (h) $CuCl_2$ processed in a high energy ball mill; and (i) and (j) AgCl and (k) and (l) $CuCl_2$ ground by hand. . . . 88
A.6 Chronopotentiometry traces of Mg|Mg symmetric cells with the APC electrolyte. The Mg foils have been soaked for 7 days in (a) APC + saturated AgCl, (b) APC + saturated $CuCl_2$, and (c) APC. 89
B.1 Selected cyclic voltammograms of 0.25 M $Mg[^{Me}Si^{F}_{24}]_2$ electrolyte with (a) 10 mM, (b) 5 mM, (c) 2 mM, and (d) 0.5 mM Me_2Mg additive. WE: Pt, CE: Mg, RE: Mg, 25 mV/s. 91
B.2 Coulombic efficiency as a function of cycle number for the cyclic voltammograms illustrated in S1. 91
B.3 Chronopotentiometry traces of symmetric Mg|0.25 M $Mg[^{Me}Si^{F}_{24}]_2$ + 10 mM Me_2Mg|Mg at (a) 0.1 mA cm^{-2} and (b) 5 mA cm^{-2}. 92
B.4 Chronopotentiometry traces of symmetric Mg|0.25 M $Mg[^{Me}Si^{F}_{24}]_2$ + 20 mM Bu_2Mg|Mg during hours (a) 5 - 15 and (b) 1490 - 1500. . . 92
B.5 SEM micrograph of deposition at -0.5 mA cm^{-2} from 0.25 M $Mg[^{Me}Si^{F}_{24}]_2$ + 20 mM Bu_2Mg for 5 hours on Pt. 93
B.6 Coulombic efficiency as a function of cycle index for 0.25 M $Mg[^{Me}Si^{F}_{24}]_2$ dissolved in 3MPA, DME, and DME:3MPA 1:10 vol:vol. 93
B.7 Selected cyclic voltammograms of 0.25 M $Mg[^{Ph}Si^{F}_{24}]_2$ dissolved in DME + 15 mM Me_2Mg (a), in DME:3MPA 1:10 (b), and (c) their corresponding Coulombic efficiencies. 94
B.8 Structure of $Mg[^{Ph}Si^{F}_{24}]_2$ 94
B.9 Cyclic voltammograms of 0.25 M $Mg[^{Me}Si^{F}_{24}]_2$ dissolved in DME + 10 mM Me_2Mg on a (a) new Pt working electrode and a (b) used Pt working electrode. 95

B.10 (a) SEM micrograph of a used Pt working electrode post treatment with nitric acid and H_2 flame and corresponding EDS maps for (b) Si and (c) O. 95
B.11 Selected cyclic voltammograms of 0.25 M $Mg[^{Me}Si^{F}_{24}]_2$ dissolved in DME with variable concentrations of Me_2Mg: (a) 15 mM, (b) 25 mM, (c) 50 mM, (d) 100 mM. WE: Pt, CE: Mg, RE: Mg. 25 mV s^{-1}. 96
B.12 Selected cyclic voltammograms of 0.25 M $Mg[^{Me}Si^{F}_{24}]_2$ dissolved in DME + 10 mM Me_2Mg in (a) a "standard" battery lab glovebox purged for 45 minutes and (b) a vacant glovebox purged for 15 minutes. WE: Pt, CE: Mg, RE: Mg. 25 mV s^{-1}. 96
C.1 Coulombic efficiency as a function of cycle number for the cyclic voltammograms shown in Figure 4.1. 97
C.2 EDS sum spectrum for the deposition shown in Figure 4.3. 98
C.3 Coulombic efficiency as a function of cycle number for the cyclic voltammograms shown in Figure 4.5. 98
C.4 EDS sum spectrum for the deposition shown in Figure 4.6. 99
D.1 Cartoon illustrating phase segregation of an "AB" alloy into distinct Mg_xA_y and Mg_wB_v intermetallics upon magnesiation 100
D.2 First, second, and seventy-fifth cyclic voltammograms of an Al powder composite electrode with the APC electrolyte. CE: Mg, RE: Mg. 1 mV s^{-1} No Faradaic features are observed on cycles 1 or 2. After several cycles, a reduction occurs around 0.11 V. This feature is paired with an oxidation around 0.375 V. These features show very low current densities. 101
D.3 EDS spectra for the ABX ($20 \leq x \leq 100$) alloy series. (a) Bi, (b) AB80, (c) AB60, (d) AB40, (e) AB20. The Zr impurity trends with Bi concentration in milled alloys. 101
D.4 SEM micrographs and corresponding Al and Bi EDS maps for (a, b, c) AB60, (d, e, f) AB40, and (g, h, i) AB80. All compositions show a homogenous distribution of Al and Bi on the micron scale. 102
D.5 Rietveld refinements for (a) AB40 and (b) AB60 fitting to distinct Al and Bi phases with reflections for Al and Bi indicated. 102
D.6 Rietveld refinements for AB40 fitting to a single Bi phase with reflections for Al and Bi indicated. 103

D.7 (a) Cyclic voltammograms of ABX ($0 \leq x \leq 100$) with the APC electrolyte at 1 mV s^{-1} with current densities normalized to peak oxidative current (b) the same curves highlighting the cathodic region. 103
D.8 Cyclic voltammograms of ABX ($0 \leq x \leq 100$) with the APC electrolyte at 1 mV s^{-1} showing cycles 1 - 100. 104
D.9 (a) Selected cyclic voltammograms of AB40 and (b) Bi at 1 mV s^{-1} with the APC electrolyte and varied lower voltage cutoffs: cycles 1-5: 0 V - 0.75 V; cycles 6-75: 0.1 V - 0.75 V; and cycles 76-150: 0 V - 0.75 V. 104
D.10 Peak current densities for (a) Mg-Bi and (b) Mg-Al dealloying. Values of $x \geq 40$ display enhanced activity in the Mg-Al region. Mg-Bi current density varies directly with Bi content. 105
D.11 SEM micrographs and corresponding EDS maps for Al and Bi of AB40 (a - c) as cast and (d - f) after 75 CV cycles. Phase separation is not evident on the micron scale. 105
D.12 SEM micrographs of (a) Al as received, (b) Bi as received, (c) AB20 milled 20 hours, and (d) AB60 milled 20 hours. The precursor metal powders have a lower average surface area than the milled alloys. . . 106
D.13 (a) XRD pattern of Al60Sn40 milled 20 hours with reflections for Al and Sn indicated and (b) first and tenth cyclic voltammograms of Al60Sn40 with the APC electrolyte at 1 mV s^{-1}. No Faradaic features are observed throughout cycling. 106
D.14 EDS spectra for (a) site 1 and (b) site 2 of an AB40 electrode reduced at C/100 for 100 hours. 107
D.15 (a) Galvanostatic traces of AB40 reduced at various rates and (b) corresponding ex situ XRD patterns of the same electrodes with reflections for Bi and Mg indicated. 107
D.16 (a) Chronopotentiometry trace of a Bi electrode reduced at C/100 and C/20 with the APC electrolyte and (b) ex situ XRD patterns of the reduced electrodes presented with that of the as prepared electrode for reference. Reflection positions for Bi and Mg_3Bi_2 are indicated. . 108
D.17 Selected EIS spectra measured following a 60s OCV rest after the working electrode potential is swept to the lower voltage cutoff for (a) an AB40 working electrode in MACC and (b) AB40, (c) Mg, and (d) Pt working electrodes in MACC + 10 mM H_2O. Following EIS, the potential is swept positive to 0.75 V, and the process is repeated. . 108

D.18 Selected cyclic voltammograms for (a) an AB40 working electrode in MACC and (b) AB40, (c) Mg, and (d) Pt working electrodes in MACC + 10 mM H_2O. 109

LIST OF TABLES

Number *Page*

2.1 Initial discharge capacities of MCl_x cathodes 11

D.1 Calculated lattice parameters from Rietveld refinements in Figure C4 100

NOMENCLATURE

(p)XRD. (powder) X-ray diffraction.

3MPA. 3 methoxypropylamine.

APC. all phenyl complex.

CE. Coulombic efficiency.

CE. counter electrode.

CV. cyclic voltammetry.

DME. dimethoxyethane.

EDS. energy-dispersive X-ray spectroscopy.

FPB. fluorinated pinacolatoborate.

G4. tetraglyme.

GITT. galvanostatic intermittent titration technique.

hfip. tetrakis(hexafluoroisopropyloxy)borate.

HMDS. hexamethyldisilizide.

IPA. isopropanol.

J. current density.

LIB. Li-ion battery.

LMB. Li-metal battery.

MACC. magnesium aluminum chloride complex.

OCV. open circuit voltage.

ppm. parts per million.

PTFE. polytetrafluoroethylene.

RE. reference electrode.

SEM. scanning electron microscopy.

SS(316). stainless steel (316).

TFSI. bis(trifluoromethane sulfonyl)imide, $N(SO_2CF_3)^-$.

THF. tetrahydrofuran.

V. voltage.

WCA. weakly coordinating anion.

WE. working electrode.

Chapter 1

INTRODUCTION

1.1 Background and Motivation

The alarming rise in atmospheric CO_2 and the concurrent effects on the Earth's climate drive the need for widespread adoption of green energy sources and electrified transport.[1] The demand for clean power requires utilities to progressively increase the portion of renewable sources in their energy generation profile. Certain emissions-free sources, namely solar and wind, produce energy intermittently, thus creating a need to store energy produced in times of surplus so that it may be used in times of deficit. Though pumped hydro remains the most commercially viable means to store energy in many situations, electrochemical energy storage in the form of batteries may see widespread deployment if such systems are economically and technologically competitive.[2, 3] Likewise, a major barrier to the increased adoption of electric vehicles for personal and commercial transport is the cost and limited capacity of the batteries powering them.[4] Thus, though urgent, these two drives are hindered by a lack of batteries based on reliable, safe, energy-dense, and resource equitable materials.

All batteries contain three basic components: the anode, or low voltage electrode; the cathode, or high voltage electrode; and the electrolyte, an ionically conductive but electronically insulating medium between the two electrodes. Originally devised in the 1970s and commercialized in the 1990s, Li-ion batteries (LIBs) are the industry standard for electrochemical energy storage.[5, 6] A typical modern LIB is illustrated in Figure 1.1. In this case, the anode is graphite, the cathode is $LiCoO_2$, and the electrolyte is $LiPF_6$ dissolved in an organic solvent. The basic operating principle of LIBs relies on the potential difference between the electrodes. As assembled, no current flows between the two because of the electronically insulating nature of the electrolyte. If the two electrodes are connected by an external circuit through which electrons can flow, however, the potential difference between them drives the flow of electrons from the anode to the cathode. This current may be used to do useful work. As electrons shuttle between the anode and cathode, charge balance is maintained by the movement of Li^+ through the electrolyte as Li^+ is deintercalated from the cathode and intercalated into the anode.

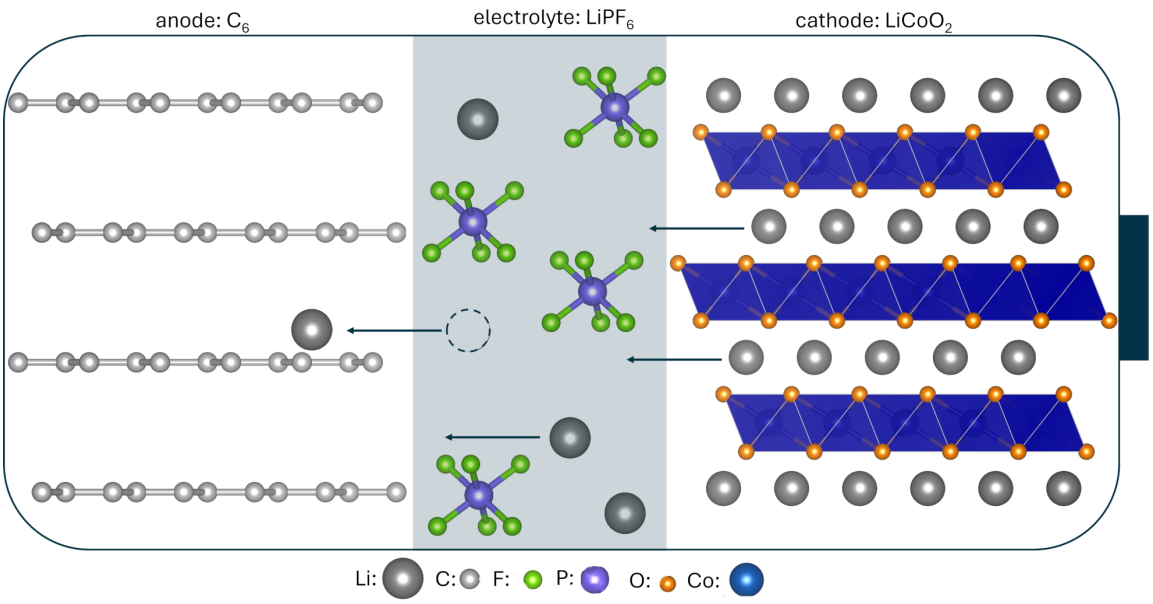

Figure 1.1: A schematic of a typical LIB. The anode is graphite, the cathode is $LiCoO_2$, and the electrolyte is $LiPF_6$ dissolved in an organic solvent.

Though LIBs have achieved market dominance, they alone are not sufficient to meet the needs of a rapidly growing global battery market. The desires to expand the range of electric vehicles and to extend the single charge duration of mobile electronic devices drive the need for batteries with enhanced energy densities. Though significant improvements have been made in extending the storage capacity of LIBs, they are quickly approaching the fundamental limit imposed by intercalation chemistries.[7] Batteries based on a Li metal anode (Li metal batteries, LMBs) promise higher energy densities; however, safety concerns related to the dendritic plating morphology of Li metal hinder their development.[8, 9] What's more, Li itself is quite rare and unevenly distributed in the Earth's crust and may thus prove unsuitable to meet the needs of a growing global battery market alone.[10] These factors prompt the investigation of alternative battery chemistries.

Mg is a promising alternative to Li. Not only is Mg more abundant than Li in the Earth's crust by several orders of magnitude, it is also globally widespread.[11, 12] Mg is also attractive from an energy storage point of view as the divalent nature of the Mg^{2+} cation endows Mg metal anodes with nearly double the volumetric capacity of comparable Li metal anodes.[7] Under the same operating conditions, Mg^{2+} is also known to adopt a smoother deposition morphology than Li^{+}, promoting safer operation.[13–15] Despite the positive characteristics of Mg-based chemistries, the

development of Mg-based batteries is hindered by a lack of mutually compatible anode, cathode, and electrolyte materials.

1.2 Thesis Outline

This thesis details several studies aimed at addressing the lack of materials which support reversible Mg electrochemistry. Each case examines a candidate material or class of materials with promising characteristics for use as a Mg anode, cathode, or electrolyte. We seek to understand which material properties are important in determining efficient and reversible cell performance and thereby establish design principles towards a hypothetical rechargeable Mg-based battery.

Chapter 2 proposes transition metal chlorides of the form MCl_x as cathode materials in dual-ion Mg^{2+}/Cl^- batteries. A corrosion-resistant cell configuration based on Mo-current collectors is established, and reversible conversion of MCl_x based on industrial metals such as Fe and Cu is demonstrated for the first time. Capacity fade mechanisms in these systems are thoroughly investigated and somewhat mitigated through modification of the electrolyte.

Chapter 3 provides detailed electrochemical and analytical characterization of a halide-free Mg electrolyte based on a weakly coordinating Si-centered anion. We present detailed characterization of a structural variant of the anion featuring a methyl axial ligand and preliminary data for another featuring a phenyl functional group. This electrolyte reversibly plates and strips Mg with high efficiency. It also exhibits the highest oxidative stability and sustains the highest applied current density without dendritic growth demonstrated to date. The compound is sensitive to exposure to water, even in standard glovebox atmospheres.

Chapter 4 details electrochemical and analytical characterization of a pair Mg electrolytes based on B-centered anions with aryl axial ligands. One bearing Mes ligands exhibits one of the lowest overpotentials for Mg deposition among reported halide-free Mg electrolytes. It plates and strips Mg with high efficiency but has poor performance at high rates. The second bearing a bulkier anion exhibits a slightly larger reductive overpotential but also features improved kinetic performance. We attribute this improvement to weakened association between the anion and the sovlated Mg^{2+} complex. Though a low oxidative stability limits the real world utility of these electrolytes, this investigation suggests increasing anion bulk as a design principle to improve the kinetic performance of B-based halide-free Mg electrolytes.

Chapter 5 explores Al as a Mg alloying anode. We provide the first evidence supporting reversible Mg-Al alloying in nonaqueous systems. We then prepare a series of Al-Bi alloys in which Mg-Al alloying current density is enhanced by two orders of magnitude. Although bulk alloying is limited by a large particle size, we use voltammetric methods to investigate the alloying-dealloying mechanism and demonstrate an enhanced resistance to passivation by water relative to traditional Mg metal anodes.

Chapter 2

INVESTIGATING CAPACITY FADE MECHANISMS IN MG-MCL$_x$ BATTERIES

Adapted from Stradley, S.H., Jones, J. P., Bugga, R. V., See, K. A. Investigating capacity fade mechanisms in Mg-MCl$_x$ batteries, J. Electrochem.Soc., 2024 171 060501

2.1 Abstract

Mg batteries are a promising alternative to Li-based chemistries due to the high abundance, low cost, and high volumetric capacity of Mg relative to Li. Mg is also less prone to dendritic plating morphologies, promising safer operation. Mg plating and stripping is highly efficient in chloride-containing electrolytes; however, chloride is incompatible with many candidate cathode materials. In this work, we capitalize on the positive effect of chloride by using transition metal chloride cathodes with a focus on low cost, Earth-abundant metals. Both soluble and sparingly soluble chlorides show capacity fade upon cycling. Active material dissolution and subsequent crossover to the Mg anode are the primary drivers of capacity fade in highly soluble metal chloride cathodes. We hypothesize that incomplete conversion and chemical reduction by the Grignard-based electrolyte are major promoters of capacity fade in sparingly soluble metal chlorides. Modifications to the electrolyte can improve capacity retention, suggesting that future work in this system may yield low cost, high retention Mg-MCl$_x$ batteries.

2.2 Introduction

The transition to a clean energy economy is hindered by a lack of safe, reliable, and efficient energy storage technologies.[1] Lithium-ion batteries (LIBs) dominate the modern battery market.[6, 7] However, LIBs are based on scarce and expensive resources as reserves of Li, Ni, and Co, key components of modern LIBs, are concentrated in just a handful of regions.[10, 16, 17] LIBs are also approaching the theoretical capacity limit imposed by intercalation chemistries and are unlikely to undergo more than minor improvements in coming decades.[7] Li-metal batteries are expected to have a higher storage capacity than LIBs; however, safety concerns related to dendritic Li plating limit utility and Li is still a major component that

suffers from resource issues.[9]

Mg-ion batteries (MIBs) are an appealing alternative to Li-based chemistries. Based on known reserves, Mg is orders of magnitude more abundant than Li in the Earth's crust.[12] Mg is also present in seawater at a concentration of about 1300 ppm. After Na, it is the most commonly found cation in the oceans.[11] The high relative abundance makes MIBs a more economical and sustainable choice than batteries that rely on Li.[4] Additionally, the volumetric capacity of a Mg metal anode is nearly twice that of Li metal (3830 vs. 2060 mAh mL^{-1}). Though some studies have demonstrated the formation of Mg dendrites under select conditions[15, 18], Mg has been found to plate more smoothly than Li under comparable current densities due to its low self-diffusion barrier.[13, 14]

Electrolytes for Mg plating and stripping are difficult to develop and the most successful electrolytes contain Cl.[19, 20] The electroactive cationic species identified in most Cl-containing electrolytes is the binuclear complex $Mg_2(\mu\text{-}Cl)_3^+$.[20–23] Though the exact role of Cl in promoting reversible Mg electrodeposition is hard to determine, evidence suggests that Cl interacts with the Mg-electrolyte interface to facilitate Mg^{2+} reduction and prevent passivation. The formation of a Cl-containing "enhancement layer" in the all-phenyl complex (APC) and other Grignard-based electrolytes has been shown to improve deposition and stripping kinetics and overpotentials.[24] Computational studies have demonstrated that the adsorption of cationic $(MgCl)^+$monomers is thermodynamically favorable and that such complexes have low desolvation energies, promoting facile Mg^{2+}reduction.[25] Later studies have likewise proposed the initial adsorption of $(MgCl)^+$ as a necessary step preceding Mg electrodeposition in Cl-containing electrolytes.[26, 27]

In addition to the favorable effect of Cl on Mg metal anode electrochemistry, the use of the highly mobile Cl anion, Cl^-, as a charge carrier may overcome the issues typically associated with the sluggish transport of Mg^{2+} in solution. Examples of Cl conversion in batteries are not uncommon. Reversible conversion of metal chlorides has been demonstrated in Na|MCl_x cells (M = Fe^{2+}, Ni^{2+}, Cu^{2+}, Zn^{2+}) at elevated temperatures.[28, 29] An Al|Cl_2 cell has been demonstrated with a room-temperature molten salt electrolyte[30]. Metal chlorides (AgCl, $CuCl_2$, $CoCl_2$, VCl_3, and $BiCl_3$) and metal oxychlorides (BiOCl and FeOCl) have been paired with Li and room-temperature non-aqueous liquid electrolytes.[31–34]

To capitalize on the beneficial effects of Cl on Mg electrochemsitry, we aim to develop a system that pairs a Mg metal anode with a Cl-containing electrolyte and

a transition metal chloride cathode of the form MCl_x (M = Cu, Fe, etc.). Such a battery would operate on a conversion-type mechanism. During discharge, the metal chloride cathode is reduced and the Mg anode is oxidized:

$$MCl_x + xe^- \rightarrow M + xCl^- \tag{2.1}$$

$$Mg \rightarrow Mg^{2+} + 2e^- \tag{2.2}$$

We hypothesize that the ionic species will interact in the electrolyte to form a soluble $[Mg_yCl_x]^{n-}$ complex, the structure of which depends on the properties of the electrolyte. The reverse processes occur upon charge. A downside of this chemistry is the formation of a soluble product during discharge whose solubility will limit the capacity. However, other successful battery systems have been developed that yield soluble products, notably the lead acid battery.

The study of metal chloride cathodes in Mg systems has been largely confined to AgCl. Zhang et al. have investigated AgCl as a conversion cathode to pair with a Mg anode and the APC electrolyte.[35] Initial discharge yielded nearly 100% theoretical conversion with impressive rate performance; however, the chemistry suffers from significant capacity fade with cycling, due to the dissolution of the AgCl active material.[35] Li et al. observed similarly impressive rate performance, albeit with a lower initial discharge capacity, by pairing AgCl and Mg with an $Mg(HMDS)_2-AlCl_3-MgCl_2$ electrolyte.[36] Inspired by these initial studies, we aim to study other metal chlorides that might bypass the high cost of Ag .[37, 38] Other Mg|MCl_x (M = Cu^+, Cu^{2+}, Ni^{2+}) cells have been discharged, but reversible conversion has not been demonstrated.[35]

In this work, we expand the library of reversible Mg|MCl_x chemistries to include several metal chlorides based on Earth-abundant, low cost metals such as Fe and Cu. We establish a cell geometry that allows for the reversible conversion of these compounds despite the highly corrosive electrolyte environment. Investigation of several capacity fade mechanisms has led us to suggest that the primary drivers of capacity fade in Mg|MCl_x systems are active material dissolution and reactivity with the Grignard-based electrolyte. Attempts to moderate capacity fade through modification of the electrolyte shows some improvement, suggesting that further research in this area may yield low cost, low fade Mg|MCl_x cells.

2.3 Methods

Preparation of MCl_x-C composites

The AgCl-C composite was prepared according to Zhang et al.[35] Silver nitrate ($AgNO_3$, 99+%, Sigma, 1.69 g) was dissolved in 500 mL of water. Super P carbon (99+%, Fisher, 1.00 g) was then added while stirring. Finally, 20 mL of concentrated HCl (36.5 to 38.0% w/w, Fisher) was added dropwise. The precipitate was collected by vacuum filtration, dried at 85°C under vacuum overnight, and immediately brought into a glovebox. CuCl (99+%, anhydrous, Fisher), $CuCl_2$ (99.995%, anhydrous, Sigma), $FeCl_2$ (99.99+%, anhydrous, Sigma), and $FeCl_3$ (99.99+%, anhydrous, Sigma) were used as received. These metal chlorides were combined with Super P carbon in a 1:1 ratio (w:w) in an Ar-filled glovebox and milled at 300 rpm for 5 h in a planetary ball mill (MSE supplies) without exposure to air. This high MCl_x:C ratio was chosen to ensure sufficient electronic conductivity in prototype cathodes to study the electrochemical properties of these insulating MCl_xs.

Cathode Preparation

The MCl_x−C composites were combined with additional Super P carbon and polytetrafluoroethylene (PTFE, Sigma) to achieve a final composition of AgCl:Super P:PTFE 40:50:10 by mass or MCl_x:Super P:PTFE (M ≠ Ag) 25:65:10 and ground by hand for 10 minutes. The composite material was pressed into pellets using an arbor press and a 0.635 cm die and dried overnight at 120°C under vacuum.

Electrolyte Preparation

The APC electrolyte was prepared according to Zhang et al.[35] A Peltier plate was used to cool 106.7 mg $AlCl_3$ (99.999%, Sigma) to ~-20 °C. To the cool $AlCl_3$, 3.2 mL of cold tetrahydrofuran (THF, Fisher) was added dropwise to dissolve the $AlCl_3$ while stirring. To this solution, 0.8 mL of cold 2.0 M phenylmagnesium chloride (PhMgCl, Sigma) was added dropwise. The electrolyte was stored in a foil-wrapped vial to prevent exposure to light and stirred overnight before use.

The magnesium-aluminum chloride complex (MACC) electrolyte was prepared according to Barile et al.[39] THF (2.5 mL) cooled on a Peltier plate was added dropwise to chilled $AlCl_3$ and stirred until dissolved. Another 2.5 mL of THF was added to $MgCl_2$ (99.9%, Fisher). The $AlCl_3$ solution was added to the $MgCl_2$ solution. Magnesium hexamethyldisilizide ($Mg(HMDS)_2$, 97%, recrystallized before use, Sigma) was added as a chemical conditioning reagent.[40] The resulting solu-

tion, 30 mM $AlCl_3$ + 60 mM $MgCl_2$ + 10 mM $Mg(HMDS)_2$, in THF was stirred overnight before use.

The $MgCl_2$−$AlCl_3$−$Mg(HMDS)_2$ in tetraglyme electrolyte was prepared according to Zhao-Karger et al.[41] A Peltier plate was used to cool 2 mL of tetraglyme (G4, ≥ 99%, Sigma). To the cool G4, 480 mg of chilled $AlCl_3$ was added dropwise while stirring. Next, 620 mg of $Mg(HMDS)_2$ was added and stirred overnight. To this solution, 172 mg of $MgCl_2$ was added and stirred for 40 hours before use.

Electrochemical Characterization

Galvanostatic cycling experiments were conducted in two electrode, Swagelok type cells. The cell stack consisted of a Mg foil (99.9%, 0.5 in diameter x 0.1 mm thick, mechanically cleaned with a razor blade, MTI) anode, a glass fiber (GFD, dried at 85°C under vacuum overnight, VWR) separator, 150 μL electrolyte, and the MCl_x cathode. As constructed, these Mg|MCl_x cells were limited by the theoretical capacity of the cathode. Theoretical capacities for each active material are listed in Table 1. Mo plungers (Midwest Tungsten Service) served as the current collectors, as Mo has been shown to resist corrosion by chloride.[42] All cell body components were made of polytetrafluoroethylene (PTFE). Figure A.1 illustrates the assembled electrochemical cell. Cells were assembled and sealed in a glovebox. Experiments were conducted on a Biologic BCS 805 battery cycler or a VMP3 potentiostat.

Material Characterization

Powder X-ray diffraction (pXRD) measurements were conducted on a Panalytical X'Pert Pro Diffractometer using a Cu Kα X-ray source. Rietveld refinements were fit using GSAS-II.[43] Scanning electron microscopy was conducted using a ZEISS 1550VP field emission SEM with a 15 kV acceleration voltage. SEM samples were prepared in an air-free environment but were briefly exposed to air just before being loaded into the instrument.

2.4 Results and Discussion

To determine the effect of active material solubility on the reversibility of metal chloride electrochemistry, we cycle several metal chlorides against Mg anodes. Figure 2.1 shows the first galvanostatic charge/discharge curves for several MCl_x cathodes, arranged in order of increasing solubility in THF.[35] The AgCl cathode achieves an initial discharge capacity of 184 mAh/g, nearly 99% of its theoretical capacity and on par with literature precedent. [35] The discharge profile plateaus

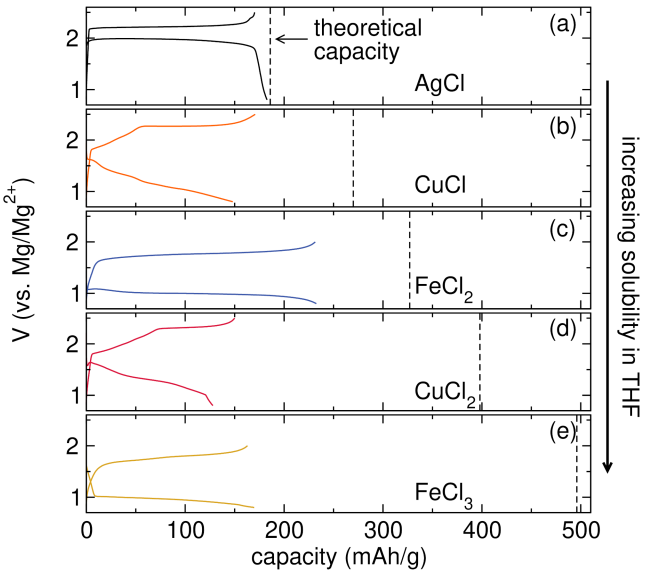

Figure 2.1: First charge and discharge profiles of various MCl_x cathodes at 0.12 C with the APC electrolyte: (a) AgCl, (b) CuCl, (c) $FeCl_2$, (d) $CuCl_2$, and (e) $FeCl_3$. AgCl has the highest discharge potential and lowest voltage hysteresis. Charge and discharge proceed through voltage plateaus at comparatively high voltages relative to the other metal chlorides in this study. CuCl and $CuCl_2$ display sloping discharge profiles and charge profiles with a lower potential sloping region and higher potential plateau. $FeCl_2$ and $FeCl_3$ show low voltage discharge plateaus and moderate voltage charge plateaus.

around 2 V while the charge profile remains similarly flat around 2.2 V vs. the Mg anode/reference, which we take to be near Mg/Mg^{2+}, yielding a relatively low hysteresis of 200 mV. All subsequent voltages will be given referenced to the Mg anode/reference. By contrast, the initial discharge capacities of the other MCl_x cathodes are significantly lower than theoretical and the voltage hystereses are larger. CuCl shows an initial discharge capacity of 150 mAh/g (56% theoretical), $FeCl_2$ shows 231 mAh/g (55% theoretical), $CuCl_2$ shows 128 mAh/g (33% theoretical), and $FeCl_3$ shows 170 mAh/g (34% theoretical). CuCl and $CuCl_2$ feature sloping discharge profiles between 1.6 and 0.7 V. In both systems, charge proceeds first through a sloping feature between 1.8 V and 2.2 V followed by a plateau at 2.3 V. $FeCl_2$ and $FeCl_3$ have initial discharge plateaus at 1 V with corresponding charge plateaus at 1.8 V. To our knowledge, this represents the first demonstrated reversible conversion of CuCl, $CuCl_2$, $FeCl_2$, and $FeCl_3$. Additionally, the initial discharge capacities of CuCl and $CuCl_2$ are higher than in previous reports, potentially due to the difference in cell geometries.[35]

Table 2.1: Initial discharge capacities of MCl_x cathodes

MCl_x	discharge capacity (mAh g^{-1})	theoretical capacity (mAh g^{-1})	% conversion*	solubility in THF[35] (mg L^{-1})
AgCl	184	186	99	0.053
CuCl	148	270	55	10.95
$FeCl_2$	231	327	71	59.7
$CuCl_2$	128	398	32	384.5
$FeCl_3$	168	496	34	(no data)

*assuming 100% Faradaic efficiency

Previous work in Mg|MCl_x systems attributed capacity fade to the dissolution of the active metal chloride by the electrolyte.[35] This hypothesis is largely based on the observations that the initial percent conversion trends inversely with the measured solubility of the metal chloride and that capacity retention is improved at faster cycling rates. Though this hypothesis is in line with the percent conversion and the reported solubilities listed in Table 2.1, it fails to explain the low conversions of more soluble metal chlorides, as the proposed amount dissolved would vastly supersaturate the small volume of electrolyte, absent a shuttle effect to facilitate self discharge. To evaluate this hypothesis in MCl_x cathodes with a wide range of measured solubilities in THF, we perform a modified galvanostatic cycling experiment in which a 24 h open circuit voltage (OCV) hold is imposed between cycle 1 charge and cycle 2 discharge. Figure 2.2 compares the discharge capacity of cycle 2 as a percentage of cycle 1 for cells with and without the 24 h OCV hold. The metal chlorides are arranged so the measured solubility in THF increases from left to right.[35] Figure 2.2 shows the OCV rest causes essentially no difference in capacity fade for AgCl. By contrast, the more soluble MCl_x cathodes show a large increase in capacity fade following a rest after charge. This difference can be explained by the relatively low solubility of AgCl, which is several orders of magnitude less soluble than any other MCl_x, and supports the hypothesis that active material dissolution is a major driver in capacity fade.

Though metal chloride dissolution can cause capacity fade, metal chlorides could also cross over and affect the anode chemistry which could negatively impact cycling behavior. To explore any effects arising from crossover, we cycle Mg|APC|AgCl and Mg|APC|$CuCl_2$ cells five times and then replace the cathode with a fresh electrode and add an additional 75 μL of fresh electrolyte. The cells are then discharged. The initial cycling data along with the post-replacement discharge curves are shown

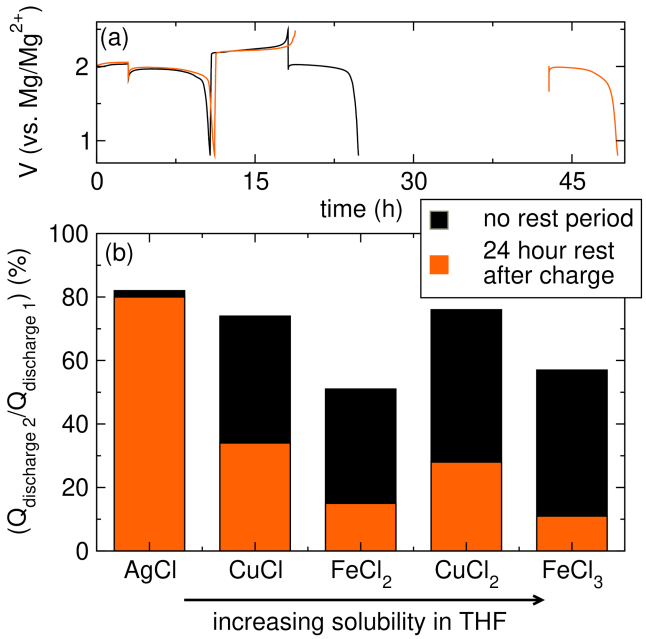

Figure 2.2: (a) Potential vs time traces of an AgCl cell cycled normally and an AgCl cell with a 24 hour rest after charge. (b) Second cycle capacity retention of MCl_x cathodes with and without a 24 hour rest after charge. AgCl shows essentially no difference in capacity fade. More soluble chlorides show more rapid fade.

in Figure A.3. Both AgCl and $CuCl_2$ cells show essentially full capacity recovery when the cathode is replaced. The discharge curve in the $CuCl_2$ cell with the fresh cathode shows a lower nucleation barrier relative to the freshly assembled cell, likely due to some conditioning process priming the already cycled anode. As a control experiment, we perform the same limited cycling protocol and replace the anode after five cycles. Under this condition, the AgCl cell shows continued capacity fade, and the $CuCl_2$ cell shows accelerated capacity fade. These observations further support our hypothesis that the capacity fade stems from dissolution of the active material.

To further investigate the primary drivers of capacity fade in Mg|MCl_x cells, we choose to focus on AgCl and $CuCl_2$ cathodes, as these represent the extremes of measured solubilities in THF, with $CuCl_2$ being over 7,000x more soluble in THF than AgCl.[35] Figure 2.3 (a) and (b) show the first discharge curves of AgCl and $CuCl_2$ cathodes. The AgCl cell discharges to essentially full theoretical capacity. To probe the reduction product, the cell is disassembled and pXRD is measured on the cathode. The pXRD and Rietveld refinement of the discharged AgCl cathode is shown in Figure 2.3 (c). The peaks correspond to Ag metal after discharge, which

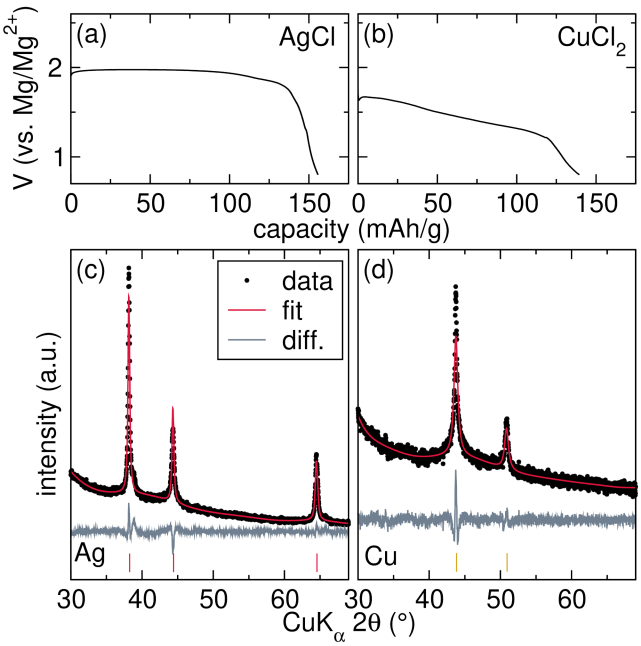

Figure 2.3: Initial discharge curve at 0.12C with the APC electrolyte of (a) AgCl and (b) $CuCl_2$. Ex situ pXRD and refinement for (c) the AgCl cell and (d) the $CuCl_2$ cell, with reflections indicated for Ag and Cu, respectively. Ag is recovered in the AgCl cell, and Cu is recovered in the $CuCl_2$ cell.

is the expected discharge product, and no reflections of the AgCl starting material are observed. In contrast, the $CuCl_2$ cell discharges only to 35% of its theoretical capacity. The pXRD pattern and Rietveld refinement of the discharged cathode is shown in Figure 2.3(d). The pattern shows only two reflections, which are refined to the expected discharge product: Cu metal. Despite the low conversion, no peaks associated with the $CuCl_2$ starting material are observed suggesting that the active material is no longer a crystalline solid in the cathode after discharge.

Upon charging the AgCl cell to 2.75 V, pXRD patterns of the cathode show reflections associated with AgCl; however, some unconverted Ag remains (Figure A.4(a)). The pattern of the recharged $CuCl_2$ cathode, by contrast, does not show any reflections (Figure A.3(b)). We hypothesize that the lack of reflections for $CuCl_2$ is due to dissolution of the compound.

To verify that the discrepancy in initial conversion between AgCl and the more soluble MCl_x cathodes is not due to differences in mixing techniques or kinetic barriers to conversion, galvanostatic intermittent titration is performed on AgCl and $CuCl_2$ cells whose cathodes are prepared with several material processing techniques. Figure A.5 shows the initial discharge and charge GITT curves for AgCl

and $CuCl_2$ cathodes. The AgCl cathode synthesized in the presence of C initially shows overpotentials on the order of 100 mV. These overpotentials grow to ~300 mV as the depth of discharge increases. The corresponding charge curve shows similar overpotentials. The AgCl cathodes prepared by mechanical milling show larger overpotentials for both discharge and charge, indicating that the low overpotentials measured in the cathode synthesized in the presence of C are at least partially due to the intimate mixing of the active material with the conductive C matrix. The $CuCl_2$ cathodes, by contrast, show relatively large conversion overpotentials (~500 mV) for all attempted mixing techniques. Direct comparison of the high power ball milled and hand ground cathodes shows that a substantial portion of the overpotential may be due to intrinsic difficulties associated with the conversion of $CuCl_2$ as we observe little difference in overpotential between the two mixing conditions.

Though evidence suggests that most of the capacity fade in highly soluble MCl_x cathodes is due to dissolution of the active material by the electrolyte, the volume of electrolyte in our electrochemical cells should not be able to dissolve a substantial amount of the active material in the cathode. As assembled, our cells contain 0.25 mL of electrolyte with a typical active loading of 3.5 mg $CuCl_2$. A mere 0.096 mg $CuCl_2$ (approx. 2.75% of the total) should saturate the electrolyte based on the measured solubility of $CuCl_2$ in THF. We hypothesize that a shuttle effect is taking place in which $CuCl_2$ is continuously dissolved from the cathode, migrates across the cell in the electrolyte, and is reduced by the anode. To probe this hypothesis, we discharged a Mg|$CuCl_2$ cell to 0.8 V, extracted the anode, and imaged the surface with a scanning electron microscope. Figure 2.4(a) shows the surface morphology the Mg anode following discharge and the corresponding EDS maps for Mg and Cu are shown in Figure 2.4(b) and (c), respectively. Figure 2.4(a) reveals an uneven, cracked layer coating the Mg anode surface. Elemental analysis of the imaged area, displayed in Figure 2.4(d), shows that this layer is primarily composed of Mg, C, O, and Cu. C likely comes from reductive decomposition of the THF solvent against the Mg surface. Decomposition of the ethereal solvent and brief air exposure prior to the measurement explains the presence of O on the anode surface. Elemental mapping in Figure 2.4(b) and (c) shows that Mg and Cu are distributed in this layer. The presence of Cu on the anode after discharge supports the hypothesis that total capacity loss in the $CuCl_2$ system is promoted by a continuous shuttle of Cu from the cathode to the anode, allowing the electrolyte to leach much more $CuCl_2$ from the cathode than can be explained by the solubility and the volume of electrolyte.

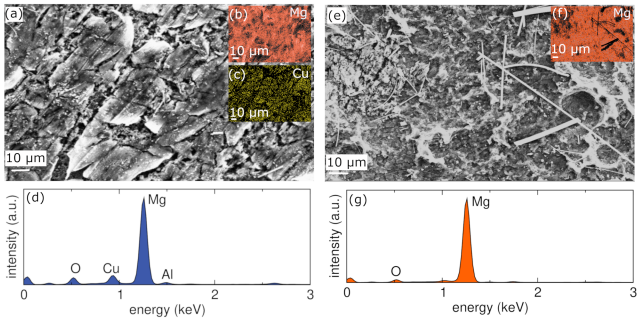

Figure 2.4: (a) SEM image of a Mg anode from a Mg|APC|$CuCl_2$ cell after discharge, the corresponding elemental maps for (b) Mg and (c) Cu, and (d) the sum EDS spectrum for the region. A layer dominated by Mg, O, Cu, and Al is present on the electrode.(e) SEM image of a Mg anode from a Mg|APC|AgCl cell after discharge, the corresponding elemental maps for (f) Mg and (g) the sum EDS spectrum for the region. A layer dominated by Mg and O is present on the electrode.

An analogous experiment was performed with an AgCl cathode. Figure 2.4(e) shows the surface morphology of the anode after discharge. Elemental mapping in Figure 2.4(f) shows Mg distributed throughout this layer. Analysis of the imaged area in Figure 2.4(g) shows that surface layer on the anode is composed mostly of Mg with a small amount of O. The layer formed in the AgCl system has a markedly different surface morphology, dominated by pits rather than plates. In contrast to the $CuCl_2$ cell, the layer formed in the Mg|AgCl cell shows no measurable Ag on the anode. This disparity may be explained by the stark difference in solubilities between the metal chlorides. We hypothesize that the electrolyte is saturated with dissolved AgCl and that a similar shuttle is taking place, but the concentration of AgCl in the electrolyte and the resultant rate of leaching is so low that no significant amount of active material is dissolved before the initial cycling of the cell. The AgCl cell thereby achieves essentially total conversion in its first cycle while the $CuCl_2$ cell features only 35% conversion. We posit that the more gradual capacity fade characteristic of AgCl may be driven by incomplete conversion of the metal Ag to AgCl during charge. This is evident in the reflections in the pXRD pattern for a recharged cathode which can be attributed to Ag (Figure A.4).

To probe the effect of the layer formed on the Mg anode in both Mg|$CuCl_2$ and Mg|AgCl cells on Mg plating and stripping at the anode, we soak Mg foils in saturated solutions of APC + AgCl and APC + $CuCl_2$ for 7 days. The metal foils are collected, rinsed thoroughly with THF, and assembled into symmetric cells with fresh APC electrolyte. Chronopotentiometry traces of these cells are illustrated

in Figure A.6. The polarization behavior of the cells soaked in the two saturated solutions are identical to that of a control soaked in neat APC for 7 days. This result indicates that any layer formed on the Mg anode by the reduction of species in the saturated MCl_x + APC electrolyte does not impede Mg transport or affect deposition and stripping processes. We hypothesize that this is due to Mg^{2+} transport through grain and phase boundaries in the heterogeneous surface layer as has been recently proposed through the SEI formed on Ca largely composed of the insulating CaO phase.[44]

To investigate the chemical reactivity of the active material with the electrolyte in a Mg|MCl_x cell, we assemble Mg|APC|AgCl and Mg|APC|$CuCl_2$ cells and let them rest in the glovebox for 7 days. The cathodes are then extracted, and their pXRD patterns are measured (Figure 2.5). The patterns associated with the pristine electrodes in Figure 2.5(a) and (b) show reflections that can be attributed to the unreacted MCl_x active material. After the cells have rested for 7 days at OCV, the reflections attributed to the chlorides are no longer present even in the case of sparingly soluble AgCl. Instead, the XRD patterns show new reflections that can be attributed to the corresponding metals, indicating chemical reduction of the active material by the electrolyte. Though not quantitative, the low intensity of the Cu metal reflections in Figure 2.5(b) suggests that a substantial portion of the active material is lost, likely deposited on the anode as in Figure 2.4. The APC electrolyte is synthesized from the Grignard reagent PhMgCl. Hypothesizing that unreacted PhMgCl may chemically reduce the active material, we prepared an electrolyte with 20% excess of the Lewis acid $AlCl_3$ to react with any unreacted PhMgCl. We perform an analogous soaking experiment with this modified electrolyte and measure the pXRD pattern of the cathode. The resulting XRD pattern of the cathode from the Mg|AgCl cell shown in Figure 2.5(a) shows reflections for both AgCl and Ag, suggesting that the excess $AlCl_3$ has served to slow but not prevent the chemical reduction of AgCl by the Grignard-containing electrolyte. The chemical reduction of AgCl by the APC electrolyte is likely also a major contributor to capacity fade. Results are similar for $CuCl_2$, as reflections for both $CuCl_2$ and CuCl are present after soaking in the APC electrolyte with excess $AlCl_3$. This result also suggests that the chemical reduction of $CuCl_2$ proceeds through a CuCl intermediate.

We identify three primary drivers of capacity fade in Mg|MCl_x cells: (1) dissolution of the active material by the electrolyte, (2) reduction of dissolved MCl_x by the Mg anode, and (3) chemical reactivity of MCl_x with the Grignard electrolyte. We now

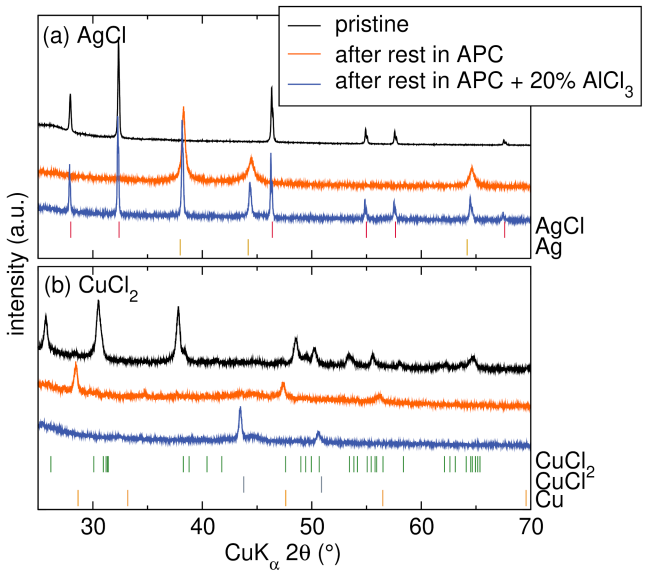

Figure 2.5: Ex situ pXRD patterns for (a) AgCl and (b) $CuCl_2$ cathodes, showing traces for a pristine cathode and cathodes assembled into cells and rested for 7 days with the APC or APC + 20 % $AlCl_3$ electrolyte. APC chemically reduces the metal chloride to the metal. APC + 20% $AlCl_3$ slows the chemical reduction.

attempt to moderate capacity fade in the highly soluble $CuCl_2$ cathode by modifying properties of the electrolyte. Figure 2.6 compares the initial discharge profile and discharge capacities as function of cycle number of a Mg|$CuCl_2$ cell with a conventional APC electrolyte and with modified electrolyte conditions. The reactivity of the APC electrolyte is reduced by adding additional $AlCl_3$ to the electrolyte. The resulting Mg|$CuCl_2$ cycling behavior, however, is minimally changed. Figure 2.6 (b) illustrates discharge capacities for this electrolyte as a function of cycle number, displaying a moderate initial conversion followed by fade at a rate similar to the APC electrolyte, which may be attributed to dissolution of the active material by the electrolyte. To eliminate the Grignard altogether, we use the magnesium-aluminum chloride complex (MACC) electrolyte, which is composed entirely of inorganic salts. The cell barely functions, however, showing minimal redox activity on cycle 1 (Q = 32 mAh/g) followed by polarization. We hypothesize that this low conversion is due to the low conductivity of the relatively low concentration MACC electrolyte. In an effort to address (1) by reducing the solubility of $CuCl_2$ in the electrolyte, we use an electrolyte with much higher salt concentrations in a more viscous G4 solvent. The highly concentrated electrolyte composed of 1.8 M $AlCl_3$ + 0.9 M $MgCl_2$ + 0.9 M $Mg(HMDS)_2$ in G4 shows the highest discharge capacity and the highest capacity at cycle 30 of any electrolyte we investigated. Figure 2.6

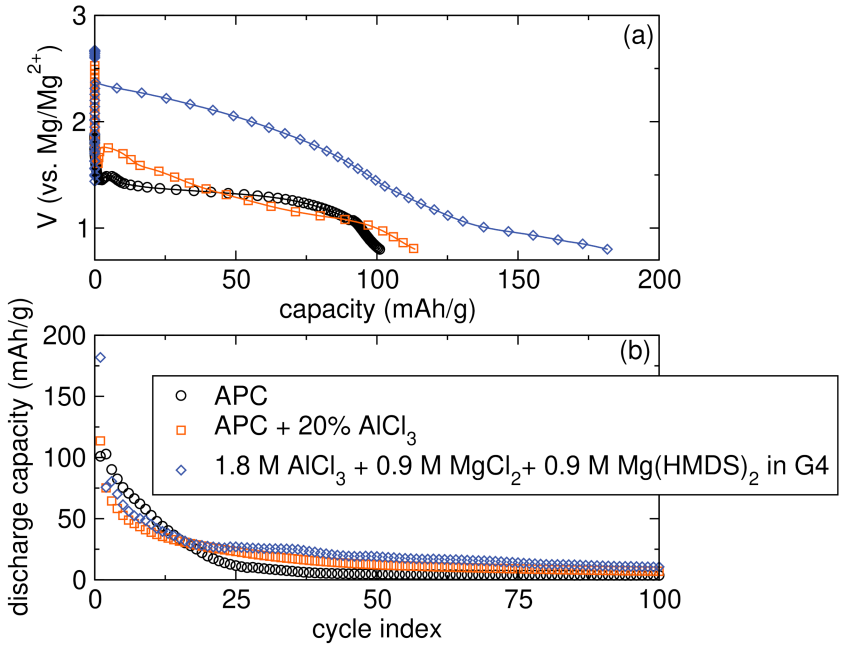

Figure 2.6: (a) First discharge of $CuCl_2$ cells and (b) discharge capacity as function of cycle number for a $CuCl_2$ cathode with a variety of electrolytes. Quenching the Grignard or removing it from the electrolyte while increasing salt concentration moderate capacity fade but does not prevent it in long-term cycling.

(a) shows that the discharge also occurs at a significantly higher voltage than in the cells with Grignard-based electrolytes, potentially due to decreased chemical reactivity with the active material. However, severe capacity fade is still observed. This result suggests that limiting active material dissolution with a highly concentrated, Grignard-free electrolyte may be a suitable avenue for moderating both self discharge and long term capacity fade in Mg|MCl_x cells.

2.5 Conclusions

In this work, we have demonstrated the conversion of a variety of transition metal chlorides based on low-cost, Earth-abundant metals in chloride-based electrolytes with a Mg metal anode. We enabled stable electrochemistry by establishing a cell geometry based on corrosion-resistant Mo current collectors and PTFE body components. Initial percent conversion and capacity retention in these cells are inversely correlated with the measured solubility in THF of the active materials, suggesting that active material dissolution is a major contributor to capacity fade in highly soluble metal chlorides. However, due to the lean electrolyte loading and typical active mass in prepared $CuCl_2$ cathodes, the high solubility of certain metal

chlorides is insufficient to explain the degree of capacity fade in highly soluble metal chlorides. We hypothesized that a shuttle effect is taking place between the MCl_x cathode and the Mg anode, enabling the continuous dissolution of the active material far beyond the quantity necessary to saturate the electrolyte. Resting experiments and subsequent ex situ pXRD characterization revealed that the active material can also be chemically reduced by the electrolyte. Reactivity with the electrolyte was moderated by the addition of 20% $AlCl_3$ to quench unreacted PhMgCl in solution. We hypothesize that chemical reduction and incomplete conversion are a major cause of capacity fade in AgCl cells. Attempts to moderate capacity fade in $CuCl_2$ cells through electrolyte modification showed some success. Increasing salt concentration and the addition of 20% $AlCl_3$ to the APC electrolyte resulted in modest improvements to capacity retention but failed to prevent total capacity fade. This effort demonstrates that future work on this system with a focus on electrolyte design to prevent active material dissolution may yield low fade Mg|MCl_x based on low-cost, Earth-abundant metals.

2.6 Acknowledgments

This research was funded by the President and Director's Research and Development Fund. Part of the work was carried out at the Jet Propulsion Laboratory, California Institute of Technology, under a contract with the National Aeronautics and Space Administration. S.H.S. acknowledges support from the National Science Foundation Graduate Research Fellowship under Grant No. DGE-1745301. SEM and EDS analyses were carried out at the Caltech GPS Division Analytical Facility, which is supported, in part, by NSF Grants EAR-0318518 and DMR-0080065.

Chapter 3

ELECTROCHEMICAL AND ANALYTICAL CHARACTERIZATION OF A HIGHLY STABLE, HALIDE FREE MG ELECTROLYTE BASED ON WEAKLY COORDINATING SILICATE ANIONS

3.1 Abstract

This study presents electrochemical and analytical characterization of a Mg electrolyte based on a weakly coordinating silicate anion with several structural variants. The $Mg[^{Me}Si^{F}{}_{24}]_2$ structural variant is capable of highly reversible Mg plating and stripping with a moderate reductive overpotential. It exhibits the highest oxidative stability limit demonstrated in Mg electrolytes to date as well as high rate capabilities. We observe a trend of increasing steric bulk on the axial ligand resulting in diminished reversibility and limited oxidative stability. The electrolyte is sensitive to impurities, which may limit its use in practical devices.

3.2 Introduction

Li-ion batteries (LIBs) are the current industry standard for electrochemical energy storage.[6, 7] Despite their market dominance, they are based on scarce and unevenly distributed resources. The bulk of the world's Li is concentrated in a small region of South America, with the balance mostly shared by a few large countries.[10] Such concentration of a critical energy resource could spell disaster for global supply chains if this region falls victim to conflict or natural disaster. In fact, the overall supply of Li is projected to be insufficient to meet the demands of an electrifying global economy if we are to aggressively pursue the technologies necessary to combat the worst effects of climate change.[10] Additionally, modern LIBs are approaching the theoretical capacity limit imposed by the number of available crystallographic sites in intercalation-type cathodes.[6] Consequently, attention has shifted to batteries based on Li-metal anodes and conversion-type cathodes. Such Li-metal batteries promise higher energy densities but are plagued by safety concerns related to the dendritic nature of Li plating.[45]

The limited global Li supply and the need for batteries with higher energy densities motivate the development of technologies based on abundant, resource-equitable materials with high energy storage capacities. Mg fits the bill. From a resource

availability point of view, Mg is over three orders of magnitude more abundant than Li in the Earth's crust and is globally widespread in the form of brines and Mg-containing compounds.[12] It is also the second most abundant cation in the ocean after Na.[11] Mg is also appealing from an energy storage point of view. The volumetric capacity of a Mg-metal anode is over four times that of graphite and over double that of Li metal.[19] This property translates into a significantly higher energy density for a cell of a given size. Though not immune to dendritic plating, Mg shows much smoother plating morphologies than Li under the same conditions, promising safer battery operation.[13–15, 18]

The development of Mg batteries is hindered by a lack of compatible electrolytes. Similar to Li, Mg reacts readily with many polar aprotic solvents, common atmospheric components (particularly O_2 and H_2O), and many salt anions (ClO_4^-, BF_4^-, PF_6^-, etc.) to form surface films. Unlike Li, these films do not conduct Mg^{2+} and thereby halt the reversible stripping and plating of Mg^{2+} at the anode.[46–48] The key challenge in the development of Mg electrolytes is thus to find a system that does not form passivating surface films on the Mg surface and supports facile, reversible Mg^{2+} plating and stripping. Early Mg electrolytes were formed by reacting Grignard reagents with Lewis acids such as $AlCl_3$ in tetrahydrofuran (THF).[49] These organohaloaluminate electrolytes showed reversible Mg electrochemistry with excellent Coulombic efficiencies and low reductive overpotentials. Unfortunately, electrolytes based on Grignards chemically react with electrophilic materials and are limited in their anodic stability to < 3.5 V, severely limiting the choice of possible candidate cathode materials.[50] The presence of Cl^- in this class of electrolyte also renders them incompatible with many industrially relevant cell components, such as stainless steel.[51]

Research focus has shifted to non-nucleophilic, halide-free electrolytes to expand the scope of possible cathode materials and cell components. Electrolytes based on $Mg(BH_4)_2$ in ethereal solvents were the first example of an inorganic salt demonstrated to support reversible Mg plating and stripping, though these show low Mg^{2+} conductivity in the absence of a high concentration of Li salts.[52] Analogs to Li electrolytes have also been targeted. Those based on $Mg(PF_6)_2$ display some reductive current but poor reversibility and low Coulombic efficiencies, likely due to the reductive decomposition of the PF_6^- anion forming passivating surface films.[53] Electrolytes based on Mg bis(trifluoromethane sulfonyl)imide ($Mg[N(SO_2CF_3)_2]_2$, $Mg(TFSI)_2$) in glymes have received much interest. Initial results boasted high an-

odic stabilities;[54] however, further experimental and computational studies have revealed high reductive overpotentials and significant decomposition of the TFSI anion.[55–57]

Recent years have seen a focus on bulky, weakly coordinating anions (WCAs). The 12- and 10-vertex monocarboranes $Mg(HCB_{11}H_{11})_2$ and $Mg(HCB_9H_9)_2$ in glymes have been investigated. They show relatively high anodic stabilities between 3.8 and 4.0 V vs. Mg/Mg^{2+} but are unattractive for widespread deployment due to their difficult and costly syntheses.[58, 59] The addition of the more electron-withdrawing F to the C vertex has been shown to increase the oxidative stability of the anion by 300 mV.[60] Alkoxyborates and alkoxyaluminates have shown impressive results. Mg tetrakis(hexafluoroisopropyloxy)borate ($Mg(B(hfip_4)_2)$) has been shown to support reversible Mg plating and stripping in DME with an anodic stability of 3.5 V vs. Mg/Mg^{2+} on Pt.[61] The analogous $Mg(Al(hfip_4)_2)$ was later demonstrated to operate with higher Coulombic efficiencies and lower voltage hysterses in full cells.[62] These hfip-based electrolytes, however, suffer from synthetic reproducibility issues and undergo significant electrochemical conditioning processes.[61–63] The Mg fluorinated pinacolatoborate ($Mg[B(O_2C_2(CF_3)_4)_2]_2$, MgFPB) electrolyte shows an impressive anodic stability of 4.0 V and Coulombic efficiency of 95%.[64]

In this work, we present electrochemical and analytical characterization of a highly stable, halide-free Mg electrolyte based on a weakly coordinating silicate anion ideated and synthesized by the Agapie group (Tianyi He, Meaghan Bruening, and Theodor Agapie).[65]. To our knowledge, the $Mg[^{Me}Si^{F}{}_{24}]_2$ electrolyte represents the highest Mg electrodeposition and stripping current densities and anodic stabilities demonstrated in Mg electrolytes to date. It shows a moderate reductive overpotential of 210 mV and a Coulombic efficiency > 98%. It displays little conditioning behavior, the highest critical current density (5 mA cm^{-2}), and the longest reversible cycling (> 1500 h) demonstrated in halide-free Mg electrolytes to date. We also provide preliminary electrochemical characterization of two structural variants of $Mg[^{Me}Si^{F}{}_{24}]_2$ that are progressively larger and observe a trend of increasing anion bulk and reduced efficiency and reversibility. Finally, we detail several factors which we find necessary to achieve reproducible electrochemical performance from this class of electrolytes.

3.3 Experimental

Electrochemical characterization

Electrolyte salts were synthesized by members of the Agapie lab according to a prior report.[65]. Electrolyte solutions were prepared by dissolving the electrolyte salt and Me_2Mg or Bu_2Mg additive in DME and stirred overnight. The DME was taken from a solvent purification system, freeze-pump-thawed, and stored over 4Å sieves for at least 48 hours before use. Sieves were activated at 220 °C under active vacuum overnight. Glassware was cleaned in a base bath and with aqua regia and dried at 120 °C before being brought into the glovebox. Electrolyte preparation and cell assembly were performed in an N_2-filled glovebox with O_2 and H_2O levels below 0.1 ppm. The glovebox atmosphere was purged for at least 30 minutes prior to handling the electrolyte salt or solvent. The catalyst was sealed during electrochemical characterization. 3Methoxypropylamine (3MPA, Simga, 99%) was distilled and stored over 4Å sieves for at least 48 hours before use.

Mg electrodes (99.9%, MTI) were polished with a razor blade immediately before use. Ca electrodes were polished with a Dremel tool immediately before use. Pt electrodes (wire, 0.5 mm diameter, 99.997%, Thermo Scientific) were soaked in concentrated HNO_3 for at least 72 hours, rinsed, heated with an H_2 torch, and immediately brought into the glovebox.

Cyclic voltammograms were performed in glass cells with 0.5 mL of electrolyte. A Pt wire served as the working electrode, and Mg foils were the counter and reference electrodes. Chronopotentiometry and linear sweep voltammograms were performed in two electrode, 0.5" diameter, Swagelok-type cells with PTFE body components and stainless steel current collectors. Swagelok parts were cleaned by sonication in a 1:1 (vol:vol) acetone:IPA mixture before being pumped into the glovebox. With the exception of long term chronopotentiometry and current sampling experiments, Swagelok cells were assembled in the glovebox and run under ambient atmosphere.

Experiments were conducted on a Biologic SP150, VSP, or VMP3 potentiostat.

Physical characterization

Scanning electron microscopy was conducted on a ZEISS 1550VP field emission SEM with a 15 kV accelerating voltage. SEM samples were prepared in a glovebox but were briefly exposed to air immediately prior to being loaded into the instrument. Pt foil (0.05 mm, 99.99%, Thermo Scientific) served as the substrate for deposition.

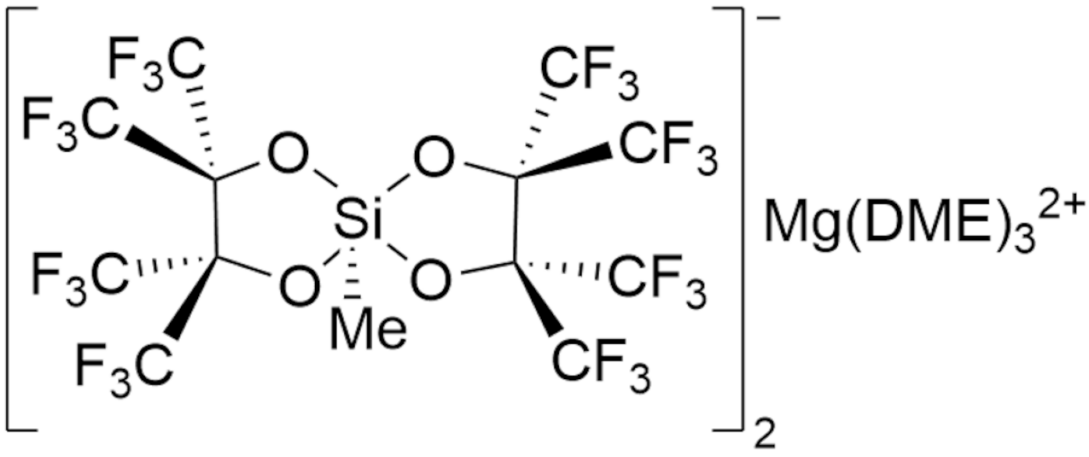

Figure 3.1: Structure of $Mg[^{Me}Si^{F}{}_{24}]_2$ in DME.

3.4 Results and discussion

We begin investigation of the structural variant of the Mg-silicate electrolyte with a methyl axial ligand ($Mg[^{Me}Si^{F}{}_{24}]_2$). The structure of the counteranion is depicted in Figure 3.1. Figure 3.2 illustrates selected cycles of a cyclic voltammogram of 0.25 M electrolyte with 10 mM Me_2Mg additive. Reversible Mg plating and stripping is observed from the first cycle. The initial reductive onset potential is -360 mV vs. Mg/Mg^{2+} with an initial oxidative onset potential of -90 mV vs. Mg/Mg^{2+} for a net reductive overpotential of 270 mV. In cycle 76, the reductive onset potential shits to -260 mV vs. Mg/Mg^{2+}, and the oxidative onset potential occurs at -50 mV vs. Mg/Mg^{2+}, for a net reductive overpotential of 210 mV. We hypothesize that this shift in potential is due to minor interfacial changes which facilitate Mg^{2+} deposition following the initial cycle and to minor shifts in the reference potential. This net reductive overpotential is comparable to or smaller than that of the other halide-free Mg electrolytes, such as $Mg(B(hfip_4)_2$, MgFPB, and carborane-based electrolytes.[61, 64, 68] The Coulombic efficiency of the $Mg[^{Me}Si^{F}{}_{24}]_2$ electrolyte remains stable > 98% for every cycle, showing no major electrochemical conditioning with cycling beyond an increase in current density. Scanning to 5.5 V vs. Mg/Mg^{2+} in cycle 77 reveals no exponential increase in oxidative current density at very positive potentials, typically indicative of anion oxidation or solvent decomposition, until 4.2 V vs. Mg/Mg^{2+}. We hypothesize that the minor increase in current density centered on 3.2 V vs. Mg/Mg^{2+} is related to the oxidation of excess of the alkyl Mg additive (vide infra).

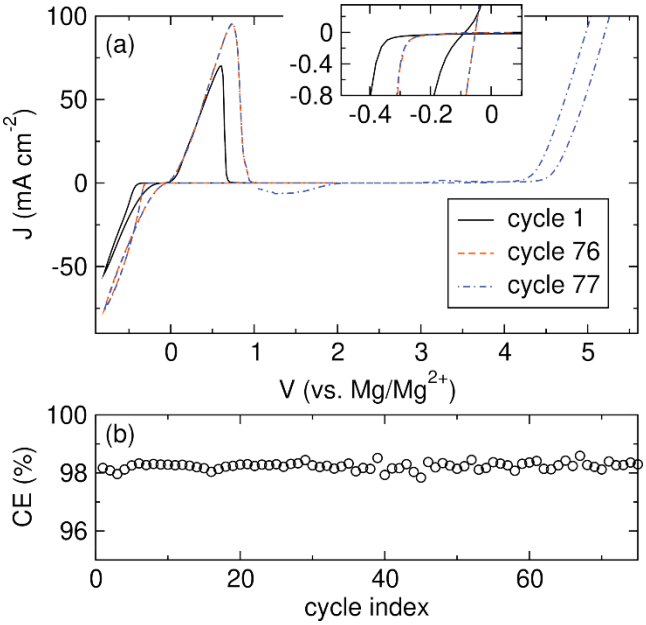

Figure 3.2: (a) Selected cyclic voltammograms of 0.25 M Mg[^{Me}Si$^{F}_{24}$]$_2$ + 10 mM Me_2Mg additive in DME. The inset highlights the deposition overpotential region of the CV. (b) Coulombic efficiency for cycles 1 – 75. The Mg[^{Me}Si$^{F}_{24}$]$_2$ electrolyte shows high efficiencies and minimal electrochemical conditioning.

Based on literature precedent, we hypothesize that the addition of a small amount of Me_2Mg additive serves to scavenge trace impurities such as H_2O and O_2, thereby improving electrochemical performance and resulting in facile, highly efficient Mg electrochemistry from cycle 1.[40, 62, 69, 70] Figure B.1 shows selected CV curves with a range of additive concentrations from 0.5 to 10 mM. There is a clear trend in both the number of cycles of reversible plating and stripping and in the Coulombic efficiency of each cycle, illustrated in Figure B.2, with increasing additive concentration. The electrolyte solution with 10 mM Me_2Mg shows little change in current density or the positions of the reductive and oxidative waves in 75 cycles of reversible Mg plating and stripping. The 10 mM solution also has a stable Coulombic efficiency > 98% for the duration of cycling. By contrast, the reductive and oxidative current densities are significantly lower, and the position of the oxidative wave has shifted to higher potentials with a lower loading of 5 mM. This shift to higher potentials and lower current densities is consistent with passivation by H_2O taking place following reduction. Under this condition, the Coulombic efficiency of the first cycle is 89% but steadily decreases, with little reversible Mg electrochemistry measured by cycle 75. This trend of decreasing additive concentration and increased passivation continues, with the 2 mM additive solution showing a

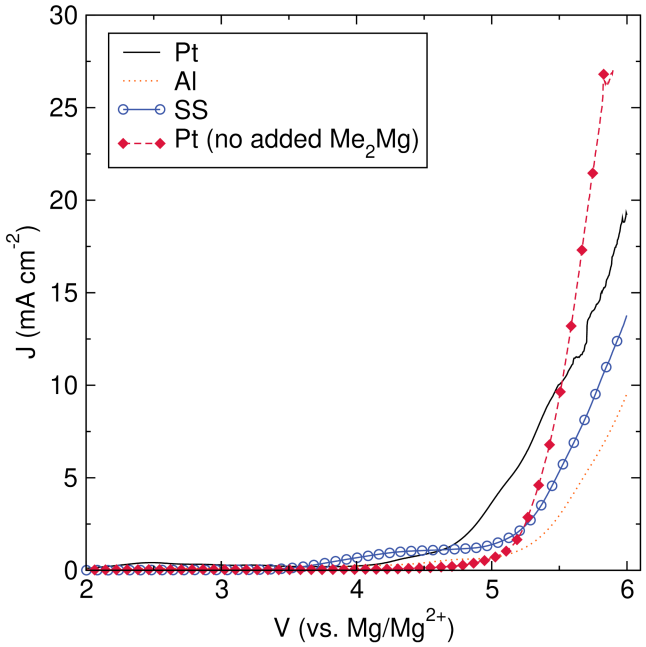

Figure 3.3: Linear sweep voltammograms of 0.25 M $Mg[^{Me}Si^{F}_{24}]_2$ + 10 mM Me_2Mg in DME on Pt, Al, stainless steel 316, and Pt without no added Me_2Mg. Scan rate = 5 mV/s, RE/CE = Mg.

shift in the oxidative potential by cycle 5 and fewer than 25 cycles of reversible Mg electrochemistry. The 0.5 mM additive solution likewise shows progressively increasing reductive overpotentials and limited reversibility.

We performed linear sweep voltammograms with a variety of working electrodes to investigate the impressive oxidative stability shown in Figure 3.2. Figure 3.3 shows LSV curves for 0.25 M $Mg[^{Me}Si^{F}_{24}]_2$ + 10 mM Me_2Mg on a variety of substrates. The measured oxidative current does not increase exponentially until 4.1 V vs. Mg/Mg^{2+} on Pt and 4.9 V vs. Mg/Mg^{2+} on Al and stainless steel. We hypothesize that the low intensity oxidative current before the onset of the exponential increase in current is due to unreacted Me_2Mg additive. To probe this hypothesis, we performed the same experiment with Pt as the working electrode in 0.25 M $Mg[^{Me}Si^{F}_{24}]_2$ electrolyte with no additive. Impressively, the oxidative current does not rise above the baseline until 4.7 V vs. Mg/Mg^{2+} in the absence of any dialkyl Mg additive. To our knowledge, this represents the highest anodic stability measured on Pt in a Mg electrolyte by over 700 mV.[64] The absence of current negative of 4.7 V vs. Mg/Mg^{2+} without the additive supports our hypothesis that the oxidative current measured at 3.2 V vs. Mg/Mg^{2+} in Figure 3.2 is due to unreacted Me_2Mg additive.

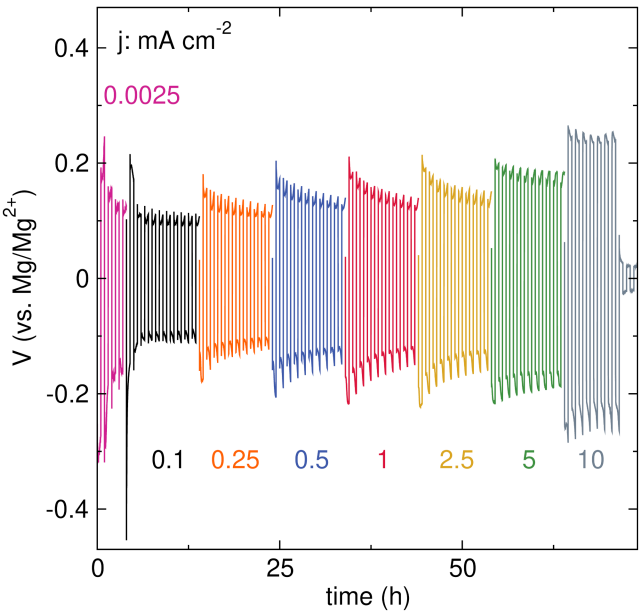

Figure 3.4: Chronopotentiometry traces of symmetric Mg|0.25 M $Mg[^{Me}Si^{F}{}_{24}]_2$ + 10 mM Me_2Mg|Mg cells at a variety of applied current densities.

To evaluate the rate performance of the $Mg[^{Me}Si^{F}{}_{24}]_2$ electrolyte, we assembled symmetric cells with two Mg electrodes and 0.25 M $Mg[^{Me}Si^{F}{}_{24}]_2$ + 10 mM Me_2Mg. Figure 3.4 shows the voltage response of the cell at a variety of applied current densities, following initial conditioning cycles at 0.0025 mA cm^{-2} to prime the Mg surface. Traces for 0.1 mA cm^{-2} and 5 mA cm^{-2} are shown in more detail in Figure B.3. After an initial polarization to -0.47 V vs. Mg/Mg^{2+}, the oxidative and reductive overpotentials at 0.1 mA cm^{-2} are measured at 100 mV. As expected, overpotentials increase with increasing applied current densities, reaching a value of 180 mV at an applied current density of 5 mA cm^{-2}. The overpotential increases to 240 mV at 10 mA cm^{-2} before shorting, manifest in the sudden drop in potential. To our knowledge, this represents the highest critical current density measured in a Mg electrolyte to date.

To investigate the long term cycling stability of the $Mg[^{Me}Si^{F}{}_{24}]_2$ electrolyte, we assembled a symmetric Mg|0.25 M $Mg[^{Me}Si^{F}{}_{24}]_2$ + 20 mM Bu_2Mg|Mg cell. Figure 3.5 illustrates the voltage response with an applied current density of 0.5 mA cm^{-2} alternating between oxidation and reduction in 30 minute intervals for 1500 hours following a conditioning period at 0.0025 mA cm^{-2} for 5 hours. Figure B.4 shows the polarization curves for the first 10 hours and final 10 hours at 0.5 mA cm^{-2}. Following an initial polarization to -0.4 V vs. Mg/Mg^{2+}, the reductive and oxidative

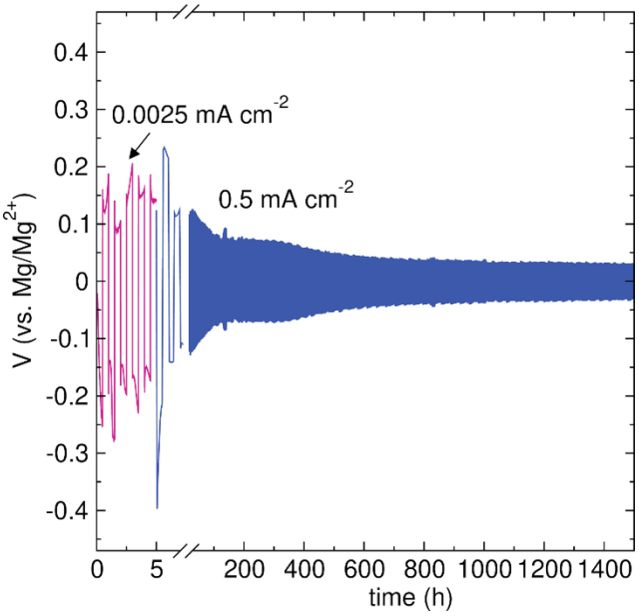

Figure 3.5: Long term chronopotentiometry trace of a symmetric Mg|0.25 M $Mg[^{Me}Si^{F}_{24}]_2$ + 20 mM Bu_2Mg|Mg cell with an applied current density of 0.5 mA cm^{-2} alternating between oxidation and reduction in 30 minute intervals following a conditioning step at 0.0025 mA cm^{-2}.

overpotentials are steady at 100 mV for the first 30 hours of cycling and decrease thereafter, reaching a steady value of 40 mV at 800 hours. We hypothesize that the decrease in overpotential over the course of cycling is due to the formation of a more favorable interface for Mg plating and stripping. The overpotential further decreases to a value of 30 mV in the final 10 hours of cycling, demonstrating the excellent cycling stability of the $Mg[^{Me}Si^{F}_{24}]_2$ electrolyte (Figure B.4). To our knowledge, this is the longest stable cycling behavior demonstrated in a halide-free Mg electrolyte to date.

To examine deposition morphology, we performed a reduction at a rate of -0.5 mA cm^{-2} for 5 hours onto a Pt substrate from a solution of 0.25 M $Mg[^{Me}Si^{F}_{24}]_2$ + 20 mM Bu_2Mg. Figure 3.6 shows the voltage response to the applied reductive current along with the resulting deposition and corresponding elemental analysis. Following an initial polarization to -250 mV vs. Mg/Mg^{2+}, the reduction potential plateaus at -165 mV vs. Mg/Mg^{2+} for the duration of the deposition. The SEM micrograph shows a smooth, even surface characterized by a conformal layer of crystallites on the order of 1 μm in width. Figure B.5 shows a closer view of individual grains. EDS analysis confirms that the deposits are composed of Mg, confirming the reductive stability of the $Mg[^{Me}Si^{F}_{24}]_2$ anion and Mg^{2+} as the mobile

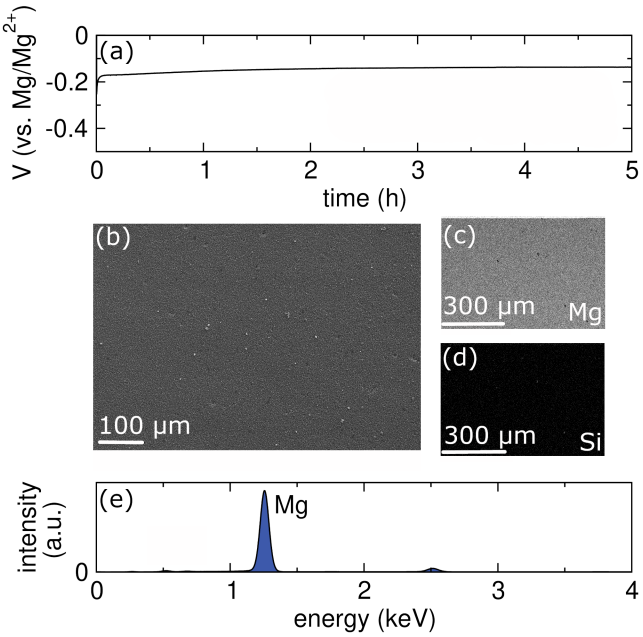

Figure 3.6: (a) Chronopotentiometry trace, (b) SEM micrograph, EDS maps for (c) Mg and (d) Si and the corresponding EDS sum spectrum (bottom) of deposition at -0.5 mA cm^{-2} from 0.25 M $Mg[^{Me}Si^{F}_{24}]_2$ + 20 mM Bu_2Mg for 5 hours on Pt.

ion. We determine the effect of applied current density on deposition morphology by reducing Mg^{2+} onto a Pt substrate by passing 9 C at rates of 0.5, 2.5, and 10 mA cm_2^-. The resulting potential versus time traces are shown in Figure 3.7 (a). As expected, the reductive overpotential increases with the applied current density with average values of -180 mV for -0.5 mA cm^{-2}, -290 mV for -2.5 mA cm^{-2}, and -450 mV for -10 mA cm^{-2}. SEM micrographs of the resulting depositions are illustrated in Figure 3.7 (b), (c), and (d). In each case, we observe a flat surface composed of crystallites on the order of 1 micron in scale. Increasing the current density from -0.5 to -2.5 mA cm^{-2} preserves the compact base layer but also reveals small columnar grains beginning to develop. A further increase in rate to -10 mA cm^{-2} increases the prominence of these columnar features. Continued deposition at this rate is likely to provoke dendritic growth on these sites as the localized electric field of these aspersions encourages further deposition on the peaks. This behavior likely led to the internal short observed at the same rate in Figure 3.4.

Although general electrochemical characterization of $Mg[^{Me}Si^{F}_{24}]_2$ with a minor Grignard additive features many positive characteristics in terms of oxidative stability and deposition morphology and composition, the deposition overpotential around 250 mV remains stubbornly high. In recent years, solvation sheath modi-

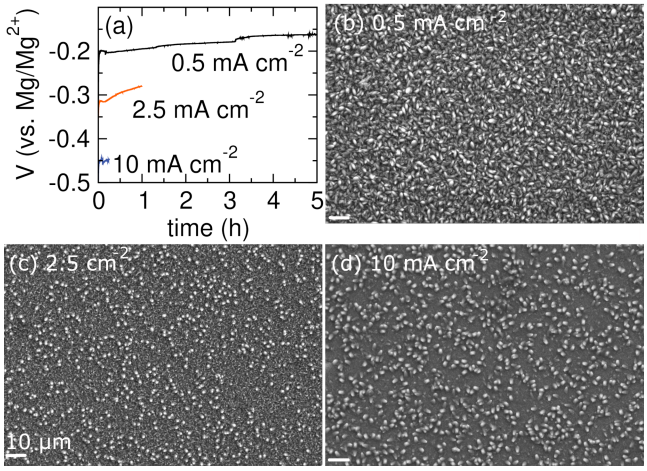

Figure 3.7: (a) Chronopotentiometry traces and corresponding SEM micrographs at (b) -0.5 mA cm^{-2} for 5 hours, (c) at -2.5 mA cm^{-2} for 1 hr, and (d) at -10 mA cm^{-2} for 0.25 hr onto a Pt substrate from 0.25 M $Mg[^{Me}Si^{F}_{24}]_2$ + 15 mM Me_2Mg

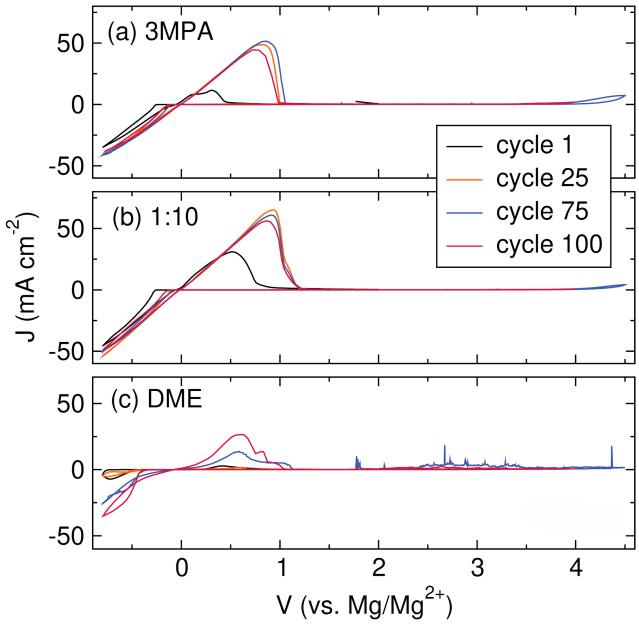

Figure 3.8: Selected cyclic voltammograms of 0.25 M $Mg[^{Me}Si^{F}_{24}]_2$ dissolved in (a) 3MPA, (b) 3MPA:DME 1:10 vol:vol, and (c) DME. 3MPA serves to lower the reductive overpoential of $Mg[^{Me}Si^{F}_{24}]_2$. The use of a mixed solvent system lessens the conditioning process.

fication through the introduction of cosolvents has emerged as a viable method to moderate the overpotential associated with metal plating. What's more, certain of these cosolvents are suggested to have inherent water-scavenging properties, suggesting highly efficient Mg^{2+} deposition without the addition of Grignard additives.[71] Inspired by these findings, we dissolve the $Mg[^{Me}Si^{F}{}_{24}]_2$ to a concentration of 0.25 M in 3-methoxyproplyamine (3MPA). Selected cyclic voltammograms are illustrated in Figure 3.8 (a). The corresponding Coulombic efficiency as a function of cycle index is shown in Figure B.6. The initial cycle with the 3MPA solvent features a reductive overpotential of about 230 mV. The Coulombic efficiency for this scan is low, however, at about 54%. Reductive overpotential progressively decreases and Coulombic efficiency increases with cycling, reaching values of 130 mV and approximately 89% by cycle 25. Minimal oxidative current is observed at high potentials, indicating that 3MPA does not compromise the high oxidative stability of the anion. For comparison, we also cycle $Mg[^{Me}Si^{F}{}_{24}]_2$ with no additive in DME. The resulting voltammograms are shown in Figure 3.8 (c). On cycle 1, $Mg[^{Me}Si^{F}{}_{24}]_2$ in neat DME shows a large reductive overpotential around 750 mV with limited reversibility. Reversible Mg^{2+} plating and stripping does emerge with cycling; however, the Coulombic efficiency is quite erratic. The poor cycling performance of the $Mg[^{Me}Si^{F}{}_{24}]_2$ electrolyte in neat DME suggests that 3MPA may provide a similar water-scavenging function to the Grignard additives, consistent with prior reports of its use as a solvent.

In an effort to retain the positive effect of 3MPA on $Mg[^{Me}Si^{F}{}_{24}]_2$ electrochemistry but also improve the Coulombic efficiency in initial cycles, we used a mixed solvent system, dissolving $Mg[^{Me}Si^{F}{}_{24}]_2$ to a concentration of 0.25 M in 3MPA:DME 1:10 vol:vol. The resulting cyclic voltammograms on a Pt working electrode are shown in Figure 3.8 (b). Similar to the scan in neat 3MPA, the reductive overpotential in the initial scan in 260 mV. Unlike the scan in neat 3MPA, however, the Coulombic efficiency is significantly higher in 3MPA:DME 1:10. Glancing at the Coulombic efficiency as a function of cycle index for this condition in Figure B.6 reveals a dramatically improved conditioning process relative to either of the neat solvents. In the case of 3MPA:DME 1:10, Coulombic efficiency reaches a value of 93% by cycle 3 and remains stable thereafter. We hypothesize that this enhancement of Coulombic efficiency is related to water-scavenging ability of the 3MPA cosolvent to prevent passivating side reactions and the mixed 3MPA:DME solvation sheath in the cosolvent system, which may better facilitate the Mg^0 oxidation process.

Characterization of additional structural variants

Initial electrochemical investigation of the $Mg[^{Ph}Si^{F}_{24}]_2$ (illustrated in Figure B.8) structural variant shows similarly impressive results. Figure 3.8 illustrates selected cyclic voltammograms of 0.25 M $Mg[^{Ph}Si^{F}_{24}]_2$ + 20 mM Bu_2Mg in DME along with the corresponding Coulombic efficiency. Reduction begins at -400 mV vs. Mg/Mg^{2+} on cycle 1 while oxidation occurs at 0 V vs. Mg/Mg^{2+}. By cycle 50, the reductive onset potential shifts to -290 mV vs. Mg/Mg^{2+}, and the oxidative onset potential remains steady at 0 V vs. Mg/Mg^{2+}. Similar to $Mg[^{Me}Si^{F}_{24}]_2$, anodic current begins increasing exponentially at 4.2 V vs. Mg/Mg^{2+}, suggesting that the structural change of the axial ligand from Me to Ph does not significantly change the anodic stability of the electrolyte. Coulombic efficiency remains steady at 98% for the duration of cycling, apart from cycles 65 and 66 which are scanned to a higher upper V cutoff. A small oxidative current arises near 2.8 V vs. Mg/Mg^{2+}, which we attribute to the oxidation of excess of the additive.

We dissolve $Mg[^{Ph}Si^{F}_{24}]_2$ to a concentration of 0.25 M in 3MPA:DME 1:10 to investigate if the amine cosolvent will serve to lower the reductive overpotential for this structural variant. Selected cyclic voltammograms of 0.25 M $Mg[^{Ph}Si^{F}_{24}]_2$ in DME + 15 mM Me_2Mg or in 3MPA:DME 1:10 are shown in Figure B.7 along with their corresponding Coulombic efficiencies as a function of cycle index. The electrolyte in DME with the Me_2Mg additive features minimal electrochemical conditioning and a reductive overpotential around 500 mV throughout cycling. By contrast, the electrolyte with no additive and dissolved in 3MPA:DME 1:10 features an initial reductive overpotential around 500 mV, which then is reduced to merely 110 mV by cycle 75. The increased reductive overpotential with 15 mM Me_2Mg additive relative to 20 mM Bu_2Mg is likely due to small differences in water contents between the solvent and salt batches used across the two experiments. These differences make it difficult to draw firm conclusions about electrochemical properties which may be affected by water passivation. The ability of the amine cosolvent to facilitate reduction is similar to the case of the $Mg[^{Me}Si^{F}_{24}]_2$ structural variant and is likely due in part to water scavenging. Comparing reductive overpotentials of both structural variants in 3MPA:DME 1:10 suggests little effect of changing the axial ligand from Me to Ph on the reductive process.

Considerations for Electrochemical Conditions

Though the $Mg[^{Me}Si^{F}_{24}]_2$ shows many excellent electrochemical properties, our work with the compound has revealed several factors which should be considered

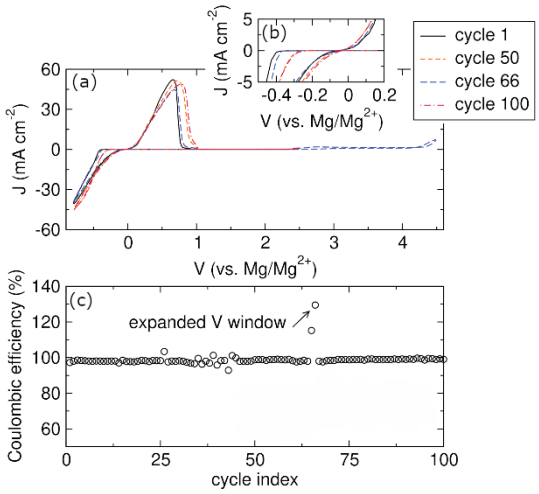

Figure 3.9: (a) Cyclic voltammograms of 0.25 M Mg[$^{Ph}Si^{F}_{24}$]$_2$ + 20 mM Bu_2Mg additive in DME at a scan rate of 25 mV/s. The inset (b) highlights the deposition overpotential region of the CV. (c) Coulombic efficiency for cycles 1 – 100.

in order to reliably reproduce the reported electrochemistry. A chief concern is the cleanliness of the Pt working electrode. Our typical procedure for cleaning and reusing is to thoroughly rinse the used electrode with acetone and deionized water, soak it in concentrated nitric acid for at least 72 hours, rinse it again with deionized water, anneal it with an H_2 flame, and bring it immediately into the glovebox. This protocol has been sufficient to clean and reuse Pt wires in our prior studies of Mg electrolytes. However, in the course of this study, we have found it necessary to use as-purchased Pt wires to achieve consistent electrochemical performance. Figure B.9 compares cyclic voltammograms of 0.25 M Mg[$^{Me}Si^{F}_{24}$]$_2$ + 10 mM Me_2Mg in DME using new and used (and cleaned) Pt working electrodes. The used working electrode results in a shift of the oxidation to higher potentials along with irregular oxidative behavior. To probe the origin of this behavior, we use SEM to image a used and cleaned Pt wire electrode. The resulting SEM micrograph and corresponding EDS maps for Si and O are shown in Figure B.10. The micrograph reveals irregular spots on the Pt surface which are darker in appearance than the bare metal. EDS maps show that these patches are composed of Si and O. The presence of Si could be due to anion decomposition or contamination from the glassware. Since Si and O are observed on the Pt after cleaning, we hypothesize that as the Pt electrode is continually used, the deposits that contain Si and O progressively create an insulating surface film on the Pt electrode. A drop in conductivity of the electrode may prompt further decomposition and undesired side reactions. This behavior may manifest in

the irregular oxidative current observed in Figure B.9. No combination of treatment with strong acids or bases, electrochemical polishing, or mechanical polishing has been successful in removing these deposits.

Another factor which impacts the reproducibility of the electrochemical results is finding an additive concentration which yields reversible Mg^{2+} plating and stripping with high Coulombic efficiency. In Figure B.1, we show highly reversible Mg deposition and stripping with an Me_2Mg concentration of merely 10 mM. Upon trying to reproduce these results with a second batch of solvent and electrolyte salt, we observed a shift in the oxidation to more positive potentials and a decrease in the Coulombic efficiency. Presuming that this result was due to an increased amount of H_2O contamination coming from some combination of the salt, solvent, and glovebox atmosphere, we attempted to remedy the contamination by increasing the additive content. Cyclic voltammograms with Me_2Mg concentrations ranging from 15 mM to 100 mM are illustrated in Figure B.11. The lowest concentrations, 15 and 25 mM, resemble the behavior shown in Figure B.1 with 5 mM additive. The behavior previously observed at 10 mM additive is now only restored at 50 mM additive, presumably because this higher concentration is now necessary to scavenge the elevated amount of H_2O. This result underscores just how sensitive this electrolyte is to small changes in water concentrations but also presents a method for counteracting water contamination.

The final factor necessary to yield reproducible electrochemical data is to use a glovebox with as few other chemicals and tools inside as possible. Initial electrochemical experiments were conducted in a "standard" glovebox containing a myriad of organic solvents, reagents, and samples from a diverse set of projects related to batteries and electrochemistry. In this box, we were occasionally able to observe highly reversible electrochemistry but more often saw the passivating behavior typical of water contamination. We ruled water and oxygen contamination unlikely as the glovebox passed chemical indicator tests with both titanocene and diethyl zinc and the behavior persisted even after 45 minutes of purging the atmosphere. We thus concluded that some other compound must be present in the box atmosphere, even after extensive purging, which similarly serves to contaminate the electrolyte. To address this contamination concern, we repeated the experiments with the same electrolyte and solvent batch in a glovebox that was vacant save for DME and the electrolyte salt and which was purged for 15 minutes prior to handling the electrolyte. The resulting voltammograms are compared with equivalent scans in our "standard"

glovebox after purging for 45 minutes in Figure B.12. Here, we see the oxidation in the "standard" glovebox experiment shifting to more positive potentials and a decrease in the current density with cycling, indicative of passivation. Meanwhile, the experiment conducted in the vacant box shows an increase in current density with cycling and no higher potential oxidation.

3.5 Conclusions

In summary, we have demonstrated an electrolyte based on a Si-centered anion capable of reversibly plating and stripping Mg with the addition of a minor amount of chemical additive. We primarily investigated the structural variant featuring a methyl axial ligand. In CV experiments, it shows high current densities for Mg oxidation and reduction and a moderate reductive overpotential of 210 mV. LSVs show an outstanding anodic stability of 4.7 V vs. Mg/Mg^{2+} on Pt. Chronopotentiometry reveals a critical current density of 10 mA cm^{-2} and stable cycling for 1500 hours, the highest critical current density and longest stable cycling demonstrated in halide-free Mg electrolytes. SEM and elemental analysis confirmed the conformal smooth plating of deposited Mg with no evidence of anion decomposition. We then incorporated an amine cosolvent to lower the reductive overpotential. We have additionally demonstrated initial electrochemical results of two structural variants with increasing bulk the axial ligand on the Si center. These experiments showed a correlation between increasing bulk and reduced oxidative stability and diminished Coulombic efficiency. We then detailed factors which we have found necessary to observe Mg deposition and stripping without significant passivation. Its high oxidative stability may allow researchers to study high voltage Mg cathodes in very controlled conditions.

3.6 Acknowledgments

This work was supported by the Resnick Sustainability Institute. S.H.S. acknowledges support from the National Science Foundation Graduate Research Fellowship under Grant No. DGE-1745301. SEM and EDS analyses were carried out at the Caltech GPS Division Analytical Facility, which is supported, in part, by NSF Grants EAR-0318518 and DMR-0080065.

Chapter 4

ELECTROCHEMICAL AND ANALYTICAL CHARACTERIZATION OF A MG ELECTROLYTE

4.1 Abstract

This study details electrochemical and analytical characterization of a pair of Mg electrolytes based. The WCA-1 electrolyte shows highly efficient Mg plating and stripping with a remarkably low reductive overpotential around 80 mV. This electrolyte exhibits flat Mg deposition morphology but limited performance at faster rates. Increasing the bulk of the anion to yield the WCA-2 electrolyte allows us to study the effect of anion size on electrochemical properties. This change resulted in a modest increase in the reductive overpotential but also an impressive enhancement of performance at faster rates. Although this electrolyte family exhibits limited oxidative stability, it serves as an example of increasing anion bulk as a viable method to enhance the kinetics of Mg electrodeposition. We hypothesize that this performance enhancement is largely due to decreased association between the bulkier anion and solvated Mg^{2+} complexes.

4.2 Introduction

Integral to mobile devices, electric vehicles, and intermittent renewable energy storage, rechargeable batteries have rapidly shifted from an experimental technology in the 1980s to ubiquitous in the modern day.[6] The monumental increase in demand for batteries necessarily drives the demand for the materials that make them. Most commercial rechargeable batteries use Li as a mobile ion which is alternatively intercalated into the anode and cathode to balance the concurrent movement of electrons through an external circuit between the two electrodes to accomplish useful work. Though Li-ion batteries (LIBs) can accommodate hundreds or thousands of charge/discharge cycles with good capacity retention, Li itself is quite rare and is concentrated in just a few regions of the globe.[12] What's more, batteries based on Li^+ intercalation are rapidly approaching the theoretical energy storage limit inherent in intercalation-type chemistries.[7] The development of Li-metal batteries (LMBs) seeks to increase the capacity of Li-based chemistries; however, LMBs are plagued by safety concerns related to the dendritic deposition morphology of Li under relevant conditions, not to mention the fact that LMBs require dramatically

more Li than LIBs, aggravating material supply concerns.[45] For these reasons, it is crucial that we develop battery materials based on more resource equitable, energy dense, safe chemistries.

Mg is an attractive material to supplement the global battery material supply chain. Orders of magnitude more abundant than Li in the Earth's crust, reserves of Mg are globally widespread.[12] It is also the second most abundant cation in the oceans after Na^+.[11] Mg is also promising from an energy storage point of view, as Mg metal anodes have nearly twice the volumetric energy density as Li metal anodes.[7] Mg metal anodes also exhibit flatter deposition morphology than Li metal anodes under the same conditions, suggesting safer operation in the case of Mg.[63, 77]

Although Mg-metal batteries have many attractive qualities, their commercialization is hindered due to a lack of electrolytes which support reversible Mg^{2+} plating and stripping with high efficiency. Like Li, Mg metal is strongly reducing with a tendency to form surface films upon contact with most commonly used organic electrolyte solvents, simple salt anions (PF_6^-, ClO_4^-, etc), and atmospheric contaminants (H_2O and O_2).[49, 78] Due to the sluggish transport of Mg^{2+} through solid phases, these layers typically do not conduct Mg and essentially halt the anode reaction.[39] To combat this tendency towards passivation, many researchers have focused on developing new electrolyte systems that are capable of reversibly plating and stripping Mg with high efficiency without forming an inert interface.

Early Mg electrolytes consisted of Grignard reagents dissolved in an organic solvent with high concentrations of a chloride salt such as $AlCl_3$. These Grignard-based electrolytes typically showed excellent compatibility with the Mg anode and were capable of highly reversible Mg plating with few deleterious side reactions[78, 79]. The exact role of chloride in promoting Mg electrochemistry is not certain, but most work suggests that Cl^- plays a role in protecting the surface of newly deposited Mg from passivation through the formation of a so called chloride rich "enhancement layer."[24, 70] Some results also suggest the transport of $(MgCl)^+$ is enhanced due to the reduced charge density of the monocation relative to the divalent solvated Mg^{2+} complex and that its adsorption to the electrode surface is a necessary step preceding Mg^{2+} reduction in Cl-containing systems.[26, 27, 80]

Despite these advantages, chloride-based systems have important drawbacks. Notably, the high concentration of chloride renders the system highly corrosive and thus incompatible with standard cell body components, namely stainless steel.[51] To overcome this limitation, much work has gone into studying Mg electrolytes which

lack chloride. To this end, electrolytes based on B-centered anions have received great attention. Commercially available $Mg(BH_4)_2$ was demonstrated to plate and strip Mg with high efficiency; however, its anodic stability is limited to just 1.7 V vs. Mg/Mg^{2+} and the overpotential to reduce Mg^{2+} is quite high (> 300 mV).[52] Work then focused on modifying properties of the anion to yield the desired electrochemistry. These efforts typically highlight borates and occasionally the analogous aluminates. A class of Mg-carboranes was developed which showed extremely high anodic stability (> 3.5 V vs. Mg/Mg^{2+}) but retained a stubbornly high reductive overpotential around 250 mV. Despite certain impressive properties, accessing the carboranes requires a difficult synthetic procedure which makes their widespread usage unlikely.[81] Electrolytes based on Mg tetrakis(hexafluoroisopropyloxy)borate ($Mg(B(hfip_4)_2)$) and its aluminate analog support highly efficient Mg plating and stripping with high anodic stabilities.[61] Unfortunately, these systems have rather large reductive overpotentials (> 400 mV) and are plagued by synthetic and electrochemical reproducibility issues.[62, 63] The quest to develop halide-free Mg electrolytes with low reductive overpotentials and high Coulombic efficiencies continues.

This work provides detailed electrochemical and analytical characterization of a pair of halide-free Mg electrolytes based on weakly-coordinating anions ideated and synthesized by the Agapie group (Tianyi He, Meaghan Bruening, and Theodor Agapie). The WCA-1 electrolyte shows outstandingly low deposition overpotentials as well as flat and dense Mg deposits. This variant shows relatively poor performance at faster rates, showing continuously increasing overpotentials at an applied current density of 1 mA cm^{-2} in Mg|Mg symmetric cells. The WCA-2 structural variant bears a bulkier anion and allows us to evaluate the effect of anion size on electrochemical characteristics. This second electrolyte shows a slightly increased reductive overpotential relative to the prior system but displays enhanced performance at faster rates. We attribute this enhancement in kinetic performance to reduced association between the anion and the solvated Mg^{2+} complex. Although a low oxidative stability limits the practical utility of this electrolyte family, the structural insight we gain may be useful in establishing design principles for future Mg electrolytes.

4.3 Experimental

Electrochemical characterization

Electrolyte salts were synthesized by Meaghan Bruening. Electrolyte solutions were prepared by measuring the desired amount of the electrolyte salt in DME and

stirring until dissolved. The DME was taken from a solvent purification system, freeze-pump-thawed before being brought into an Ar-filled glovebox, and then stored over 4Å sieves for at least 48 hours before use. Sieves were activated at 220 °C under active vacuum overnight. Glassware was cleaned in a base bath and with aqua regia and dried at 120 °C before being brought into the glovebox. Electrolyte preparation and cell assembly were performed in a glovebox under an N_2 atmosphere with O_2 and H_2O levels below 0.1 ppm. The glovebox atmosphere was purged for at least 30 minutes prior to handling the electrolyte salt or solvent. The catalyst was sealed during electrochemical characterization.

Mg electrodes (99.9%, MTI) were polished with a razor blade immediately before use. Pt electrodes (wire, 0.5 mm diameter, 99.997%, Thermo Scientific) were soaked in concentrated HNO_3 for at least 72 hours, rinsed, annealed with an H_2 torch, and immediately brought into the glovebox.

Cyclic voltammograms were performed in three-electrode glass cells with 0.5 mL of electrolyte. A Pt wire served as the working electrode, and Mg foils were the counter and reference electrodes. Chronopotentiometry and linear sweep voltammograms were performed in two electrode, 0.5" diameter, Swagelok-type cells with PTFE body components and stainless steel current collectors. Swagelok parts were cleaned by sonication in a 1:1 (vol:vol) acetone:IPA mixture before being pumped into the glovebox. With the exception of long term chronopotentiometry and current sampling experiments, Swagelok cells were assembled in the glovebox and run under ambient atmosphere.

Experiments were conducted on a Biologic SP150, VSP, or VMP3 potentiostat.

Physical characterization

Scanning electron microscopy was conducted on a ZEISS 1550VP field emission SEM with a 15 kV accelerating voltage. SEM samples were prepared in a glovebox but were briefly exposed to air immediately prior to being loaded into the instrument. Pt foil (0.05 mm, 99.99%, Thermo Scientific) served as the substrate for deposition.

4.4 Results and Discussion

With the aim of developing halide-free Mg electrolytes capable of plating and stripping Mg with low overpotentials and high efficiencies, we dissolved WCA-1 in DME. Figure 4.1 shows the 25th cyclic voltammograms of WCA-1 at concentrations of 0.1, 0.25, and 0.5 M in DME. The region showing the reductive overpotential

is highlighted in Figure 4.1 (b). The reductive behavior of each electrolyte concentration is similar. The three concentrations each show a relatively low reductive overpotential less than 100 mV, among the lowest reductive overpotentials demonstrated in a halide-free Mg electrolyte in an organic solvent. Current density trends with increasing electrolyte concentration, likely due to an increased conductivity.

The difference in the oxidative behavior between the three is more stark. The 0.25 and 0.5 M WCA-1 electrolytes display a single oxidative feature which increases linearly in current with increasing potential before rapidly decreasing in intensity as accessible Mg^0 is depleted. By contrast, the 0.1 M WCA-1 electrolyte shows two oxidative features: one which reaches a peak current density at 0.42 V vs. Mg/Mg^{2+} and another at 1.1 V vs. Mg/Mg^{2+}. The presence of this higher potential oxidation is likely due to the oxidation of species related to electrolyte decomposition which takes place in the lower concentration (and lower conductivity) system but not in the higher concentration systems. The Coulombic efficiencies for these scans as a function of cycle index are shown in Figure C.1, which shows efficiencies which generally trend with electrolyte concentration. At 0.1 M, the WCA-1 electrolyte has an Coulombic efficiency of merely 69%, which briefly increases before gradually declining for the duration of cycling. This decline may be related to the progressive consumption of the electrolyte due to side reactions, evident in the higher potential oxidation at this concentration. The 0.25 M WCA-1 electrolyte begins with a much higher Coulombic efficiency around 97% which also gradually declines with cycling, showing that this concentration may also be prone to parasitic side reactions, although to a lesser degree than the 0.1 M electrolyte. The 0.5 M WCA-1 electrolyte displays a cycle 1 Coulombic efficiency of about 94% which gradually increases in early cycles and stabilizes around 98% through cycling. The initial increase in efficiency may be related to electrolytic conditioning processes which prime the electrode surface for future electrodeposition, remove trace impurity species, or some combination of the two.

To probe if the differences in the electrochemistry observed as a function of electrolyte concentration shown in Figure 4.1 are due to differences in conductivity, we perform EIS on WCA-1 electrolytes at a variety of concentrations. The high frequency intercepts of the Nyquist plots, which we take to reflect the charge transfer resistance of the electrolyte, are illustrated in Figure 4.2 (a). Conductivities calculated from these values are displayed in Figure 4.2 (b). As expected, conductivity increases with electrolyte salt concentration, reaching a maximum value of 34 mS

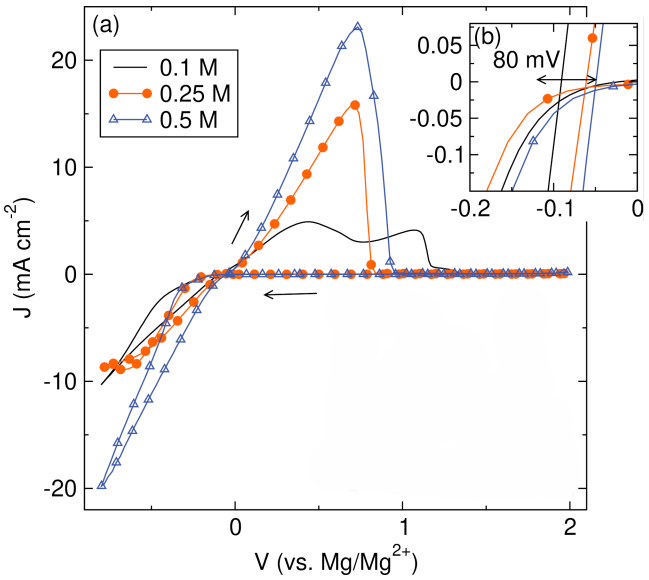

Figure 4.1: (a) Cyclic voltammograms of WCA-1 dissolved in DME to varying concentrations with the inset (b) highlighting the reductive overpotential region. WE: Pt, CE: Mg, RE: Mg. 25 mV s^{-1}. Cycle 25 shown.

cm^{-1} at 0.8 M in DME, on par with reported halide-containing Mg electrolytes.[19] The conductivity decreases slightly at 1 M. This observation is expected and is likely due to the formation of contact ion pairs in the more concentration electrolyte which slows Mg^{2+} transport. Altogether, these results suggest that the differences in current density and oxidative behavior between the different concentrations of WCA-1 in Figure 4.1 are due to differences in conductivity, as 0.5 M has nearly 5x the conductivity of 0.1 M.

To investigate the morphology and composition of depositions from WCA-1, we reduce a Pt electrode in 0.5 M WCA-1 in DME at 0.5 mA cm^{-2} for five hours. The potential vs. time trace is shown in Figure 4.3 (a). The electrode potential quickly drops to -150 mV vs. Mg/Mg^{2+} and remains relatively constant for the duration of the experiment, consistent with a single, well-defined electrochemical process (e.g. Mg^0 deposition). A SEM micrograph of the reduced electrode is shown in Figure 4.3. This image shows a flat surface composed of densely packed hexagonal particles, on the order of several microns in size. The EDS map of Mg shown in Figure 4.3 (c) and the full EDS spectrum displayed in C.2 indicate that this surface is composed essentially entirely of Mg. This result suggests that WCA-1 is capable of Mg^0 deposition with a smooth morphology and without significant electrolyte or solvent decomposition.

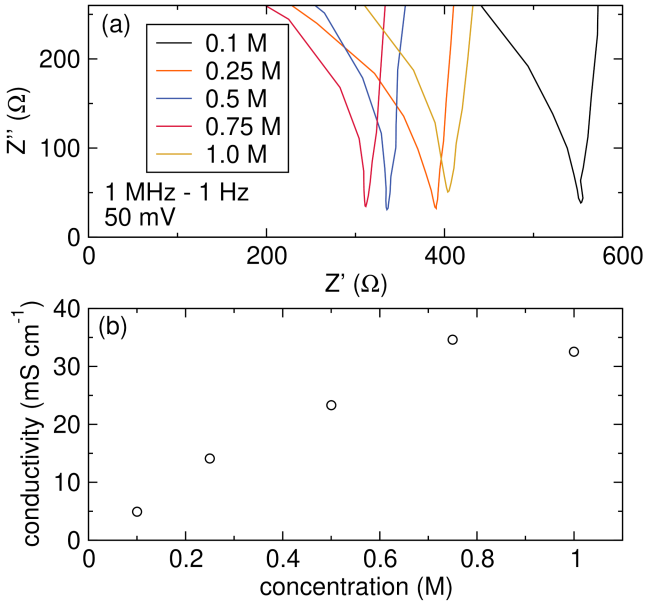

Figure 4.2: (a) EIS spectra at a variety of WCA-1 electrolyte concentrations in DME and (b) the corresponding conductivities calculated from these spectra.

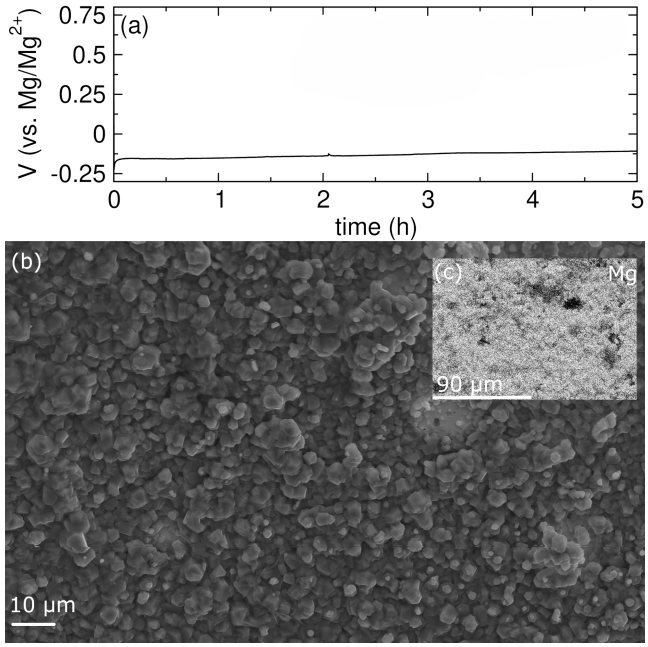

Figure 4.3: (a) Potential vs. time trace of deposition from 0.5 M WCA-1 in DME at a rate of 0.5 mA cm^{-2} for five hours with (b) the corresponding SEM micrograph and (c) the EDS map for Mg. WE: Pt, CE: Mg, RE: Mg.

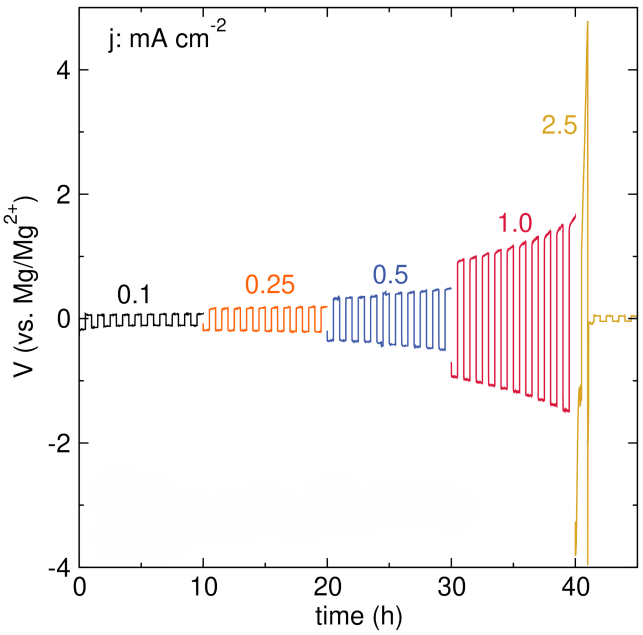

Figure 4.4: Chronopotentiometry of Mg|Mg symmetric cells with 0.5 M WCA-1 in DME at a variety of applied areal current densities ranging from 0.1 mA cm^{-2} to 2.5 mA cm^{-2}.

To determine the critical current density at which deposition from WCA-1 adopts a dendritic morphology, we cycle Mg|Mg symmetric cells at progressively increasing areal current densities. The resulting chronopotentiograms with 0.5 M WCA-1 in DME at current densities ranging from 0.5 mA cm^{-2} to 2.5 mA cm^{-2} are illustrated in Figure 4.4. The curves show low overpotentials (80 mV) for the lowest applied current density. As expected, overpotentials increase with increasing current density, beginning to continually increase at 1.0 mA cm^{-2} and eventually shorting at 2.5 mA cm^{-2}.

Next, we investigate the electrochemistry of a structural variant of WCA-1 featuring a bulkier anion, which we term WCA-2. Cyclic voltammograms of 0.1 and 0.25 M WCA-2 in DME are shown in Figure 4.5 (a). Both concentrations show similar reductive behavior. The region showing the reductive overpotential is highlighted in Figure 4.5 (b). The 0.1 M electrolyte shows a moderate overpotential of 180 mV which is reduced to 110 mV in the 0.25 M electrolyte. These values are larger than reductive overpotentials at the same concentrations for WCA-1 in Figure 4.1, suggesting that the increased steric bulk of the WCA-2 anion may impede electroreduction. The presence of the bulkier anion serves to lower the overall charge density of the anion relative to WCA-1. The lessened charge density likely results

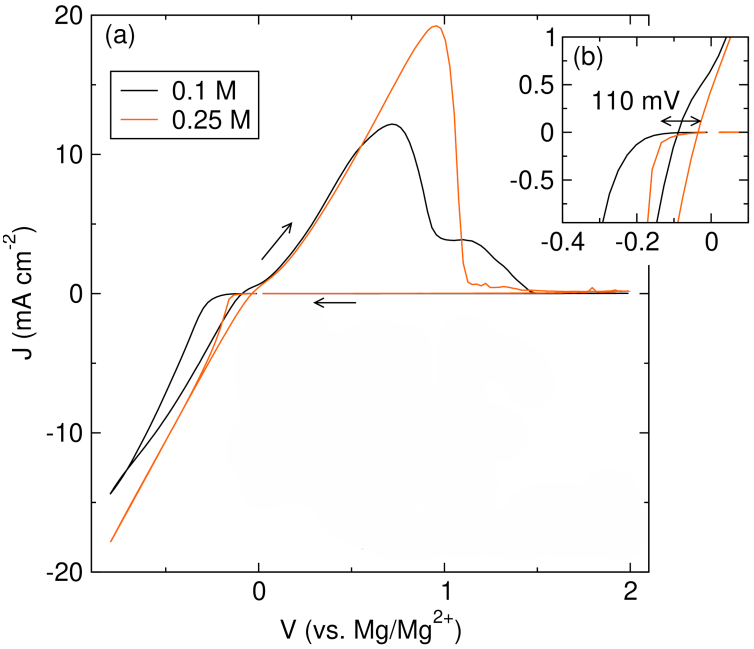

Figure 4.5: (a) Cyclic voltammograms of WCA-2 dissolved in DME to varying concentrations with the inset (b) highlighting the reductive overpotential region and (c) illustrating the anion. WE: Pt, CE: Mg, RE: Mg. 25 mV s^{-1}. Cycle 25 shown.

in a reduced association of the anion with the solvated Mg^{2+} cation. We hypothesize that the relatively more cation-coordinated WCA-1 may serve to stabilize the solvated Mg^{2+} cation and reduce the coordination of solvent molecules. This mixed anion/solvent coordination sphere around Mg^{2+} may lower the thermodynamic barrier for reduction and result in the small reductive overpotentials observed in WCA-1. Introducing a more coordinating anion to reduce solvent coordination has been successfully used to lower reductive overpotentials in divalent electrolyte systems.[82]

The trends in oxidative behavior for WCA-2 at different concentrations are similar to those for WCA-1. The 0.1 M electrolyte displays a pair of oxidations: one with a peak current density at 700 mV vs. Mg/Mg^{2+} and a second at 1100 mV. Unlike WCA-1, the lower potential oxidation is higher in intensity, suggesting that the increased steric bulk of WCA-2 may offer enhanced resistance to reductive decomposition of the anion. The 0.25 M electrolyte shows a single oxidation that increases in current density linearly with potential before rapidly decreasing to the baseline. Figure C.3 shows the Coulombic efficiencies as a function of cycle index of the curves shown in Figure 4.5. The CE for the 0.1 M electrolyte begins around 80%, swiftly increases for a few cycles, and progressively declines from cycle 15

onwards. The 0.25 electrolyte similarly begins around 83% and gradually increases to 88% with cycling. This behavior is similar to the trends in Coulombic efficiency observed in WCA-1, suggesting that the modification to the anion does not have a strong effect on the long term cycleability of the electrolyte in CV experiments.

Next, we examine the morphology and composition of deposits from WCA-2. To this end, we apply a reductive current density of -0.5 mA cm^{-2} to a Pt working electrode immersed in 0.25 M WCA-2 in DME for five hours. The potential vs. time trace of the electrode is shown in Figure 4.6 (a), which shows a stable plateau around -110 mV for the duration of the reduction. Like the case of WCA-1, this behavior is consistent with a single electrochemical process taking place. The surface of the reduced electrode is imaged via SEM in Figure 4.6 (b) with the EDS map for Mg shown in Figure 4.6 (c). Similar to the deposition from 0.5 M WCA-1, the surface is composed of tightly packed hexagonal particles. The EDS map and sum spectrum shown in Figure C.4 indicate that these particles are composed of essentially pure Mg, indicating a good reductive stability of the electrolyte species at this rate. The particle size is larger than those shown in Figure 4.3, but the difference in electrolyte concentration makes it difficult to determine whether this discrepancy is due to the relative differences in conductivity between the two solutions or due to differences in the anion structure. Nonetheless, each electrolyte is capable of Mg^0 deposition with minimal electrolyte decomposition at this rate.

Now we examine the effect of the bulkier WCA-2 electrolyte on the critical current density required to grow dendrites. Accordingly, we cycle 0.25 M WCA-2 in DME in Mg|Mg symmetric cells with progressively greater applied current densities ranging from 0.5 to 5.0 mA cm^{-2}. The resulting potential vs. time traces are shown in Figure 4.7 (a). As expected, overpotentials gradually increase with increasing current density. Unlike the case of WCA-1, overpotentials do not continuously increase with cycling under an applied current density of 1.0 mA cm^{-2}, instead remaining largely stable through cycling. Impressively, the potentials are also stable at 2.5 mA cm^{-2}, where the cell containing the less bulky electrolyte shorted. This result is notable, as it suggests that the bulkier anion supports enhanced kinetic performance despite likely having a lower conductivity due to the difference in electrolyte concentrations. We hypothesize that this enhanced kinetic performance is due to the lower charge density of the $BH(2,6{-}Me4{-}tBuPh)_3$ anion, which effectively reduces the attraction between the anion and the solvated Mg^{2+} complex. This reduced attraction may facilitate faster rates of electrodeposition. The fact that this enhanced performance

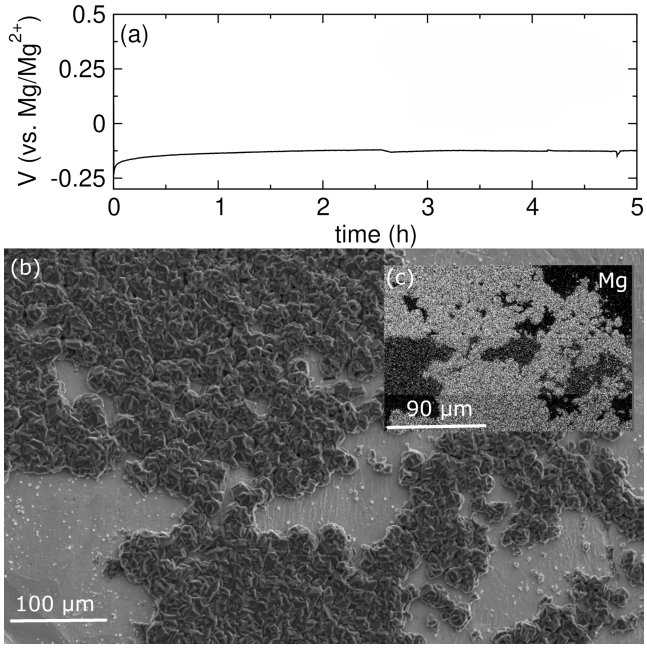

Figure 4.6: (a) Potential vs. time trace of deposition from 0.25 M WCA-2 in DME at a rate of 0.5 mA cm^{-2} for five hours with the corresponding SEM micrograph (b) and the EDS map for Mg (c). This electrolyte supports compact Mg^0 deposition.

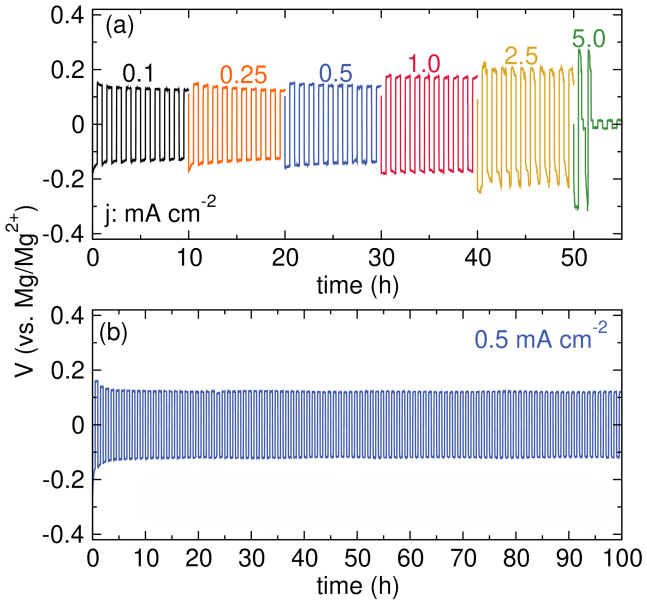

Figure 4.7: (a) Galvanostatic cycling of Mg|Mg symmetric cells with 0.25 M WCA-2 in DME at a variety of applied areal current densities ranging from 0.1 mA cm^{-2} to 5.0 mA cm^{-2} and (b) traces for extended cycling at 0.5 mA cm^{-2}. The bulkier anion shows improved performance at faster rates.

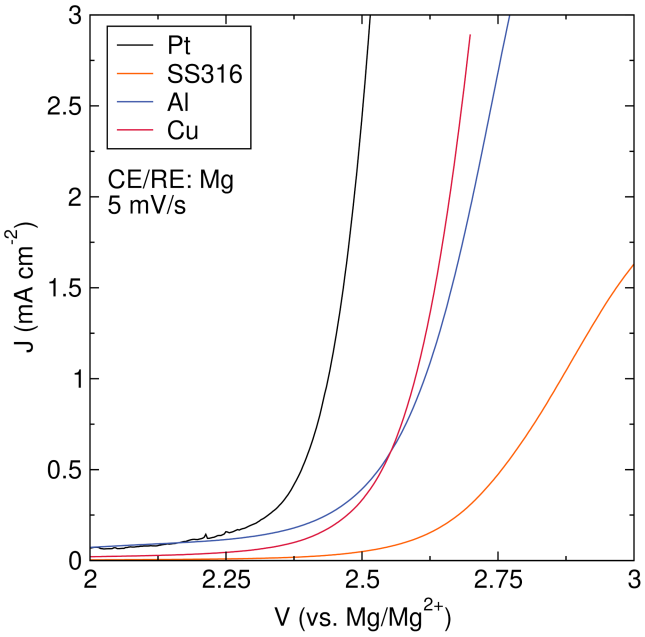

Figure 4.8: Linear sweep voltammograms of 0.25 M WCA-2 in DME at 5 mV s^{-1} on a variety of substrates.The electrolyte shows a relatively low anodic stability. CE/RE: Mg

at faster rates in galvanostatic experiments is coupled with an increased reductive overpotential in CV experiments suggests competing effects of anion bulk on the thermodynamics and kinetics of Mg deposition. To evaluate the long term cycling performance of WCA-2 we likewise cycle Mg|Mg symmetric cells at a rate of 0.5 mA cm^{-2}. The resulting potential vs. time trace is shown in Figure 4.7 (b). Overpotentials begin around 160 mV and quickly drop to 125 mV for the duration of cycling. The stable long cycling suggests excellent reversibility of Mg^0 deposition from WCA-2 without significant side reactions or electrode fouling.

Finally, we determine the oxidative stability of WCA-2 by performing linear sweep voltammograms at 5 mV s^{-1} with a variety of working electrodes. The resulting current vs. potential traces are shown in Figure 4.8. Current begins to rapidly around 2.25 V vs. Mg/Mg^{2+}, indicating a relatively low oxidative stability. Stability is extended on SS316, Al, and Cu relative to Pt but remain low, showing oxidation at 2.6 V on SS316. These results suggest that, despite the excellent kinetic performance and good deposition morphology of WCA-2, the electrolyte stability window is too low to enable the higher voltage cathodes.

4.5 Conclusions

In this study, we have electrochemically and analytically characterized two electrolytes based on halide-free Mg salts with weakly coordinating anions. The WCA-1 electrolyte supports reversible Mg plating and stripping with high Coulombic efficiency at a concentration of 0.5 M in DME. The reductive overpotential at this concentration is around 80 mV, among the lowest reported in halide-free Mg electrolytes. Mg deposited from WCA-1 adopts a dense morphology and does not show evidence of anion or solvent reduction. The kinetic performance of WCA-1 is relatively poor, showing continually increasing overpotentials in Mg|Mg symmetric cells at 1.0 mA cm^{-2} and shorting at 2.5 mA cm^{-2}. A change in steric bulk between the two anions allows us to evaluate the effect of anion size on relevant electrochemical properties. The WCA-2 shows highly reversible Mg electrochemistry at a concentration of 0.25 M in DME. The reductive overpotential is modestly higher at around 110 mV and the size of deposited Mg particles is larger. Nevertheless, the bulkier anion results in improved kinetic performance, which we attribute to reduced association between the anion and solvated Mg^{2+} complexes. Despite this improvement, the WCA-2 electrolyte shows a relatively low anodic stability limit around 2.25 V vs. Mg/Mg^{2+} on Pt.

4.6 Acknowledgments

This work was supported by the Resnick Sustainability Institute. S.H.S. acknowledges support from the National Science Foundation Graduate Research Fellowship under Grant No. DGE-1745301. SEM and EDS analyses were carried out at the Caltech GPS Division Analytical Facility, which is supported, in part, by NSF Grants EAR-0318518 and DMR-0080065.

Chapter 5

REALIZING AL AS A WATER-RESISTANT MG ANODE FOR ENERGY STORAGE

5.1 Abstract

Expanding the library of rechargeable battery chemistries is critical to the transition to a green economy. Magnesium is an attractive battery material, but the development of Mg metal batteries is hindered by the incompatibility of the Mg metal anode with conventional electrolyte solutions and atmospheric contaminants. Mg alloy anodes show improved resistance to passivation; however, the most successful alloy anode, Bi, is relatively scarce and low capacity. Based on its abundance and high theoretical energy density, Al is a good choice as an alloy anode for Mg. Despite its appeal, reversible Mg-Al alloying has not been demonstrated in organic solvents. In this study, we present evidence supporting Mg-Al alloying in a nonaqueous electrolyte. We then enhance the current density of Mg-Al alloying by two orders of magnitude by mechanically alloying Al with Bi. Further, we show that the AB40 alloy tolerates low concentrations of H2O contamination in the electrolyte better than Mg. Though a large particle size limits the alloying capacity of the anode, we show that reducing the particle size can improve the Mg-Al alloying capacity.

5.2 Introduction

The rise in atmospheric CO_2 and its effect on the climate necessitate the increased deployment of carbon-free energy sources as a portion of the global energy-generation portfolio.[1] The production of certain emissions-free energy sources, namely wind and solar, varies greatly with time, as do industrial and personal energy consumption. A major challenge then arises as utilities must match variable energy generation and consumption patterns. Though pumped-hydro still comprises the bulk of modern grid-scale energy storage, the use of batteries on the grid and home scales is growing.[2, 3, 83] Likewise, the infiltration of personal devices powered by rechargeable batteries into daily life continues to spread globally at a fast pace.[84] These trends drive the demand for more batteries and, as a result, the materials that make them.

Lithium-ion batteries (LIBs) are the current industry standard for electrochemical energy storage. Though LIBs have transformed modern life, they alone are not fit to

meet the needs of the growing global battery market. From an energy storage point of view, LIBs are approaching the theoretical capacity limit imposed by intercalation chemistries and are thus unlikely to see more than modest improvements in storage through further development.[6, 7] Lithium-metal batteries promise higher energy densities than LIBs; however, they have yet to be commercialized, in large part due to safety issues associated with the dendritic morphology of Li deposits on the metal anode.[8, 9] Li-based chemistries are also problematic from a resource perspective. Beyond the scarcity, environmental degradation, and human-rights abuses related to the extraction of Ni and Co, key components of many modern LIB cathodes, Li itself is rare and concentrated in a few regions.[10, 85, 86] The development of alternative battery chemistries is thus crucial to meet the demands of the growing market.

Magnesium is an attractive battery material. The divalent nature and compact size of the Mg^{2+} cation endow Mg-metal anodes with nearly double the volumetric capacity of Li-metal anodes (3830 vs. 2060 mAh mL^{-1}).[7] Mg is also known to adopt a smoother deposition morphology than Li under the same conditions, suggesting safer operation for Mg-based batteries.[13–15, 18] What's more, Mg is abundant and globally widespread. It is the eighth most abundant element in the Earth's crust and is present in seawater at a concentration of 1300 ppm, making Mg the most abundant cation in the oceans after Na.[11, 12]

The tendency of Mg-metal anodes to passivate is a major roadblock for the development of Mg-based batteries. Like Li metal, Mg is strongly reducing. It tends to form surface films upon contact with many common organic solvents, atmospheric contaminants (particularly H_2O and O_2), and many salt anions (PF_6^-, ClO_4^-, BF_4^-, etc.).[48, 70, 87] These films typically contain MgO and $Mg(OH)_2$ from reaction with H_2O and O_2 as well as organic species resulting from solvent reduction and phases arising from anion decompsosition such as MgS, MgF_2, and Mg_3N_2. Unlike Li solid electrolyte interphases, these layers typically do not conduct Mg^{2+} and essentially halt the anode reaction.[88–90]

Much work has gone into improving the Mg anode/electrolyte interface by modifying the electrolyte. Grignard- and chloride-based electrolytes have demonstrated excellent compatibility with Mg metal and plate and strip Mg^{2+} with high efficiency. Though these electrolytes work well with the Mg anode, they have a relatively low anodic stability and are highly corrosive, curtailing the number of candidate cathode and cell body materials.[49, 51, 79] Focus has shifted to halide-free electrolytes

with the aim of accessing more positive cathode materials, while still maintaining reversibility at the Mg anode. Electrolytes based on Mg bis(trifluoromethane sulfonyl)imide ($Mg[N(SO_2CF_3)_2]_2$, $Mg(TFSI)_2$) in glymes have received great interest. Early results boasted an expanded anodic stability window; however, further experimental and computational studies have revealed high reductive overpotentials and significant decomposition of the TFSI anion against Mg.[54, 56] Alkoxyborates and the analogous alkoxyaluminates have shown impressive results. Mg tetrakis(hexafluoroisopropyloxy)borate ($Mg(B(hfip_4)_2)$) has been shown to support reversible Mg plating and stripping in DME with an anodic stability of 3.5 V vs. Mg/Mg^{2+} on Pt.[61] Despite their initial promise, these hfip-based electrolytes have shown significant synthetic and electrochemical reproducibility issues.[63]

Though much work has gone into tailoring the electrolyte salt, solvent, and additives to enable facile Mg^{2+} transfer across the anode/electrolyte interface, a class of alloying anodes offers another path forward. The last decade has seen the emergence of several materials, notably Bi[91], Pb[92], Sn[93, 94], In[95], and Sb[91], which may serve as Mg^{2+} hosts through electrochemical alloying reactions. The motivation behind exploring alloying anodes is to reduce the activity of the magnesiated product towards passivating reactions via the formation of some intermetallic compound Mg_aM_b, where a and b are integers whose values depend on the alloying metal M and the degree of magnesiation, rather than Mg^0. Experimentally observed electrochemical alloying reactions typically occur 0.2 - 0.5 V positive of Mg/Mg^{2+}, which may thermodynamically prevent the formation of inert layers that occur at the more negative potentials required for Mg^0 deposition.[96] Though rarely measured in organic solvents, Mg_aM_b intermetallics have also shown slower kinetics for reaction with H_2O than Mg in aqueous solutions.[97–99] These factors suggest that alloying anodes may be less susceptible to passivating reactions by conventional electrolyte components and atmospheric contaminants, potentially unlocking conventional electrolytes for Mg^{2+} conduction and an increase in the power density of Mg-based batteries via more positive cathode materials.[96]

Alloying reactions are common in other battery systems. Researchers in the LIB field have investigated alloy anodes to increase the energy density relative to the commercial standard graphite anode while sidestepping the resource constraints and safety concerns inherent in a Li metal anode. A variety of alloying elements, particularly Si[100], Al[101, 102], Sn[103, 104], Sb[105], Bi[106], Zn[107–109], Cd[108], and Pb[108], have been considered. The large volume change typically associated with

the transition from M to the intermetallic Li_aM_b remains a challenge, as particle fracturing and pulverization prompts dramatic capacity fade with cycling.[110, 111] Na- and K-ion batteries have seen similar efforts.[112] These investigations have primarily targeted Si[113, 114], Sn[115, 116], Ge[117], P[118], Bi[119, 120], and Sb[121] as possible Na or K hosts but likewise tend to report issues related to particle expansion impeding long-term cyclability.[122] The field is not restricted to monovalent working ions. Remarkably, a Sn anode was electrochemically alloyed with Ca to enable the first rechargeable Ca-ion battery at room temperature with a $Ca(PF_6)_2$ electrolyte in conventional carbonate solvents.[123, 124]

The bulk of work on alloy anodes for Mg batteries has focused on Bi and Sn.[96] Bi has received a large amount of academic interest due to the fast kinetics and excellent reversibility of Mg-Bi alloying.[125, 126] Nanostructured Bi has demonstrated a capacity of 350 mAh g^{-1} (88% theoretical) at a rate of 0.05C with a high coulombic efficiency. Increasing the rate to 2C resulted in only a minor reduction in the achieved capacity.[127] Though Bi is capable of high degrees of magensiation with fast kinetics, Mg-Bi alloying occurs at relatively high potentials and with a large charge/discharge voltage hysteresis, diminishing the power of a hypothetical Bi-based cell. Moreover, Bi is quite bulky and relatively rare (0.0085 ppm in the Earth's crust), eliminating the advantages of increased storage capacity and high material abundance promised by Mg-based systems.[93, 96] With a theoretical capacity of 903 mAh g^{-1} and a crustal abundance of 9.8 ppm, Sn seeks to obviate these issues.[12] Unfortunately, Sn shows poor conversion and reversibility at relevant rates.[93, 94, 125, 128] Nevertheless, the desirable characteristics of Sn have led researchers to attempt to improve Mg-Sn alloying kinetics. The primary avenue for this improvement has been bi- or multi-element alloying with other metals which show faster kinetics for Mg-M alloying.[129–132] The mechanism by which the addition of a second or third metal phase improves the performance of the first is not certain but is thought to be interfacial and thermodynamic. Upon initial magnesiation/demagnesiation, certain multielement alloys undergo phase separation, which leads to a decrease in particle size and an increase in surface area.[131, 133] This phenomenon is illustrated in Figure D.1. Other researchers have suggested that the weaker Sn-Sn bonding in SnM alloys enhances Mg^{2+} diffusion in the lattice and the formation of Sn-Mg bonds.[132] Computational studies report that the introduction of Bi into the Sn lattice promotes the Mg-Sn alloying reaction by lowering the defect formation energy which in turn promotes Mg reactivity with Sn.[134]

In this work, we expand scope of Mg alloying anodes to include a new material, Al. In terms of storage and resource properties, Al is something of a holy grail. It is the third most abundant element in the Earth's crust (nearly 4x as common as Mg) and has a theoretical volumetric energy density of 8636 Wh L^{-1} when paired with a hypothetical 3.75 V vs. Mg/Mg^{2+} cathode, higher than that of any Li-intercalation or alloying anode or any other Mg-alloying anode.[96, 135] Mg-Al alloys and intermetallics have also shown reduced corrosion activity by H_2O in aqueous solution and in Mg-air batteries, suggesting that a cell based on Mg-Al alloying at the anode may show greater resistance to passivation by atmospheric contaminants and a better compatibility with conventional electrolyte formulations.[98, 136, 137] Despite these desirable characteristics, electrochemical alloying of Mg and Al has not been reported in nonaqueous systems. This study provides the first evidence for electrochemical magnesiation of Al. We dramatically improve the kinetics of Mg-Al alloying through bimetallic alloying of Al with Bi. Further, we show that the prepared AB40 anode shows reduced passivation by H_2O compared to anodes based on Mg^{2+} reduction. These findings open the door to further exploration of the Mg-Al system for sustainable, high capacity rechargeable batteries.

5.3 Results and discussion

Cyclic Voltammetry of Al with the APC electrolyte

We begin our investigation of Al as an alloy anode for Mg by performing a cyclic voltammogram on an Al powder composite working electrode with the all-phenyl complex (APC) electrolyte. The first, second, and seventy-fifth cycles are displayed in Figure D.2 (a) with the inset (b) highlighting cycle 75. In all electrochemical experiments, we use a separate Mg reference electrode, the potential of which we assume to be near 0 V vs. Mg/Mg^{2+}. All potentials listed hereafter are relative to this reference. The first cycle features a reduction around 0.4 V, with a capacitive current gradually increasing as the lower voltage cutoff approaches. The reverse scan shows no Faradaic features. The lack of reversible redox in the first cycle may be due to the presence some surface layer present on the as-prepared electrode, the reduction of trace impurity species in the electrolyte, or a combination of the two. Commercially available Al powders invariably feature an insulating surface layer of Al_2O_3, which may be removed electrolytically.[138] The second cycle lacks the reduction at 0.4 V and shows lower current density than the first, suggesting that much of the current in cycle 1 is due to the removal of the surface oxide layer. Faradaic peaks emerge and capacitive current continues to decrease with cycling,

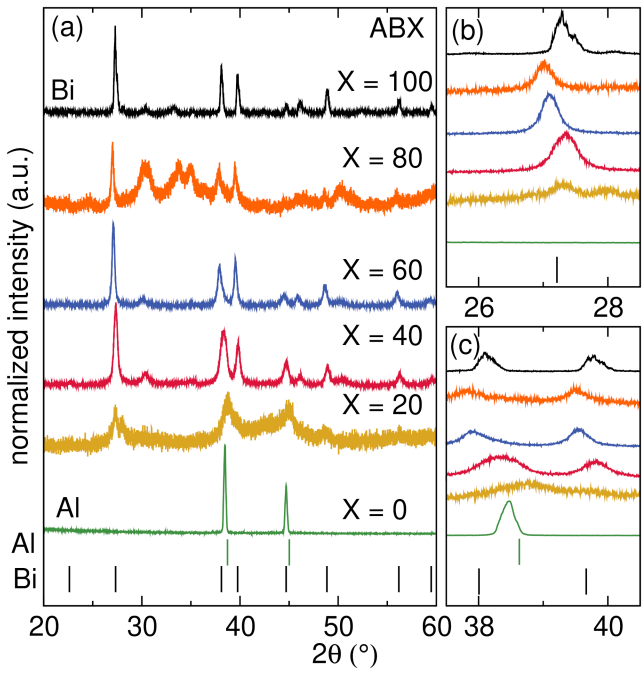

Figure 5.1: (a) XRD patterns of the ABX series, where X = wt% Bi along with highlighted regions that showcase reflections associated with (b) Bi and (c) Al.

consistent with progressive removal of the native oxide and possible surface changes taking place on the electrode. The seventy-fifth cycle shows a cathodic wave around 0.15 V coupled with an anodic wave at 0.3 V. This pair of features could be due to some electrochemical activity of the Al powder; however, the low measured current density (on the order of 0.01 mA/mg) indicates that it is not useful nor worth further characterization.

Mechanical alloying of Al and Bi

We hypothesize that the sluggish kinetics of Mg diffusion in Al prohibits the alloying reaction. Taking inspiration from the efforts to improve Mg-Sn alloying kinetics through bimetallic alloying of Sn, we use mechanical alloying to alloy Al and Bi, since Bi is the material with the fastest reported kinetics for Mg alloying.[96] Mechanical alloying is a solid state processing technique in which precursor powders are combined with milling media and subjected to rapid, repeated, high energy collisions. These collisions drive progressive fracturing and flattening of the precursor particles and subsequent cold welding of these flattened particles. Depending on the milling parameters and the properties of the precursors, this technique can be used to prepare nanocomposites, supersaturated solid solutions, and equilibrium and nonequilibrium amorphous and crystalline phases.[139]

Although Bi is essentially insoluble in Al at room temperature, Uenishi and coworkers used vibration milling to prepare alloys of the two, featuring Bi grains measuring about 30 nm embedded in the Al matrix. By measuring the a lattice parameter of Bi and using Vegard's law, they reported an extended solubility of Al in Bi of 1.9% in Al-30 at.% Bi.[140, 141] Following their example, we combine various ratios of Al and Bi with ZrO_2 media in a high energy ball mill and process them for 20 hours. The resulting materials are named ABX, where X ranges from 0-100 and indicates the wt% of Bi. Figure 5.1(a) shows the XRD patterns for the series ABX with the most prominent reflections for Bi and Al highlighted in Figure 5.1(b) and (c). The pattern for AB80 retains the major Bi reflections at 27.4°, 38.0°, and 39.6°, although several new reflections at 30.4°, 33.7°, 34.8°, and 50.1°appear, with these new reflections likely corresponding to an impurity phase arising from media contamination. The EDS spectra of the ABX alloy series are displayed in Figure D.3. AB80 shows a major Zr impurity which trends inversely with Bi content in the ABX series. The reason for this trend may be that, although the total ball-to-powder mass ratio is constant at all compositions, the volume of metal powder varies significantly due to the large difference in density between Al and Bi. This disparity results in more ball-ball and ball-wall collisions in Bi-rich compositions relative to more Al-rich ones, causing increased media contamination. The patterns for AB60 and AB40 largely resemble that of Bi (X = 100). We do not observe distinct reflections expected for Al at 38.5°or 44.7°, although these peaks may overlap with the nearby reflections for Bi. The reflections highlighted in Figure 5.1(b) and (c) show a slight shift to lower 2θ at X = 80 and progressively move to higher angles at X = 60 and X = 40. These shifts are accompanied by a broadening of all reflections as x decreases on $100 \geq x \geq 40$. These changes are consistent with the prior report of Al-Bi alloying and the formation of a supersaturated solid solution.[141] EDS mapping shown in Figure D.4 reveals a homogeneous distribution of Al and Bi on the micron scale at all compositions. Figure D.5 displays Rietveld refinements of AB60 and AB40 refined to distinct Al and Bi phases. The goodness of fit indicates that Al and Bi domains likely exist, although their size has been refined to below the micron scale. Table C1 lists the lattice parameters calculated from these refinements. Consistent with the previous report of Al-Bi mechanical alloying, the lattice parameters for Bi contract as the Al content increases from AB60 to AB40, consistent with the dissolution of the smaller Al atom into the Bi lattice. In turn, the Al lattice parameter grows as Bi content increases from AB40 to AB60, supporting the dissolution of the larger Bi atom in Al. For comparison, AB40 refined to a single Bi phase is shown

in Figure D.6. The relatively poor fit, particularly near the expected angles for Al reflections, further supports the existence of discrete Al and Bi phases in AB40. Incorporation of additional Bi at X = 20 results in a dramatic loss of crystallinity as all but the most prominent Bi reflections are suppressed. The remaining peaks broaden significantly, reflecting the decrease in crystallinity of the Bi and Al lattices. This loss of crystallinity is also consistent with extended solubility of Al in Bi at higher values of x as additional Al prompts the collapse of the Bi lattice. These observations taken together suggest the formation alloys of Al and Bi and distinct domains of Al and Bi along with extended solid solubility of the two at values of x greater than 40.

Electrochemistry of the Al-Bi alloys

Next, we investigate the effect of Al-Bi alloying on Mg-Al electrochemistry. Investigating the electrochemical properties of an alloy is not always straightforward as the components of the alloy may react individually to form distinct Mg_aM1_b/Mg_cM2_d intermetallics or as a single active material to make a ternary phase of the form $Mg_aM1_bM2_c$. Previous work in multimetallic alloy anodes for Mg tends to report the former mechanism of phase separation followed by stepwise magnesiation,[129, 131, 134, 142] although the latter has also been reported.[143] As an initial probe of the alloying mechanism for the ABX series, we perform cyclic voltammetry with the APC electrolyte. Figure 5.2 (a) shows the seventy-fifth cyclic voltammogram of ABX working electrodes at 1 mV s^{-1}. To facilitate comparison, the same curves are displayed in Figure D.7 with all current densities normalized to the peak oxidative current for a given scan. Cycles 1 - 100 are illustrated in Figure D.8. To get an idea of the potentials at which Mg-Bi and Mg-Al alloying take place, we first examine the pure phases: Bi (X = 100) and Al (X = 0). Bi reveals a single cathodic wave which reaches a peak cathodic current density around 0.06 V. This cathodic wave is coupled to an anodic wave on the positive scan, reaching a peak current density around 0.52 V. This wide hysteresis between reduction and oxidation is typical of Mg-Bi alloying/dealloying, with the cathodic wave representing the formation of Mg_3Bi_2 and the reverse process happening on oxidation.[96] We use this result to assign the region from roughly 0.4 to 0.6 V to Mg-Bi dealloying. Comparison of Bi to Al on the same current density scale shows dramatically reduced activity for Mg alloying in the latter. The normalized scan for Al in Figure D.7 features a cathodic wave at 0.17 V which grows in intensity as the scan approaches the lower voltage cutoff. The reverse scan reveals an anodic wave with a peak current at 0.37 V, which

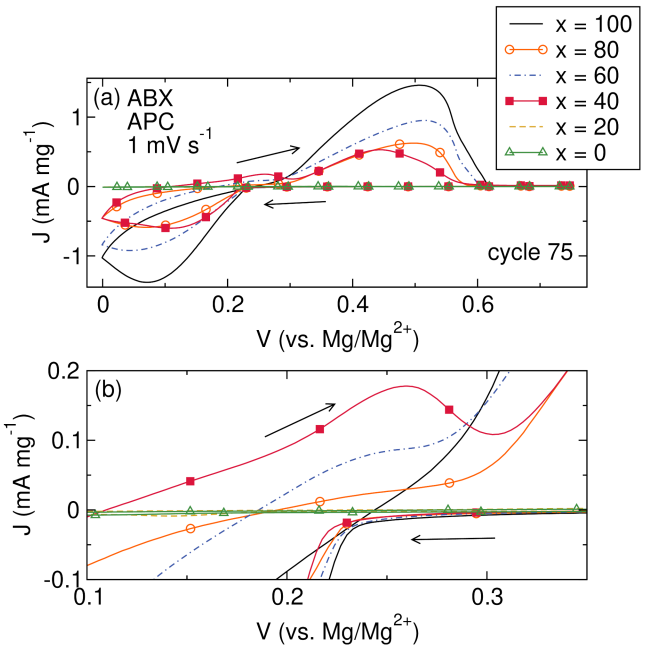

Figure 5.2: (a) Cyclic voltammograms of ABX ($0 \leq x \leq 100$) with the APC electrolyte at 1 mV s^{-1}, (b) a highlight of the region from 0.1 V to 0.4 V.

we hypothesize corresponds to Mg-Al dealloying. From this result, we assign the region from 0.2 V to 0.4 V to Mg-Al dealloying.

AB80 (X = 80) and AB60 (X = 60) show cathodic waves that largely overlap with that of Bi as well as anodic waves shifted slightly negative relative to that of the parent Bi phase. Figure 5.2(b) highlights the region between 0.1 V and 0.4 V. This view reveals a small anodic current in AB80 which increases in intensity in AB60. Since Bi shows essentially no anodic current at this potential and Mg-Al dealloying occurs near this potential in Al, we assign these anodic waves to Mg-Al dealloying in AB80 and AB60. The presence of Mg-Al dealloying implies that some portion of the cathodic wave observed in these materials is due to Mg-Al alloying, despite the absence of a new distinct reductive peak. The single, broad cathodic waves suggest either that Mg-Bi and Mg-Al alloying take place in a concerted fashion in the ABX alloy or that the reactions overlap sufficiently in potential so as to be unable to resolve the two at this scan rate. Similar behavior has been observed in other bimetallic Mg alloying anodes. $In_{0.5}Sn_{0.5}$ displays a single pair of broad reductive and oxidative peaks, and $Pb_{0.4}Sn_{0.6}$ shows multiple cathodic waves followed by a single broad anodic wave.[132]

AB40 (X = 40) continues the trends observed in AB80 and AB60. The Mg-Bi deal-

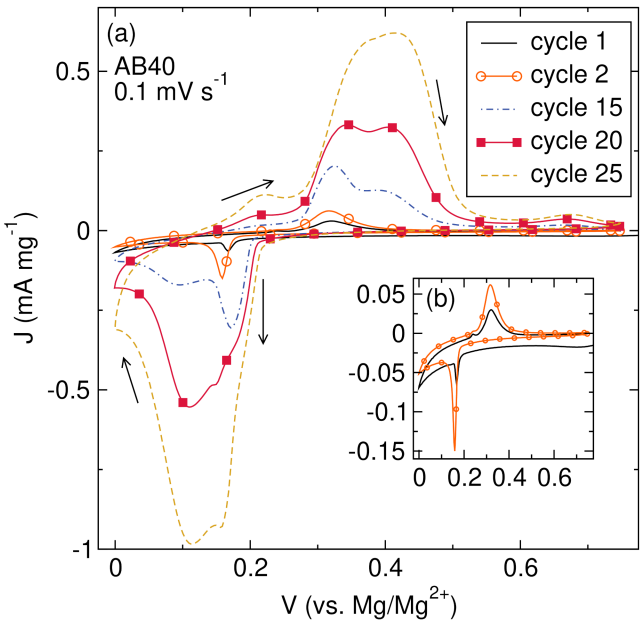

Figure 5.3: (a) Selected cyclic voltammograms of AB40 at 0.1 mV s^{-1} with the APC electrolyte and (b) inset highlighting cycles 1 and 2.

loying peak current shifts further negative to 0.44 V with a distinct Mg-Al dealloying peak appearing at 0.26 V. The cathodic region of the curve features a single broad cathodic wave that reaches a peak around 0.12 V–between the cathodic waves observed in the Bi and Al parent phases. AB20 (X = 20) displays a dramatically lower current density than measured in the previous two alloy phases. The normalized curve shows a cathodic peak around 0.14 V coupled with an anodic wave that nearly overlaps with that of Al, suggesting that the alloying and dealloying currents in this phase are primarily due to Mg-Al activity. The dramatic lowering of current density in AB20 is concurrent with the drop in crystallinity in Figure 5.1. We hypothesize that this loss of order impedes Mg transport within the phase, thereby curtailing the degree of magnesiation and thus the measured current density.

We attempt to deconvolute the cathodic reactions by cycling AB40 at slower rates. Selected cyclic voltammograms for AB40 at 0.1 mV s^{-1} are illustrated in Figure 5.3. Cycle 1 shows a sharp cathodic wave at 0.16 V paired with an anodic wave at 0.33 V, with these features becoming more intense in cycle 2. In cycle 15, the sharp cathodic wave present in cycle 1 has shifted positive to 0.18 V and is now followed by a broad cathodic wave at 0.095 V. The emergence of this broad cathodic wave is accompanied by two new anodic features: a small anodic wave at 0.22 V and a larger, broader one at 0.40 V. The anodic wave at 0.33 V is preserved and becomes

more intense. By cycle 20, the new features at 0.095 V and 0.40 V surpass the initial ones in current as the one at 0.22 V continues to grow. By cycle 25, the cathodic waves are nearly equal in intensity and become difficult to distinguish. The same is true for the anodic waves as 0.33 V and 0.40 V, becoming a single broad feature while the one at 0.22 V becomes more distinct.

To probe if the anodic features at 0.22 V and 0.40 V are coupled with the cathodic wave at 0.095 V, we cycle AB40 at 1 mV s^{-1} with a modified protocol. The potential is swept from 0.75 V to 0 V for 5 cycles, from 0.75 V to 0.1 V for 75 cycles, and finally from 0.75 to 0 V for 75 cycles. The resulting voltammograms are illustrated in Figure D.9. In the initial window, we observe a cathodic wave at 0.16 V and a corresponding anodic wave at 0.33 V. Upon restricting the reductive sweep, we observe a slight decrease in intensity of the anodic wave relative to the previous cycle. Continued cycling in the second window preserves these features but with little change in intensity or position. Again extending the cutoff to 0 V results in the growth of a cathodic shoulder negative of 0.10 V along with the emergence of anodic waves at 0.25 V and 0.45 V. This result suggests that these two anodic waves are indeed coupled with the cathodic wave at 0.095 V.

Similar scans for Bi are included for comparison. In the initial voltage window, Bi shows a cathodic wave at 0.13 V paired with a broad anodic wave with a peak at 0.40 V. This Bi pair undergoes a similar decrease in intensity and position upon initially restricting the lower voltage cutoff, but continued cycling reveals that these features progressively grow in intensity while the cathodic shoulder does not grow in. From the similar potential to features in Bi, we assign the cathodic wave at 0.16 V and anodic wave at 0.33 V in AB40 in Figure 5.3 to Mg-Bi alloying. The presence of a single pair of features for Mg-Bi alloying is expected, as Mg and Bi form a single intermetallic: Mg_3Bi_2. We then assign the cathodic wave at 0.095 V and anodic waves at 0.25 V and 0.45 V to Mg-Al alloying/dealloying. The presence of two distinct anodic waves is consistent with the formation of the two Mg-Al intermetallics: Mg_2Al_3 and $Mg_{17}Al_{12}$.

The progressive growth in current of Bi with cycling under a restricted voltage window is in stark contrast to the behavior of AB40, which remains essentially static in intensity. This observation suggests that only a portion of the Bi in the as prepared AB40 alloy can be magnesiated independent of Al, as accessing the Mg-Al region alloying region negative of 0.10 V is necessary for the continued growth of Mg-Bi features. We hypothesize that cycling ABX to 0.10 V initially

results in magnesiation of Bi domains near the particle surface. Current growth is restricted when accessing only the Bi window because additional Bi in ABX lies behind Al-rich domains. When these Al domains are magnesiated, Mg diffuses further into the material, allowing for the continued growth of both Bi and Al alloying/dealloying current. Structural changes with continued alloying/dealloying likely allow for deeper penetration of Mg into the particle core. SEM micrographs of an AB40 electrode as cast and following 75 CV cycles are displayed in Figure D.11 along with the corresponding EDS maps for Al and Bi. Al/Bi segregation is not evident at this scale, suggesting that Al and Bi clustering remains localized in domains. Based on these observations, we propose the following mechanism for alloying in the Al-Bi system:

$$2Bi + 3Mg^{2+} + 6e^{-} \rightarrow Mg_3Bi_2 \tag{5.1}$$

$$3Al + 2Mg^{2+} + 4e^{-} \rightarrow Mg_2Al_3 \tag{5.2}$$

$$4Al_3Mg_2 + 9Mg^{2+} + 18e^{-} \rightarrow Mg_{17}Al_{12} \tag{5.3}$$

Stepwise formation of Mg_3Bi_2 followed by Mg_2Al_3 and finally $Mg_{17}Al_{12}$ is also consistent with thermodynamic modeling of the Mg-AlBi system.[140]

The lack of clear resolution of the voltammetric features during extended cycling makes quantifying distinct Mg-Bi and Mg-Al alloying/dealloying currents difficult. Instead, we use the peak current density in the Mg-Bi dealloying region as a surrogate for the Mg-Bi activity, though some of this current is likely due to Mg-Al dealloying. We conservatively estimate Mg-Al activity by tracking the peak current of the dealloying feature around 0.25 V in Figure 5.2 (b) as it can be easily distinguished from the Mg-Bi current. Figure D.10 plots these peak dealloying currents as a function of composition normalized to either total alloy or individual metal weight, with the capacitive contribution to the current subtracted. When normalized to alloy weight, Mg-Bi dealloying current generally trends with Bi content in compositions where X > 20. AB80 is an outlier, displaying a lower current density than expected, but this discrepancy is likely due to an overestimation of active loading due to the significant ZrO_2 impurity. When normalized to Bi weight, the Mg-Bi dealloying currents for AB60 and AB40 are unexpectedly high relative to that of pure Bi. One explanation for this elevated intensity is that a significant portion of the current measured in the Mg-Bi dealloying range is in fact due to Mg-Al dealloying due to

the apparent merger of the Mg-Bi dealloying peak at 0.33 V with the Mg-Al one at 0.40 V observed in Figure 5.3.

The Mg-Al current tells a different story. Moving from Al to AB20 results in a slight increase in Mg-Al current density, despite the lowering of Al content. Continuing to decrease Al content to AB40 then yields a two-order-of-magnitude increase in Mg-Al current density. We rationalize this dramatic increase in current density as a small concentration of Bi dissolved in Al acting to improve the kinetics of Mg-Al alloying. This phenomenon is in line with previous studies using Bi or other metals to improve the Mg-alloying kinetics of Sn and Sb.[91, 96, 130–132, 134, 142] A further decrease in Al content to AB60 and AB80 shows a lowering of Mg-Al current density, as expected for lowering Al content. From these results, we see two distinct regimes in the Al-Bi system: the low Al ($< 80\%$) higher crystallinity regime and the high Al ($\geq 80\%$) low crystallinity regime. Al current density in the higher crystallinity regime shows a dramatic increase in Al current density relative to pure Al and decreases with decreasing Al content. Al current density in the lower crystallinity regime is higher than in pure Al despite lower Al content but is significantly lower than in the more crystalline alloys.

We control for the effects of milling itself on these results in two ways: by examining the surface area of the milled particles and by milling Al with a material that itself shows poor kinetics for Mg alloying. Although milling tends to lower the average particle size of most brittle materials, this trend is not always true for ductile materials. Mechanical alloying relies on high energy collisions driving the successive flattening, cold welding, and fracturing of distinct metal particles. The average particle size of the milled alloy can thus be smaller or larger than those of the precursor powders, depending on whether welding or fracturing predominates when milling is stopped.[139, 144–146] We examine the size and morphology of our milled particles compared to the precursor powders via SEM in Figure D.12. The Al powder shown in Figure D.12 (a) is dominated by spheroid particles with a size distribution on the order of 1's - 10's of microns. The Bi powder in Figure D.12 (b) shows a wider size distribution, featuring more particles on the lower end of this same range. The milled powders of AB20 and AB60, illustrated in Figure D.12 (c) and (d), respectively, are dominated by much larger particles with a flat, flaky morphology, some of which are on the order of 100's of microns in scale. Comparing the average particle size of Al, AB20, and AB60 and the current densities observed in Figure 5.2, we can see that the measured Mg-Al dealloying current density does not depend

directly on particle size as one might expect but instead depends on the interplay of relative Al and Bi content while maintaining a high degree of crystallinity. Since we do not observe the expected correlation between smaller particle size and enhanced kinetics, we hypothesize that Bi dissolved in Al acts to lower the thermodynamic barrier for Mg-Al alloying. The activation of Al by Bi despite the increase in particle size is in line with previous results which showed an analogous activation of Sn by Bi dissolved in Sn despite larger particles.[134]

In addition to a decrease in particle size, another possible effect of milling is the accumulation of defects in the Al lattice due to mechanical stress.[147] Prior work has shown that an increase in crystallographic defects can lead to enhanced ionic conductivity in certain systems.[148, 149] To control for this possibility, we mill Al with a material whose intrinsic kinetics for Mg alloying are also poor: Sn. Figure D.13 (a) shows the diffraction pattern of Al60Sn40 prepared in the same way as the Al-Bi series. The reflections for Al and Sn remain distinct after milling, reflecting separate Al and Sn phases. Figure D.13 (b) illustrates the first and tenth cyclic voltammogram of Al60Sn40 with the APC electrolyte at 1 mV s^{-1}. Unlike the Al-Bi materials, Al60Sn40 shows no Faradaic features throughout cycling, indicating no enhanced alloying/dealloying kinetics in either Al or Sn as a result of milling. Thus, the improvement of Mg-Al alloying activity observed in the Al-Bi series is not due to either a particle size reduction via milling or from mechanical stress applied to Al during milling.

To confirm the alloying/dealloying mechanism in AB40, we attempt a bulk conversion by reducing AB40 at C/100 for 100 hours. We then extract the reduced electrode, rinse it with THF, and measure its XRD pattern. The galvanostatic trace of a reduced AB40 electrode is displayed in Figure 5.4 (a) with the corresponding ex situ XRD pattern shown in Figure 5.4 (b). The pattern of a pristine electrode is included for comparison. The galvanostatic trace reveals an initial sloping feature with a small plateau at 0.12 V followed by a second plateau at -0.10 V which does not deplete as the capacity reaches the theoretical value of 955 mAh/g, based on conversion to Mg_3Bi_2 and $Mg_{17}Al_{12}$. Though plateaus are typically observed in constant current conversions of alloy anodes to the magnesiated intermetallic, the potential measured for the primary feature at -0.10 V is more negative than expected for Mg-Al or Mg-Bi alloying.[96] Examining the XRD pattern of the reduced electrode, we see the primary reflections for AB40 preserved at 27.3°, 38.5°, and 39.7°but at a lower intensity than those in the pristine electrode, while no new reflections appear.

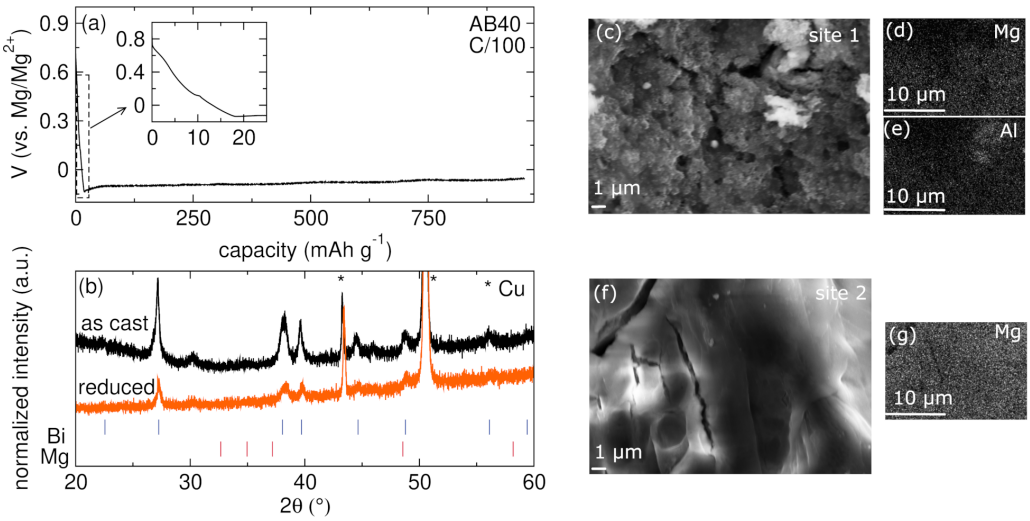

Figure 5.4: (a) Galvanostatic trace of an AB40 electrode reduced at C/100 with the APC electrolyte with inset highlighting initial region and (b) ex situ XRD patterns of the reduced electrode presented with that of a pristine electrode for reference. Reflection positions for Bi and Mg are indicated.(c) SEM micrograph and EDS maps for (d) Mg and (e) Al for one site of the same electrode. (f) SEM micrograph and EDS map for (g) Mg for a second site.

The apparent absence of new reflections is likely due to the low signal-to-noise ratio. Any crystalline products may be in too low abundance to detect, particularly if the reduction yields a distribution of Mg_2Al_3, Mg_3Bi_2, and Mg^0 . Additionally, the most prominent reflection for Mg_2Al_3, the first intermetallic product expected to form for the alloying of Mg and Al, is found at 39.7°, which is not distinguishable from the reflection for Bi found at the same 2θ.

Another explanation for the absence of new crystalline phases after reduction is the formation of nano-sized amorphous Mg_aM_b intermetallics. This latter phenomenon has been observed in other systems. The galvanostatic magnesiation of InSb yields crystalline Mg_3Sb_2 and amorphous MgIn products.[142] Likewise, In-Pb solid solutions form crystalline Mg_2Pb and amorphous MgIn when magnesiated.[150] The full sodiation of SnSb results in amorphous products at room temperature but crystalline ones at an elevated temperature.[151] Based on these reports, the difference in crystal symmetry between the starting materials and magnesiated intermetallics may explain the drive to amorphization in our system. It has been hypothesized that the reason that crystalline MgIn can be formed from reacting InBi and In electrodes with Mg is that each phase belongs to a tetragonal space group (P4/mmm for MgIn and P4/mmm and I4/mmm for InBi and In, respectively). By contrast, In-Sb and In-Pb

have cubic structures. The greater structural rearrangement associated with forming MgIn from a cubic starting material thus tends to result in amorphization.[150] In this study, Al begins in the cubic $Fm\bar{3}m$ space group. Although the most magnesiated phase $Mg_{17}Al_{12}$ is also cubic ($I\bar{4}3m$), the intermediate Mg_3Al_2 is tetragonal ($I4_1/amd$). Similar to the case of In-Pb, the magnesiation of Al may thus result in amorphous products due to this significant structural rearrangement. Amorphization of Mg-Al intermetallics may be driven by possible nanostructuring of Al following Mg-Bi alloying.

We use SEM and EDS to image the same reduced electrode to probe the products of the reduction. Figure 5.4 (c) shows one site of the electrode surface along with corresponding elemental maps for (d) Mg and (e) Al. Here, we see a porous surface in which the active material is largely indistinguishable from the C matrix. Elemental maps show an essentially homogeneous distribution of Al and Mg on this surface. Figure D.14 (a) shows the full EDS spectrum. Here, we find Mg and Al in essentially the same intensity, along with the expected Bi, C, F, and O. The overlay of Al and Mg is consistent with the formation of an alloy phase. Elsewhere on the electrode, we find a dramatically different surface structure and composition. At site 2, imaged in Figure 5.3 (f) with the elemental map for Mg in panel (g), we observe a flatter, partially fractured surface. The full EDS spectrum in Figure D.14 (b) shows that this layer is composed nearly entirely of Mg and O, which is likely due to air exposure prior to imaging. Mg isolated from other electrode components and the negative potential suggest that Mg^0 deposition is taking place during reduction. Still, the presence of interspersed Al and Mg in highly porous sections of the electrode suggests that alloying is occurring in particles on the smaller extreme of the milled AB40 particle size distribution. These observations lead us to hypothesize that both alloying and Mg^0 deposition occur at C/100 in our system, with the lower overpotential features likely corresponding to alloying reactions while the very negative plateau is simply Mg^0 deposition.

We vary the reduction rate to evaluate the effect of kinetics on alloying and product distribution. Galvanostatic traces of AB40 reduced at rates of C/50, C/100, and C/1000 are shown in Figure D.15 (a) along with the corresponding ex situ XRD patterns in Figure D.15 (b). The C/50 trace quickly drops to -0.15 V and plateaus for the duration of the experiment. In contrast to the C/100 experiment, we observe the reflections for Mg^0 expected at 32.6°, 34.9°, 37.1°, 48.5°, and 58.1°, revealing that Mg^0 plating is the primary process happening at this faster rate. The slowest

rate shows a different electrochemical response. At C/1000, small plateaus appear at 0.21 V and -0.05 V before an extended plateau at -0.11 V. We assign these two more positive features to alloying reactions which are more prominent at this slower rate. The extended plateau is likely Mg^0 deposition as in the C/100 case. The XRD pattern of the cell reduced at C/1000 shows an almost total suppression of the reflections for AB40. The small peak at 25.1°is likely due to the formation of Mg_3Bi_2. The presence of crystalline Mg_3Bi_2 is not surprising, as both Bi and Mg_3Bi_2 belong to trigonal space groups ($R\bar{3}m$ and $P\bar{3}m1$, respectively). Another small reflection at 36.6°may indicate either the formation of $Mg_{17}Al_{12}$ (expected at 36.5°) or Mg^0 (expected at 37.1°).

We control for cell configuration and reduction rate by reducing a Bi composite electrode at C/100 and C/20. The resulting galvanostatic traces and ex situ XRD patterns are displayed in Figure D.16. For C/100, the potential vs. capacity trace plateaus around 0.17 V before gradually depleting as theoretical capacity is reached. This behavior is consistent with prior reports of Bi anodes at similar rates.[91] The corresponding ex situ XRD pattern shows that the three most prominent reflections for Bi remain after reduction, but they appear less intense. In turn, several new reflections appear at 22.3°, 24.2°, 25.1°, 38.7°, 46.3°, and 46.8°. These peaks can be indexed to Mg_3Bi_2, the expected magnesiated phase. From this control, we determine that the cell geometry, electrolyte choice, and casting procedure do not impede the alloying of AB40 in Figure 5.4. The electrode reduced at a faster rate shows a different electrochemical response. A small plateau appears at 0.10 V before gradually declining and ending in another plateau at -0.11 V. The XRD pattern for this electrode shows the reflections for Mg_3Bi_2, indicating that alloying remains the primary reaction at this rate, despite the fact that the potential is below 0 V for the majority of the reduction. The changes in the galvanostatic trace for Bi as we increase the reduction rate from C/100 to C/20 are similar to those corresponding to alloying reactions in AB40 as we go from C/1000 to C/100, as plateaus at more positive potentials yield to an extended plateau at -0.11 V. However, this transition occurs at much slower rates for our alloy phase than for the control Bi powder. We hypothesize that this difference is caused by the difference in particle size between the milled alloy and the precursor Bi. Figure D.12 shows that the milled alloy powders have a significantly larger average particle size than does the precursor Bi powder. Prior studies have shown that the rate capability and degree of conversion of Bi depends strongly on particle size and that larger particles with with low surface-area-to-volume ratios tend to alloy only in outer layers, leaving the core inaccessible

.[127] Likewise, work on Sn indicates a strong dependence on size for Mg alloying kinetics.[133] Further, in the study of In-Pb alloying anodes, the large particle size of In-Pb powders produced by mechanical alloying resulted in minimal capacity in galvanostatic experiments. Reducing the particle size by introducing C as a process control agent dramatically increased alloying capacity.[150] Taking these ideas into account, we hypothesize that the current observed in Figure 5.2 is indeed alloying and dealloying of ABX but that the alloying is essentially restricted to smaller particles or the surface of larger ones, leaving the bulk inaccessible due to relatively slow metal diffusion in the large grains of our milled powder. The small plateau feature at 0.12 V in Figure 5.3 (a) may reflect surface alloying which quickly yields to Mg^0 deposition as the surface "shell" fully alloys. Areas of homogeneous Al and Mg distribution found on the electrode surface likely reflect the alloying of minute AB40 particles. As observed in InSb alloying anodes, Mg-Al alloying products may be amorphous when formed under galvanostatic conditions, making identifying them difficult with XRD. These interpretations rationalize the dependence of peak current density on alloy composition in Figure D.10 with the lack of bulk alloying in Figure 5.3.

Resistance of AB40 to passivation by H_2O

Now, we evaluate the resistance of AB40 to passivation by H_2O. To illustrate the effect of H_2O on the deposition and stripping behavior of Mg metal, we evaluate Mg^0 reduction and oxidation on a Pt wire electrode using the MACC electrolyte. Selected cyclic voltammograms are illustrated in Figure 5.5 (a). The well known conditioning process is observed[39] and by cycle 50, the electrolyte supports highly reversible Mg deposition and stripping behavior. Then, water is added to a concentration of 10 mM in the electrolyte. The subsequent CV shows dramatically different behavior with minimal oxidation current and no definable Mg deposition current. Upon cycling, the Mg deposition behavior is retained but the Coulombic efficiency is very low (6.4%). The increased intensity of the reduction coupled with the lower Coulombic efficiency relative to those of the neat MACC electrolyte suggest that the bulk of this reducing current is due to irreversible passivating reactions, rather than the desired Mg^{2+} reduction and oxidation reactions.

We evaluate the vulnerability of AB40 to passivation by H_2O with a modified cycling procedure. We begin from open circuit and scan to -0.25 V at 1 mV s^{-1}. Upon reaching the lower voltage cutoff, the cell rests at open circuit for 60s. Following this rest, an electrochemical impedance spectrum is measured. The scan then continues

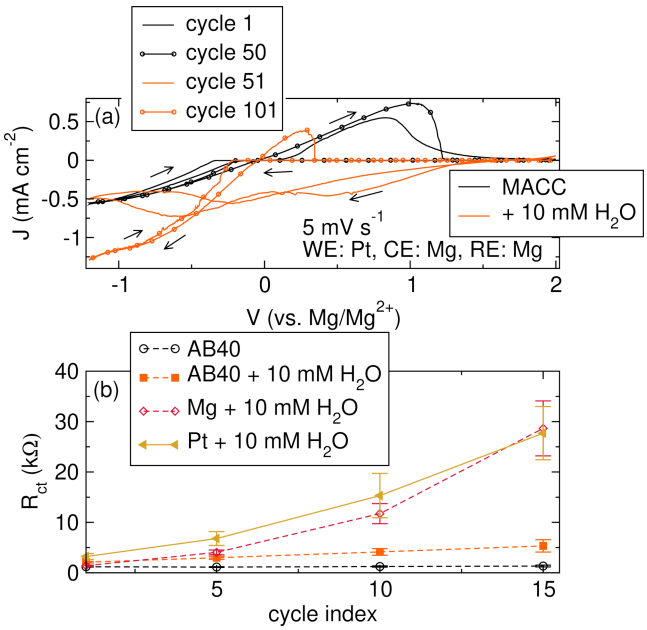

Figure 5.5: (a) Selected cyclic voltammograms of a Pt working electrode with the MACC electrolyte at 5 mV s^{-1} with and without 10 mM H_2O. MACC shows reversible Mg^{2+} plating and stripping. Adding 10 mM H_2O results in irreversible reductions on cycle 1. (b) R_{CT} values measured as a function of cyclic voltammogram cycle number for AB40 in MACC +/- 10 mM H_2O and Mg and Pt in MACC + 10 mM H_2O. Mg and Pt working electrodes show increased R_{CT} with cycling. AB40 is cycled from -0.25 to 0.75 V, Mg is cycled from -0.25 to 0.25 V, and Pt is cycled from -0.75 to 0.75 V

from the lower voltage cutoff, proceeds to the upper voltage cutoff, and repeats the protocol. We choose this procedure because prior investigation into the reaction of deposited Mg^0 with H_2O has found that passivation largely occurs after deposition rather than continuously during the scan.[70] Selected EIS spectra are displayed in Figure D.17 with selected voltammograms plotted in Figure D.18. Taking the x-intercept of the impedance spectrum as a proxy for the charge transfer resistance R_{ct}, we extract these values from the spectra in Figure D.17 and plot them against cyclic voltammogram cycle index in Figure 5.5 (b). Also included are the same values for a bulk Mg^0 working electrode. So as not to convolute the properties of the deposited surface layers with those of underlying bulk Mg^0, we set the upper voltage cutoff for the Mg cell to 0.25 V, where the trace in Figure 5.5 (a) for a Pt working electrode in MACC + 10 mM H_2O at cycle 50 rapidly decreases in current. A glance at the EIS spectra and extracted R_{ct} values in Figure 5.5 (b) for AB40 in MACC shows little increase in impedance with cycling. The addition of H_2O

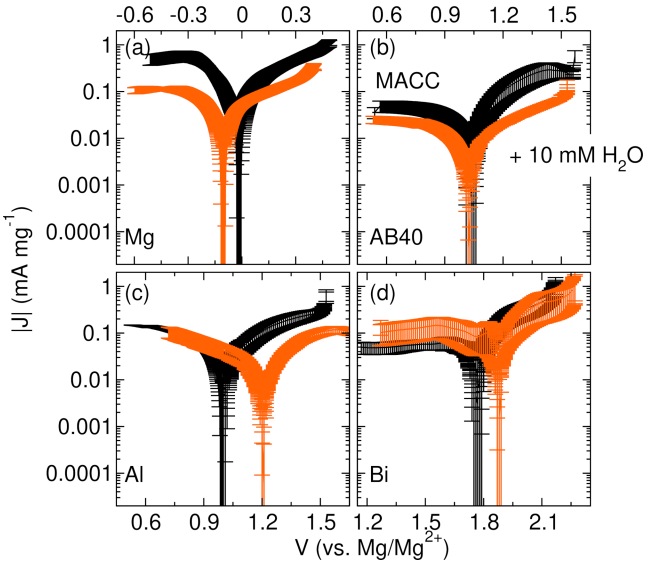

Figure 5.6: Cyclic polarization of (a) Mg, (b) AB40, (c) Al, and (d)Bi with and without 10 mM H_2O. Nobility trends Bi, Al, AB40, and then Mg. AB40 shows the lowest overall corrosion current.

results in a modest linear increase in R_{ct} with cycling, suggesting that AB40 is not totally immune to reaction by H_2O. Nevertheless, the impedance of the Mg cell seems to grow geometrically as a function of cycle number, beginning to outpace those of the AB40 around cycle 5. At cycle 15, R_{ct} for the Mg cell reaches 28.5 kΩ, while that for AB40 with 10 mM H_2O is 5.2 kΩ. To control for the effect of the extended voltage window on the anodic sweep, we also repeat this experiment with a Pt working electrode. In this case, however, we must extend the lower voltage cutoff to -0.75 V due to the increased overpotential for Mg^{2+} deposition on Pt relative to Mg. Nevertheless, Figure 5.5 (b) shows that R_{ct} evolution the Pt electrode largely resembles that of the Mg electrode. Overall, the discrepancy between the results for AB40 and Mg and Pt suggests that Mg is significantly more prone to irreversible passivating reactions with H_2O than AB40.

Next, we explore the kinetic contribution to the resistance of AB40 to passivation by H_2O. To this end, we perform cyclic polarization of AB40, Al, Bi, and Mg in MACC with and without 10 mM H_2O from 500 mV positive of OCV to 500 mV negative of OCV. The absolute value of the measured current is plotted on a log scale against the potential in Figure 5.6. Values are averaged for three replicate cells for each working electrode and electrolyte. Thermodynamically, Bi is the most noble working electrode, followed by Al, AB40, and finally Mg. AB40 has the lowest overall reactivity with H_2O, followed closely by Al. This slow rate of corrosion

relative to that of Mg is in line with previous measurements of Al-based phases in aqueous media.[98, 136] Perplexingly, the MACC control curves show increased current density with Mg and AB40 working electrodes relative to the curves for MACC + 10 mM H_2O for the same working electrodes. Considering the error bars of the cathodic branches, we observe that Mg is the only working electrode under investigation in which the error bars of the curves do not overlap, suggesting that only Mg is significantly affected by the presence of added H_2O. We hypothesize that Mg shows a higher current density without added H_2O because the dominant reaction in this case is Mg^{2+} reduction to Mg^0, which is impeded by the formation of an essentially inert $Mg(OH)_2$/MgO phase when added H_2O is present. This same phenomenon may not occur at rates fast enough to make a measurable difference in AB40, Al, and Bi. This discrepancy between Mg and the other working electrodes is in line with the data present in Figure 5.5, in which AB40 is only minorly affected by added H_2O.

5.4 Conclusions

This study demonstrates electrochemical alloying of Mg and Al in a nonaqueous electrolyte, which is an attractive material for Mg-based energy storage. We improve the inherently sluggish kinetics of this alloying by preparing alloys of Al and Bi. This approach enhances the Mg-Al dealloying current by two orders of magnitude in AB40, despite an increase in average particle size. Due to the large size of the alloy particles, we hypothesize that the beneficial effect of Bi on Mg-Al alloying is primarily thermodynamic in nature. However, we believe that this same increase in particle size limits the bulk alloying of our material at relevant rates. Galvanostatic experiments coupled with ex situ XRD and SEM/EDS measurements demonstrate the interplay between reduction rate and alloying/Mg^0 deposition ratio, the latter of which is favored at faster rates. We posit that bulk conversion may be achieved through further milling to reduce the average particle size below those of the precursor powders. Cyclic voltammetry coupled with EIS measurements shows that AB40 exhibits significantly slower growth in impedance relative to Mg and Pt controls in the presence of added H_2O. Cyclic polarization experiments further show that AB40 has as lower corrosion current than Mg electrodes with added H_2O and that only Mg electrodes were significantly impacted by the addition of H_2O. In all, this study opens the door to the exploration of Al as an abundant, high capacity, water-resistant anode for Mg-based energy storage.

Chapter 6

CONCLUSIONS AND OUTLOOK

Magnesium has a litany of attractive qualities that motivate the development of Mg-based batteries to supplement the global energy storage portfolio. A poor understanding of the physical properties that enable materials and interfaces to reversibly conduct Mg^{2+} hinders the progress of Mg-based chemistries. In particular, the tendency of the Mg metal anode to passivate in contact with conventional electrolyte materials and atmospheric contaminants and the sluggish transport of the divalent Mg^{2+} cation through solid phases represent major roadblocks. This thesis draws on lessons learned in prior studies to explore several material families which are attractive for deployment in MIBs. Our studies aim to elucidate the material properties which prevent irreversible passivation and promote facile Mg^{2+} conduction with high efficiency.

Chapter 2 capitalizes on the positive effect of Cl^- on the Mg metal anode to pair transition metal chlorides based on Earth-abundant metals with a Mg anode and electrolyte. We demonstrate reversible cycling but observe dramatic capacity fade due to active material dissolution and shuttle. Electrolyte modification is then explored as a viable method to moderate capacity fade. As dissolution remains the fatal flaw of Mg|MCl_x battery chemistries, future forays into this field may consider a class of electrolyte which has no capacity to dissolve the active material: solid-state electrolytes. Though the sluggish transport of Mg^{2+} in solid phases makes developing solid-state Mg electrolytes difficult, $MgSc_2Se_4$ has been demonstrated to support Mg conduction with high efficiencies, making it a viable candidate to support the anodic reaction.[152] The cathodic reaction, by contrast, depends on the transport of Cl^- into the electrolyte during discharge. An alternative charge compensation mechanism, however, can be considered. Rather than reducing the MCl_x to M, one can imagine inserting Mg^{2+} into the cathode, resulting in some compound of the form Mg_yMCl_x. An analogous mechanism has been demonstrated in Li|$FeCl_3$ cells, which suggests that Mg intercalation may also be viable although it may be significantly slower than Li^+ insertion.[153] A solid Cl^- conductor can also be considered, but a full cell may be limited by the sluggish conversion of Mg to $MgCl_2$ in the solid state.

Chapter 3 explores the fundamental electrochemistry of a class of Mg electrolytes based on a bulky, weakly coordinating silicate anion. This family displays outstanding electrochemical performance in ideal conditions due to the weakly coordinating nature and outstanding anodic stability of the anion. Overcoming this obstacle likely requires the use of an in situ water scavenger, either in the form of an additive compound which reacts with H_2O to remove it from solution or as a cosolvent which preferentially coordinates H_2O to prevent it from reacting with Mg. The reductive stability of this electrolyte, however, must be examined. Though anion decomposition is not evident during cyclic voltammetry experiments, the presence of Si and O deposits on used Pt electrodes suggests that the anion does indeed react with Mg but at a rate significantly slower than Mg^{2+} deposition so as not to be observed in dynamic experiments. This reactivity should be probed by depositing Mg onto a clean substrate and then allowing the deposited metal to rest in the electrolyte solution. Surface techniques such as SEM/EDS, XPS, and XRD should then be used to probe the speciation of any surface layers that may have formed.

Chapter 4 details electrochemical studies of another family of weakly coordinating anions. These compounds display remarkably low reductive overpotentials but relatively low anodic stabilities. They do provide compelling insight, however, into increasing the bulk of the anion as a means of improving the kinetic performance of the electrolyte. Further study should examine speciation in solution, specifically the relationship between anion-cation and solvent-cation coordination and rate performance. Techniques like Raman spectroscopy and solution-phase NMR are viable for this investigation. This electrolyte system may be viable to pair with low voltage Mg cathodes, such as Mo_6S_8.

Finally, Chapter 5 deploys Al as an alloying anode for Mg-based batteries for the first time. Although the native kinetics for Mg alloying in pure Al are too sluggish for practical applications, we mechanically alloy Al with Bi and observe a two-order-of-magnitude increase in alloying kinetics. A large particle size limits the alloying capacity of the prepared materials, but smaller particles may exhibit higher capacities. Future studies may use extended high energy milling or high energy milling coupled with cryomilling to reduce the average particle size. Smaller particles with higher alloying capacity will enable researchers to confirm the Mg-Al-Bi alloying/dealloying mechanism with bulk techniques such as XRD. Although Bi promotes Mg-Al alloying electrochemistry very well, Bi is itself quite rare and low capacity. Future studies in this field may then consider mechanically alloying

Al with more abundant, higher capacity metals such as In or Pb. An Al-based anode capable of alloying with Mg at fast rates and with high capacity may be compatible with a variety of simple salt Mg electrolytes and be resistant to passivation by H_2O. Such a systems represents a viable platform to investigate high voltage Mg cathodes.

Though rechargeable Mg-based batteries with high energy densities, high efficiency, good capacity retention, and based on materials which can be manufactured at an industrial scale remain hypothetical, this thesis details studies to understand these systems on a fundamental level. By carefully considering various candidate cathode, anode, and electrolyte materials, we uncover material and system properties that are important to enable reversible Mg electrochemistry in different operating scenarios. Accumulating knowledge and experience from these and similar studies will inform future studies and establish the design principles that will yield a commercialized Mg battery.

BIBLIOGRAPHY

[1] Chu, S.; Cui, Y.; Liu, N. The path towards sustainable energy. *Nat. Mater* **2017**, *16*, 16–22, 1.

[2] Yang, Z.; Zhang, J.; Kintner-Meyer, M. C. W.; Lu, X.; Choi, D.; Lemmon, J. P.; Liu, J. Electrochemical Energy Storage for Green Grid. *Chem. Rev.* **2011**, *111*, 3577–3613.

[3] Chowdhury, J. I.; Balta-Ozkan, N.; Goglio, P.; Hu, Y.; Varga, L.; McCabe, L. Techno-environmental analysis of battery storage for grid level energy services. *Renew. Sustain. Energy Rev.* **2020**, *131*, 110018.

[4] Choi, J. W.; Aurbach, D. Promise and reality of post-lithium-ion batteries with high energy densities. *Nat. Rev. Mater.* **2016**, *1*, 1–16, 4.

[5] Whittingham, M.S. Electrical Energy Storage and Intercalation Chemistry *Science* **1976**, *192*, 4244, 1126-1127.

[6] Manthiram, A. A reflection on lithium-ion battery cathode chemistry. *Nat. Commun.* **2020**, *11*, 1550, 1.

[7] Cabana, J.; Monconduit, L.; Larcher, D.; Palacín, M. R. Beyond Intercalation-Based Li-Ion Batteries: The State of the Art and Challenges of Electrode Materials Reacting Through Conversion Reactions. *Adv. Mater* **2010**, *22*, E170–E192.

[8] Bucur, C. B.; Lita, A.; Osada, N.; Muldoon, J. A soft, multilayered lithium–electrolyte interface. *EES* **2016**, *9*, 112–116.

[9] Cheng, X.-B.; Zhang, R.; Zhao, C.-Z.; Zhang, Q. Toward Safe Lithium Metal Anode in Rechargeable Batteries: A Review. *Chem. Rev* **2017**, *117*, 10403–10473.

[10] Greim, P.; Solomon, A. A.; Breyer, C. Assessment of lithium criticality in the global energy transition and addressing policy gaps in transportation. *Nat. Commun* **2020**, *11*, 4570, 1.

[11] Lyman, J.; Fleming, R. Composition of sea water. *J. Mar. Res.* **1940**, *3*.

[12] Hans Wedepohl, K. The composition of the continental crust. *GCA* **1995**, *59*, 1217–1232.

[13] Matsui, M. Study on electrochemically deposited Mg metal. *J. Power Sources* **2011**, *196*, 7048–7055.

[14] Jäckle, M.; Helmbrecht, K.; Smits, M.; Stottmeister, D.; Groß, A. Self-diffusion barriers: possible descriptors for dendrite growth in batteries? *EES* **2018**, *11*, 3400–3407.

[15] Davidson, R.; Verma, A.; Santos, D.; Hao, F.; Fincher, C.; Xiang, S.; Van Buskirk, J.; Xie, K.; Pharr, M.; Mukherjee, P. P.; Banerjee, S. Formation of Magnesium Dendrites during Electrodeposition. *ACS Energy Lett.* **2019**, *4*, 375–376.

[16] Ober, J. A. *Mineral commodity summaries 2016*; USGS Unnumbered Series, 2016; p 205, Code: Mineral commodity summaries 2016 Publication Title: Mineral commodity summaries 2016 Reporter: Mineral commodity summaries 2016 Series: Mineral Commodity Summaries IP-072363.

[17] Elshkaki, A.; Reck, B. K.; Graedel, T. E. Anthropogenic nickel supply, demand, and associated energy and water use. *Resources, Conservation and Recycling* **2017**, *125*, 300–307.

[18] Davidson, R. et al. Mapping mechanisms and growth regimes of magnesium electrodeposition at high current densities. *Mater. Horiz.* **2020**, *7*, 843–854.

[19] Bonnick, P.; Muldoon, J. A Trip to Oz and a Peak Behind the Curtain of Magnesium Batteries. *Adv. Funct. Mater.* **2020**, *30*, 1910510.

[20] Wu, Q.; Shu, K.; Sun, L.; Wang, H. Recent Advances in Non-nucleophilic Mg Electrolytes. *Front. Mater.* **2021**, *7*.

[21] Bieker, G.; Salama, M.; Kolek, M.; Gofer, Y.; Bieker, P.; Aurbach, D.; Winter, M. The Power of Stoichiometry: Conditioning and Speciation of MgCl2/AlCl3 in Tetraethylene Glycol Dimethyl Ether-Based Electrolytes. *ACS Appl. Mater. Interfaces* **2019**, *11*, 24057–24066.

[22] See, K. A.; Chapman, K. W.; Zhu, L.; Wiaderek, K. M.; Borkiewicz, O. J.; Barile, C. J.; Chupas, P. J.; Gewirth, A. A. The Interplay of Al and Mg Speciation in Advanced Mg Battery Electrolyte Solutions. *J. Am. Chem. Soc.* **2016**, *138*, 328–337.

[23] Liao, C.; Sa, N.; Key, B.; K. Burrell, A.; Cheng, L.; A. Curtiss, L.; T. Vaughey, J.; Woo, J.-J.; Hu, L.; Pan, B.; Zhang, Z. The unexpected discovery of the Mg(HMDS) 2 /MgCl 2 complex as a magnesium electrolyte for rechargeable magnesium batteries. *J. Mater. Chem. A* **2015**, *3*, 6082–6087.

[24] Esbenshade, J. L.; Barile, C. J.; Fister, T. T.; Bassett, K. L.; Fenter, P.; Nuzzo, R. G.; Gewirth, A. A. Improving Electrodeposition of Mg through an Open Circuit Potential Hold. *J. Phys. Chem. C* **2015**, *119*, 23366–23372.

[25] Canepa, P.; Gautam, G. S.; Malik, R.; Jayaraman, S.; Rong, Z.; Zavadil, K. R.; Persson, K.; Ceder, G. Understanding the Initial Stages of Reversible Mg

Deposition and Stripping in Inorganic Nonaqueous Electrolytes. *Chem. Mater* **2015**, *27*, 3317–3325.

[26] Benmayza, A.; Ramanathan, M.; Arthur, T. S.; Matsui, M.; Mizuno, F.; Guo, J.; Glans, P.-A.; Prakash, J. Effect of Electrolytic Properties of a Magnesium Organohaloaluminate Electrolyte on Magnesium Deposition. *J. Phys. Chem. C* **2013**, *117*, 26881–26888.

[27] Ta, K.; See, K. A.; Gewirth, A. A. Elucidating Zn and Mg Electrodeposition Mechanisms in Nonaqueous Electrolytes for Next-Generation Metal Batteries. *J. Phys. Chem. C* **2018**, *122*, 13790–13796.

[28] Ratnakumar, B. V.; Stefano, S. D.; Halpert, G. Electrochemistry of Metal Chloride Cathodes in Sodium Batteries. *J. Electrochem. Soc.* **1990**, *137*, 2991.

[29] Lu, X.; Li, G.; Y. Kim, J.; P. Lemmon, J.; L. Sprenkle, V.; Yang, Z. A novel low-cost sodium– zinc chloride battery. *EES* **2013**, *6*, 1837–1843.

[30] Gifford, P. R.; Palmisano, J. B. An Aluminum/Chlorine Rechargeable Cell Employing a Room Temperature Molten Salt Electrolyte. *J. Electrochem. Soc.* **1988**, *135*, 650.

[31] Li, T.; Chen, Z. X.; Cao, Y. L.; Ai, X. P.; Yang, H. X. Transition-metal chlorides as conversion cathode materials for Li-ion batteries. *Electrochim. Acta* **2012**, *68*, 202–205.

[32] Liu, J.-l.; Cui, W.-j.; Wang, C.-x.; Xia, Y.-y. Electrochemical reaction of lithium with CoCl2 in nonaqueous electrolyte. *Electrochem. Commun.* **2011**, *13*, 269–271.

[33] Zhao, X.; Ren, S.; Bruns, M.; Fichtner, M. Chloride ion battery: A new member in the rechargeable battery family. *J. Power Sources* **2014**, *245*, 706–711.

[34] Zhao, X.; Zhao-Karger, Z.; Wang, D.; Fichtner, M. Metal Oxychlorides as Cathode Materials for Chloride Ion Batteries. *Angew. Chem. Int. Ed.* **2013**, *52*, 13621–13624.

[35] Zhang, R.; Ling, C.; Mizuno, F. A conceptual magnesium battery with ultra-high rate capability. *Chem. Commun.* **2015**, *51*, 1487–1490.

[36] Li, X.; Zhang, Y.; Shen, J.; Cao, S.-a.; Li, T.; Xu, F. A High-Rate Rechargeable Mg Battery Based on AgCl Conversion Cathode with Fast Solid-State Mg2+ Diffusion Kinetics. *Energy Technol.* **2019**, *7*, 1900454.

[37] Macrotrends. *Silver Prices - 100 Year Historical Chart*. https://www.macrotrends.net/1470/historical-silver-prices-100-year-chart (accessed 2024-02-09).

[38] Macrotrends. *Copper Prices - 45 Year Historical Chart*. https://www.macrotrends.net/1476/copper-prices-historical-chart-data (accessed 2024-02-09).

[39] Barile, C. J.; Barile, E. C.; Zavadil, K. R.; Nuzzo, R. G.; Gewirth, A. A. Electrolytic Conditioning of a Magnesium Aluminum Chloride Complex for Reversible Magnesium Deposition. *J. Phys. Chem. C* **2014**, *118*, 27623–27630.

[40] Kim, S. S.; Bevilacqua, S. C.; See, K. A. Conditioning-Free Mg Electrolyte by the Minor Addition of Mg(HMDS)2. *ACS Appl. Mater. Interfaces* **2019**,

[41] Zhao-Karger, Z.; Zhao, X.; Wang, D.; Diemant, T.; Behm, R. J.; Fichtner, M. Performance Improvement of Magnesium Sulfur Batteries with Modified Non-Nucleophilic Electrolytes. *Adv. Energy Mater* **2015**, *5*, 1401155.

[42] Cheng, Y.; Liu, T.; Shao, Y.; Engelhard, M. H.; Liu, J.; Li, G. Electrochemically stable cathode current collectors for rechargeable magnesium batteries. *J. Mater. Chem. A* **2014**, *2*, 2473–2477.

[43] Toby, B. H.; Von Dreele, R. B. GSAS-II: the genesis of a modern open-source all purpose crystallography software package. *J. Appl. Crystallogr.* **2013**, *46*, 544–549, 2.

[44] McClary, S. A.; Long, D. M.; Sanz-Matias, A.; Kotula, P. G.; Prendergast, D.; Jungjohann, K. L.; Zavadil, K. R. A Heterogeneous Oxide Enables Reversible Calcium Electrodeposition for a Calcium Battery. *ACS Energy Lett.* **2022**, 2792–2800.

[45] Liu, D.-H.; Bai, Z.; Li, M.; Yu, A.; Luo, D.; Liu, W.; Yang, L.; Lu, J.; Amine, K.; Chen, Z. Developing high safety Li-metal anodes for future high-energy Li-metal batteries: strategies and perspectives. *Chem. Soc. Rev* **2020**, *49*, 5407–5445.

[46] Li, Q.; Chen, J.; Fan, L.; Kong, X.; Lu, Y. Progress in electrolytes for rechargeable Li-based batteries and beyond. *GEE* **2016**, *1*, 18–42.

[47] Aurbach, D.; Gofer, Y.; Lu, Z.; Schechter, A.; Chusid, O.; Gizbar, H.; Cohen, Y.; Ashkenazi, V.; Moshkovich, M.; Turgeman, R.; Levi, E. A short review on the comparison between Li battery systems and rechargeable magnesium battery technology. *J. Power Sources* **2001**, *97-98*, 28–32.

[48] Aurbach, D.; Gofer, Y.; Schechter, A.; Chusid, O.; Gizbar, H.; Cohen, Y.; Moshkovich, M.; Turgeman, R. A comparison between the electrochemical behavior of reversible magnesium and lithium electrodes. *J. Power Sources* **2001**, *97-98*, 269–273.

[49] Aurbach, D.; Lu, Z.; Schechter, A.; Gofer, Y.; Gizbar, H.; Turgeman, R.; Cohen, Y.; Moshkovich, M.; Levi, E. Prototype systems for rechargeable magnesium batteries. *Nat.***2000**, *407*, 724–727.

[50] Mizrahi, O.; Amir, N.; Pollak, E.; Chusid, O.; Marks, V.; Gottlieb, H.; Larush, L.; Zinigrad, E.; Aurbach, D. Electrolyte Solutions with a Wide Electrochemical Window for Rechargeable Magnesium Batteries. *J. Electrochem. Soc.* **2007**, *155*, A103.

[51] Muldoon, J.; Bucur, C. B.; Oliver, A. G.; Zajicek, J.; Allred, G. D.; Boggess, W. C. Corrosion of magnesium electrolytes: chlorides – the culprit. *EES* **2013**, *6*, 482–487.

[52] Mohtadi, R.; Matsui, M.; Arthur, T. S.; Hwang, S.-J. Magnesium Borohydride: From Hydrogen Storage to Magnesium Battery. *Angew. Chem. Int. Ed.* **2012**, *51*, 9780–9783.

[53] Keyzer, E. N.; Glass, H. F. J.; Liu, Z.; Bayley, P. M.; Dutton, S. E.; Grey, C. P.; Wright, D. S. Mg(PF6)2-Based Electrolyte Systems: Understanding Electrolyte–Electrode Interactions for the Development of Mg-Ion Batteries. *J. Am. Chem. Soc.* **2016**, *138*, 8682–8685.

[54] Ha, S.-Y.; Lee, Y.-W.; Woo, S. W.; Koo, B.; Kim, J.-S.; Cho, J.; Lee, K. T.; Choi, N.-S. Magnesium(II) Bis(trifluoromethane sulfonyl) Imide-Based Electrolytes with Wide Electrochemical Windows for Rechargeable Magnesium Batteries. *ACS Appl. Mater. Interfaces* **2014**, *6*, 4063–4073.

[55] Ma, Z.; Kar, M.; Xiao, C.; Forsyth, M.; MacFarlane, D. R. Electrochemical cycling of Mg in Mg[TFSI]2/tetraglyme electrolytes. *Electrochem. Commun.* **2017**, *78*, 29–32.

[56] Baskin, A.; Prendergast, D. Exploration of the Detailed Conditions for Reductive Stability of Mg(TFSI)2 in Diglyme: Implications for Multivalent Electrolytes. *J. Phys. Chem. C* **2016**, *120*, 3583–3594.

[57] Jay, R.; Tomich, A. W.; Zhang, J.; Zhao, Y.; De Gorostiza, A.; Lavallo, V.; Guo, J. Comparative Study of Mg(CB11H12)2 and Mg(TFSI)2 at the Magnesium/Electrolyte Interface. *ACS Appl. Mater. Interfaces* **2019**, *11*, 11414–11420.

[58] G. McArthur, S.; Jay, R.; Geng, L.; Guo, J.; Lavallo, V. Below the 12-vertex: 10-vertex carborane anions as non-corrosive, halide free, electrolytes for rechargeable Mg batteries. *Chem. Commun.* **2017**, *53*, 4453–4456.

[59] Tutusaus, O.; Mohtadi, R.; Singh, N.; Arthur, T. S.; Mizuno, F. Study of Electrochemical Phenomena Observed at the Mg Metal/Electrolyte Interface. *ACS Energy Lett.* **2017**, *2*, 224–229.

[60] Hahn, N. T.; Seguin, T. J.; Lau, K.-C.; Liao, C.; Ingram, B. J.; Persson, K. A.; Zavadil, K. R. Enhanced Stability of the Carba- *closo* -dodecaborate Anion for High-Voltage Battery Electrolytes through Rational Design. *J. Am. Chem. Soc.* **2018**, *140*, 11076–11084.

[61] Zhao-Karger, Z.; Bardaji, M. E. G.; Fuhr, O.; Fichtner, M. A new class of non-corrosive, highly efficient electrolytes for rechargeable magnesium batteries. *J. Mater. Chem. A* **2017**, *5*, 10815–10820.

[62] Pavčnik, T.; Lozinšek, M.; Pirnat, K.; Vizintin, A.; Mandai, T.; Aurbach, D.; Dominko, R.; Bitenc, J. On the Practical Applications of the Magnesium Fluorinated Alkoxyaluminate Electrolyte in Mg Battery Cells. *ACS Appl. Mater. Interfaces* **2022**.

[63] Mandai, T. Critical Issues of Fluorinated Alkoxyborate-Based Electrolytes in Magnesium Battery Applications. *ACS Appl. Mater. Interfaces* **2020**, *12*, 39135–39144.

[64] Luo, J.; Bi, Y.; Zhang, L.; Zhang, X.; Liu, T. L. A Stable, Non-Corrosive Perfluorinated Pinacolatoborate Mg Electrolyte for Rechargeable Mg Batteries. *Angew. Chem. Int. Ed.* **2019**, *58*, 6967–6971.

[65] He, T.; Bruening, M. A.; Espinosa, M.; Agapie, T. Novel Silicate Platform as Weakly-Coordinating Anions for Diverse Organometallic and Electrochemical Applications. *Angew. Chem. Int. Ed.* **2025**, *64*, e2024171366.

[66] Jankowski, P.; Li, Z.; Zhao-Karger, Z.; Diemant, T.; Fichtner, M.; Vegge, T.; Lastra, J. M. G. Development of Magnesium Borate Electrolytes: Explaining the Success of Mg[B(hfip)4]2 Salt. *Energy Storage Mater.* **2022**, *45*, 1133–1143.

[67] Zhang, S.; Cheng, M.; Zhang, P.; Wang, Y.; Zhang, D.; Yang, Y.; Wang, J.; NuLi, Y. Insights into Stability of Magnesium Borate Salts for Rechargeable Magnesium Batteries from AIMD Simulations. *Chem. Commun.* **2022**.

[68] Carter, T. J.; Mohtadi, R.; Arthur, T. S.; Mizuno, F.; Zhang, R.; Shirai, S.; Kampf, J. W. Boron Clusters as Highly Stable Magnesium-Battery Electrolytes. *Angew. Chem. Int. Ed.* **2014**, *53*, 3173–3177.

[69] Kim, S. S.; See, K. A. Activating Magnesium Electrolytes through Chemical Generation of Free Chloride and Removal of Trace Water. *ACS Appl. Mater. Interfaces* **2021**, *13*, 671–680.

[70] Connell, J. G.; Genorio, B.; Lopes, P. P.; Strmcnik, D.; Stamenkovic, V. R.; Markovic, N. M. Tuning the Reversibility of Mg Anodes via Controlled Surface Passivation by H2O/Cl– in Organic Electrolytes. *Chem. Mater* **2016**, *28*, 8268–8277.

[71] Wang, F.; Hua, H.; Wu, D.; Li, J.; Xu, Y.; Nie, X.; Zhuang, Y.; Zeng, J.; Zhao, J. Solvent Molecule Design Enables Excellent Charge Transfer Kinetics for a Magnesium Metal Anode. *ACS Energy Lett.* **2022**, 780–789.

[72] Arroyo-de Dompablo, M. E.; Ponrouch, A.; Johansson, P.; Palacín, M. R. Achievements, Challenges, and Prospects of Calcium Batteries. *Chem. Rev* **2020**, *120*, 6331–6357.

[73] Ponrouch, A.; Frontera, C.; Bardé, F.; Palacín, M. R. Towards a calcium-based rechargeable battery. *Nat. Mater* **2016**, *15*, 169–172, 2.

[74] Araujo, R. B.; Thangavel, V.; Johansson, P. Towards novel calcium battery electrolytes by efficient computational screening. *Energy Storage Mater.* **2021**, *39*, 89–95.

[75] Yamijala, S. S. R. K. C.; Kwon, H.; Guo, J.; Wong, B. M. Stability of Calcium Ion Battery Electrolytes: Predictions from Ab Initio Molecular Dynamics Simulations. *ACS Appl. Mater. Interfaces* **2021**, *13*, 13114–13122.

[76] Li, Z.; Fuhr, O.; Fichtner, M.; Zhao-Karger, Z. Towards stable and efficient electrolytes for room-temperature rechargeable calcium batteries. *EES* **2019**, *12*, 3496–3501.

[77] Mandai, T.; Naya, H.; Masu, H. Comparative Studies on [B(HFIP)4]-Based Electrolytes with Mono- and Divalent Cations. *J. Phys. Chem. C* **2023**.

[78] Aurbach, D.; Schechter, A.; Moshkovich, M.; Cohen, Y. On the Mechanisms of Reversible Magnesium Deposition Processes. *J. Electrochem. Soc.* **2001**, *148*, A1004.

[79] Aurbach, D.; Gizbar, H.; Schechter, A.; Chusid, O.; Gottlieb, H. E.; Gofer, Y.; Goldberg, I. Electrolyte Solutions for Rechargeable Magnesium Batteries Based on Organomagnesium Chloroaluminate Complexes. *J. Electrochem. Soc.* **2001**, *149*, A115.

[80] Canepa, P.; Jayaraman, S.; Cheng, L.; Nidhi Rajput, N.; D. Richards, W.; Sai Gautam, G.; A. Curtiss, L.; A. Persson, K.; Ceder, G. Elucidating the structure of the magnesium aluminum chloride complex electrolyte for magnesium-ion batteries. *EES* **2015**, *8*, 3718–3730.

[81] Tutusaus, O.; Mohtadi, R.; Arthur, T. S.; Mizuno, F.; Nelson, E. G.; Sevryugina, Y. V. An Efficient Halogen-Free Electrolyte for Use in Rechargeable Magnesium Batteries. *Angew. Chem. Int. Ed.* **2015**, *54*, 7900–7904.

[82] Kisu, K.; Dorai, A.; Hatakeyama-Sato, K.; Takano, T.; Takagi, S.; Oyaizu, K.; Orimo, S.-i. Enhanced Durability of Ca Metal Battery with Dual Salt: Synergistic Effect on Solid Electrolyte Interphase and Solvation Structure for Improved Electrodeposition. *ACS Appl. Mater. Interfaces* **2024**.

[83] Palacín, M. R. Recent advances in rechargeable battery materials: a chemist's perspective. *Chem. Soc. Rev* **2009**, *38*, 2565–2575.

[84] Liang, Y.; Zhao, C.-Z.; Yuan, H.; Chen, Y.; Zhang, W.; Huang, J.-Q.; Yu, D.; Liu, Y.; Titirici, M.-M.; Chueh, Y.-L.; Yu, H.; Zhang, Q. A review of rechargeable batteries for portable electronic devices. *InfoMat* **2019**, *1*, 6–32.

[85] Zeng, A.; Chen, W.; Rasmussen, K. D.; Zhu, X.; Lundhaug, M.; Müller, D. B.; Tan, J.; Keiding, J. K.; Liu, L.; Dai, T.; Wang, A.; Liu, G. Battery technology and recycling alone will not save the electric mobility transition from future cobalt shortages. *Nat. Commun* **2022**, *13*, 1341, 1.

[86] Turcheniuk, K.; Bondarev, D.; Amatucci, G. G.; Yushin, G. Battery materials for low-cost electric transportation. *Mater. Today* **2021**, *42*, 57–72.

[87] Lu, Z.; Schechter, A.; Moshkovich, M.; Aurbach, D. On the electrochemical behavior of magnesium electrodes in polar aprotic electrolyte solutions. *J. Electroanal. Chem.* **1999**, *466*, 203–217.

[88] Zhang, J.; Liu, J.; Wang, M.; Zhang, Z.; Zhou, Z.; Chen, X.; Du, A.; Dong, S.; Li, Z.; Li, G.; Cui, G. The origin of anode–electrolyte interfacial passivation in rechargeable Mg-metal batteries. *EES* **2023**, *16*, 1111–1124.

[89] Mandai, T.; Watanabe, M. Oxygen – a fatal impurity for reversible magnesium deposition/dissolution. *J. Mater. Chem. A* **2023**.

[90] Attias, R.; Salama, M.; Hirsch, B.; Goffer, Y.; Aurbach, D. Anode-Electrolyte Interfaces in Secondary Magnesium Batteries. *Joule* **2019**, *3*, 27–52.

[91] Arthur, T. S.; Singh, N.; Matsui, M. Electrodeposited Bi, Sb and Bi1-xSbx alloys as anodes for Mg-ion batteries. *Electrochem. Commun.* **2012**, *16*, 103–106.

[92] Periyapperuma, K.; Tran, T. T.; Purcell, M. I.; Obrovac, M. N. The Reversible Magnesiation of Pb. *Electrochim. Acta* **2015**, *165*, 162–165.

[93] Singh, N.; Arthur, T. S.; Ling, C.; Matsui, M.; Mizuno, F. A high energy-density tin anode for rechargeable magnesium-ion batteries. *Chem. Commun.* **2012**, *49*, 149–151.

[94] Nguyen, D.-T.; Song, S.-W. Magnesium stannide as a high-capacity anode for magnesium-ion batteries. *J. Power Sources* **2017**, *368*, 11–17.

[95] Murgia, F.; Weldekidan, E. T.; Stievano, L.; Monconduit, L.; Berthelot, R. First investigation of indium-based electrode in Mg battery. *Electrochem. Commun.* **2015**, *60*, 56–59.

[96] Niu, J.; Zhang, Z.; Aurbach, D. Alloy Anode Materials for Rechargeable Mg Ion Batteries. *Adv. Energy Mater* **2020**, *10*, 2000697.

[97] Südholz, A. D.; Kirkland, N. T.; Buchheit, R. G.; Birbilis, N. Electrochemical Properties of Intermetallic Phases and Common Impurity Elements in Magnesium Alloys. *Electrochem. Solid-State Lett.* **2011**, *14*, C5.

[98] Ma, J.; Zhang, Y.; Ma, M.; Qin, C.; Ren, F.; Wang, G. Corrosion and discharge performance of a magnesium aluminum eutectic alloy as anode for magnesium–air batteries. *Corros. Sci.* **2020**, *170*, 108695.

[99] Xu, S.; Ikpi, M. E.; Dong, J.; Wei, J.; Ke, W.; Chen, N. Effects of Cadmium alloying on the Corrosion and Mechanical Properties of Magnesium. *Int. J. Electrochem. Sci.* **2012**, *7*.

[100] Iwamura, S.; Nishihara, H.; Ono, Y.; Morito, H.; Yamane, H.; Nara, H.; Osaka, T.; Kyotani, T. Li-Rich Li-Si Alloy As A Lithium-Containing Negative Electrode Material Towards High Energy Lithium-Ion Batteries. *Sci. Rep.* **2015**, *5*, 8085.

[101] Sun, J.; Zeng, Q. R.; Lv, R.; Lv, W.; Yang, Q.-H.; Amal, R.; Wang, D.-W. A Li-ion sulfur full cell with ambient resistant Al-Li alloy anode. *Energy Storage Mater.* **2018**, *15*, 209–217.

[102] Tong, X.; Zhang, F.; Ji, B.; Sheng, M.; Tang, Y. Carbon-Coated Porous Aluminum Foil Anode for High-Rate, Long-Term Cycling Stability, and High Energy Density Dual-Ion Batteries. *Adv. Mater* **2016**, *28*, 9979–9985.

[103] Guo, W.; Wang, Y.; Zhang, F.; Rao, S.; Mao, P.; Wang, D. SnO2@C@Fe3O4 Sandwich-like Hollow Nanospheres for High-Performance Lithium-Ion Battery Anodes. *Energ. Fuel* **2020**, *34*, 2462–2470.

[104] Wan, M.; Kang, S.; Wang, L.; Lee, H.-W.; Zheng, G. W.; Cui, Y.; Sun, Y. Mechanical rolling formation of interpenetrated lithium metal/lithium tin alloy foil for ultrahigh-rate battery anode. *Nat. Commun* **2020**, *11*, 829.

[105] Meng, H.;Kravchyk, K; Walter, M; Kovalenko, M. Monodisperse Antimony Nanocrystals for High-Rate Li-ion and Na-ion Battery Anodes: Nano versus Bulk Nano Letters. **2014**, *14*, 3, 1255–1262.

[106] Sun, C.-F.; Hu, J.; Wang, P.; Cheng, X.-Y.; Lee, S. B.; Wang, Y. Li3PO4 Matrix Enables a Long Cycle Life and High Energy Efficiency Bismuth-Based Battery. *Nano Lett.* **2016**, *16*, 5875–5882,.

[107] Chi, S.-S.; Wang, Q.; Han, B.; Luo, C.; Jiang, Y.; Wang, J.; Wang, C.; Yu, Y.; Deng, Y. Lithiophilic Zn Sites in Porous CuZn Alloy Induced Uniform Li Nucleation and Dendrite-free Li Metal Deposition. *Nano Lett.* **2020**, *20*, 2724–2732.

[108] Wang, J.; King, P.; Huggins, R. A. Investigations of binary lithium-zinc, lithium-cadmium and lithium-lead alloys as negative electrodes in organic solvent-based electrolyte. *Solid State Ion* **1986**, *20*, 185–189.

[109] Kim, S.-O.; Manthiram, A. High-Performance Zn–TiC–C Nanocomposite Alloy Anode with Exceptional Cycle Life for Lithium-Ion Batteries. *ACS Appl. Mater. Interfaces* **2015**, *7*, 14801–14807.

[110] Peng, M.; Shin, K.; Jiang, L.; Jin, Y.; Zeng, K.; Zhou, X.; Tang, Y. Alloy-Type Anodes for High-Performance Rechargeable Batteries. *Angew. Chem. Int. Ed.* **2022**, *61*, e202206770.

[111] Obrovac, M. N.; Chevrier, V. L. Alloy Negative Electrodes for Li-Ion Batteries. *Chem. Rev* **2014**, *114*, 11444–11502.

[112] Song, K.; Liu, C.; Mi, L.; Chou, S.; Chen, W.; Shen, C. Recent Progress on the Alloy-Based Anode for Sodium-Ion Batteries and Potassium-Ion Batteries. *Small* **2021**, *17*, 1903194.

[113] Kulish, V. V.; Malyi, O. I.; Ng, M.-F.; Chen, Z.; Manzhos, S.; Wu, P. Controlling Na diffusion by rational design of Si-based layered architectures. *Phys. Chem. Chem. Phys.* **2014**, *16*, 4260–4267.

[114] Jangid, M. K.; Vemulapally, A.; Sonia, F. J.; Aslam, M.; Mukhopadhyay, A. Feasibility of Reversible Electrochemical Na-Storage and Cyclic Stability of Amorphous Silicon and Silicon-Graphene Film Electrodes. *J. Electrochem. Soc.* **2017**, *164*, A2559.

[115] Wang, Q.; Zhao, X.; Ni, C.; Tian, H.; Li, J.; Zhang, Z.; Mao, S. X.; Wang, J.; Xu, Y. Reaction and Capacity-Fading Mechanisms of Tin Nanoparticles in Potassium-Ion Batteries. *J. Phys. Chem. C* **2017**, *121*, 12652–12657.

[116] Komaba, S.; Matsuura, Y.; Ishikawa, T.; Yabuuchi, N.; Murata, W.; Kuze, S. Redox reaction of Sn-polyacrylate electrodes in aprotic Na cell. *Electrochem. Commun.* **2012**, *21*, 65–68.

[117] Yue, C.; Yu, Y.; Sun, S.; He, X.; Chen, B.; Lin, W.; Xu, B.; Zheng, M.; Wu, S.; Li, J.; Kang, J.; Lin, L. High Performance 3D Si/Ge Nanorods Array Anode Buffered by TiN/Ti Interlayer for Sodium-Ion Batteries. *Adv. Funct. Mater.* **2015**, *25*, 1386–1392.

[118] Sun, J.; Lee, H.-W.; Pasta, M.; Sun, Y.; Liu, W.; Li, Y.; Lee, H. R.; Liu, N.; Cui, Y. Carbothermic reduction synthesis of red phosphorus-filled 3D carbon material as a high-capacity anode for sodium ion batteries. *Energy Storage Mater.* **2016**, *4*, 130–136.

[119] Su, D.; Dou, S.; Wang, G. Bismuth: A new anode for the Na-ion battery. *Nano Energy* **2015**, *12*, 88–95.

[120] Cheng, X.; Li, D.; Wu, Y.; Xu, R.; Yu, Y. Bismuth nanospheres embedded in three-dimensional (3D) porous graphene frameworks as high performance anodes for sodium- and potassium-ion batteries. *J. Mater. Chem. A* **2019**, *7*, 4913–4921.

[121] Qian, J.; Chen, Y.; Wu, L.; Cao, Y.; Ai, X.; Yang, H. High capacity Na-storage and superior cyclability of nanocomposite Sb/C anode for Na-ion batteries. *Chem. Commun.* **2012**, *48*, 7070–7072.

[122] Chevrier, V. L.; Ceder, G. Challenges for Na-ion Negative Electrodes. *J. Electrochem. Soc.* **2011**, *158*, A1011.

[123] Wang, M.; Jiang, C.; Zhang, S.; Song, X.; Tang, Y.; Cheng, H.-M. Reversible calcium alloying enables a practical room-temperature rechargeable calcium-ion battery with a high discharge voltage. *Nat. Chem* **2018**, *10*, 667–672.

[124] Yao, Z.; Hegde, V. I.; Aspuru-Guzik, A.; Wolverton, C. Discovery of Calcium-Metal Alloy Anodes for Reversible Ca-Ion Batteries. *Adv. Energy Mater* **2019**, *9*, 1802994.

[125] Jin, W.; Li, Z.; Wang, Z.; Fu, Y. Q. Mg ion dynamics in anode materials of Sn and Bi for Mg-ion batteries. *Mater. Chem. Phys.* **2016**, *182*, 167–172.

[126] Benmayza, A.; Ramanathan, M.; Singh, N.; Mizuno, F.; Prakash, J. Electrochemical and Thermal Studies of Bismuth Electrodes for Magnesium-Ion Cells. *J. Electrochem. Soc.* **2015**, *162*, A1630.

[127] Shao, Y.; Gu, M.; Li, X.; Nie, Z.; Zuo, P.; Li, G.; Liu, T.; Xiao, J.; Cheng, Y.; Wang, C.; Zhang, J.-G.; Liu, J. Highly Reversible Mg Insertion in Nanostructured Bi for Mg Ion Batteries. *Nano Lett.* **2014**, *14*, 255–260.

[128] Wang, M.; Yuwono, J. A.; Vasudevan, V.; Birbilis, N.; Medhekar, N. V. Atomistic Mechanisms of Mg Insertion Reactions in Group XIV Anodes for Mg-Ion Batteries. *ACS Appl. Mater. Interfaces* **2019**, *11*, 774–783.

[129] Zheng, X.; Song, C.; Yuan, Y.; Li, D.; Gu, D.; Wu, L.; Huang, G.; Wang, J.; Pan, F. High stability In–Sn–Bi multi-element alloy anode for Mg ion batteries. *J. Power Sources* **2023**, *575*, 233141.

[130] Gu, D.; Yuan, Y.; Liu, J.; Li, D.; Zhang, W.; Wu, L.; Cao, F.; Wang, J.; Huang, G.; Pan, F. The electrochemical properties of bismuth-antimony-tin alloy anodes for magnesium ion batteries. *J. Power Sources* **2022**, *548*, 232076.

[131] Cheng, Y.; Shao, Y.; Parent, L. R.; Sushko, M. L.; Li, G.; Sushko, P. V.; Browning, N. D.; Wang, C.; Liu, J. Interface Promoted Reversible Mg Insertion in Nanostructured Tin–Antimony Alloys. *Adv. Mater* **2015**, *27*, 6598–6605.

[132] Kitada, A.; Kang, Y.; Uchimoto, Y.; Murase, K. Electrochemical Reactivity of Magnesium Ions with Sn-Based Binary Alloys (Cu-Sn, Pb-Sn, and In-Sn). *ECS Trans.* **2014**, *58*, 75.

[133] Parent, L. R.; Cheng, Y.; Sushko, P. V.; Shao, Y.; Liu, J.; Wang, C.-M.; Browning, N. D. Realizing the Full Potential of Insertion Anodes for Mg-Ion Batteries Through the Nanostructuring of Sn. *Nano Lett.* **2015**, *15*, 1177–1182.

[134] Song, M.; Zhang, T.; Niu, J.; Gao, H.; Shi, Y.; Zhang, Y.; Ma, W.; Zhang, Z. Boosting electrochemical reactivity of tin as an anode for Mg ion batteries through introduction of second phase. *J. Power Sources* **2020**, *451*, 227735.

[135] Tran, T. T.; Obrovac, M. N. Alloy Negative Electrodes for High Energy Density Metal-Ion Cells. *J. Electrochem. Soc.* **2011**, *158*, A1411.

[136] Südholz, A. D.; Kirkland, N. T.; Buchheit, R. G.; Birbilis, N. Electrochemical Properties of Intermetallic Phases and Common Impurity Elements in Magnesium Alloys. *ESL* **2010**, *14*, C5.

[137] Department of Materials Science and Engineering, Yantai Nanshan University, Yantai 265713,China; Zhu, H. Electrochemical performance of Mg-Al-Zn and Mg-Al-Zn-Ce alloys as anodes for Mg-air battery. *Int. J. Electrochem. Sci.* **2018**, 11180–11192.

[138] Litvintsev, A. I.; Arbuzova, L. A. Kinetics of degassing of aluminum powders. *Soviet Powder Metallurgy and Metal Ceramics* **1967**, *6*, 1–10.

[139] Suryanarayana, C. Mechanical Alloying: A Novel Technique to Synthesize Advanced Materials. *Res.* **2019**, *2019*.

[140] Paliwal, M.; Jung, I.-H. Thermodynamic modeling of the Al–Bi, Al–Sb, Mg–Al–Bi and Mg–Al–Sb systems. *Calphad* **2010**, *34*, 51–63.

[141] Uenishi, K.; Yong, K. H.; Kobayashi, K. F. Mechanical alloying in the Al-Bi alloy system. *J. Mater. Sci.* **1996**, *31*, 3605–3611.

[142] Blondeau, L.; Foy, E.; Khodja, H.; Gauthier, M. Unexpected Behavior of the InSb Alloy in Mg-Ion Batteries: Unlocking the Reversibility of Sb. *J. Phys. Chem. C* **2019**, *123*, 1120–1126.

[143] Murgia, F.; Laurencin, D.; Weldekidan, E. T.; Stievano, L.; Monconduit, L.; Doublet, M.-L.; Berthelot, R. Electrochemical Mg alloying properties along the Sb1-xBix solid solution. *Electrochim. Acta* **2018**, *259*, 276–283.

[144] Benjamin, J. S.; Volin, T. E. The mechanism of mechanical alloying. *Metall. Mater. Trans.* **1974**, *5*, 1929–1934.

[145] Demétrio, K. B. Cryomilling And Spark Plasma Sintering of Aluminum Alloy. **2024**

[146] Nagesha, K. V. A Review On Mechanical Alloying. *Int. J. Eng. Res.* **2013**, *3*.

[147] Delogu, F.; Mulas, G.; Schiffini, L.; Cocco, G. Mechanical work and conversion degree in mechanically induced processes. *Mater. Sci. Eng. A* **2004**, *382*, 280–287.

[148] Wohlmuth, D.; Epp, V.; Bottke, P.; Hanzu, I.; Bitschnau, B.; Letofsky-Papst, I.; Kriechbaum, M.; Amenitsch, H.; Hofer, F.; Wilkening, M. Order vs. disorder—a huge increase in ionic conductivity of nanocrystalline LiAlO 2 embedded in an amorphous-like matrix of lithium aluminate. *J. Mater. Chem. A* **2014**, *2*, 20295–20306.

[149] Wilkening, M.; Epp, V.; Feldhoff, A.; Heitjans, P. Tuning the Li Diffusivity of Poor Ionic Conductors by Mechanical Treatment: High Li Conductivity of Strongly Defective LiTaO3 Nanoparticles. *J. Phys. Chem. C* **2008**, *112*, 9291–9300.

[150] Blondeau, L.; Surblé, S.; Foy, E.; Khodja, H.; Gauthier, M. Electrochemical reactivity of In-Pb solid solution as a negative electrode for rechargeable Mg-ion batteries. *J. Energy Chem.* **2021**, *55*, 124–128.

[151] Baggetto, L.; Hah, H.-Y.; Jumas, J.-C.; Johnson, C. E.; Johnson, J. A.; Keum, J. K.; Bridges, C. A.; Veith, G. M. The reaction mechanism of SnSb and Sb thin film anodes for Na-ion batteries studied by X-ray diffraction, 119Sn and 121Sb Mössbauer spectroscopies. *J. Power Sources* **2014**, *267*, 329–336.

[152] Glaser, C.; Wei, Z.; Indris, S.; Klement, P.; Chatterjee, S.; Ehrenberg, H.; Zhao-Karger, Z.; Rohnke, M.; Janek, J. To Be or Not to Be – Is MgSc2Se4 a Mg-Ion Solid Electrolyte? *Adv. Energy Mater.* **2023**, *13*, 2301980.

[153] Liu, Z.; Liu, J.; Zhao, S.; Xun, S.; Byaruhanga, P.; Chen, S.; Tang, Y.; Zhu, T.; Chen, H. Low-cost iron trichloride cathode for all-solid-state lithium-ion batteries. *Nat. Sustain.* **2024**, *7*, 1492–1500.

Appendix A

SUPPLEMENTARY INFORMATION FOR INVESTIGATING CAPACITY FADE MECHANISMS IN MG-MCL$_x$ BATTERIES

Appendix A contains supplementary information for Chapter 2: Investigating capacity fade mechanisms in Mg-MCl$_x$ batteries. Included in this appendix are a cell schematic, cyclic voltammetry of MCl$_x$ active materials, partial galvanostatic cycling with electrode replacement, ex situ XRD characterizations, GITT of various active materials, and chronopotentiometry of Mg|Mg symmetric cells with electrolyte saturated with dissolved active material.

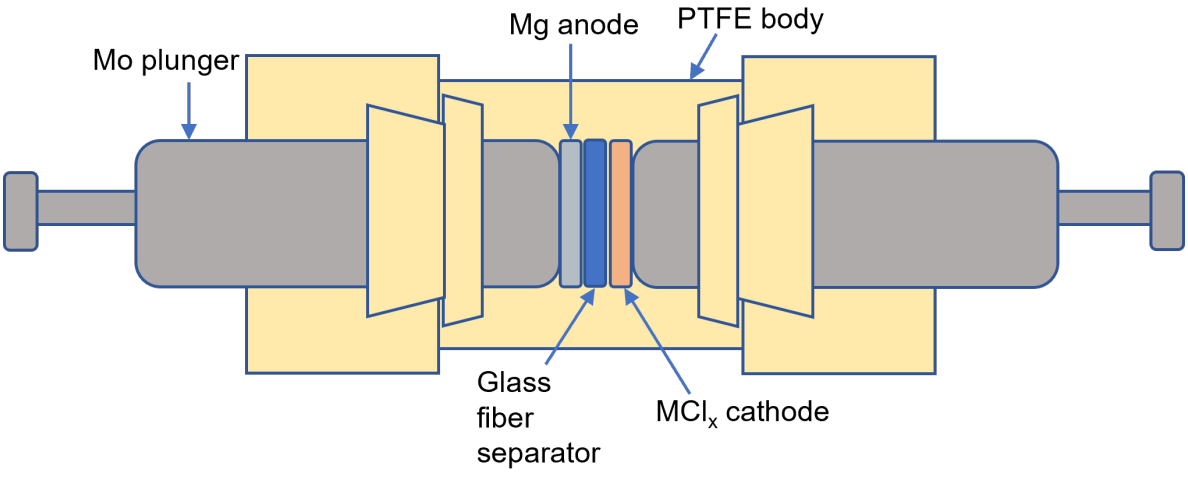

Figure A.1: Cell schematic featuring Mo current collectors, PTFE body components, a Mg anode, GFD separator, and a MClx cathode.

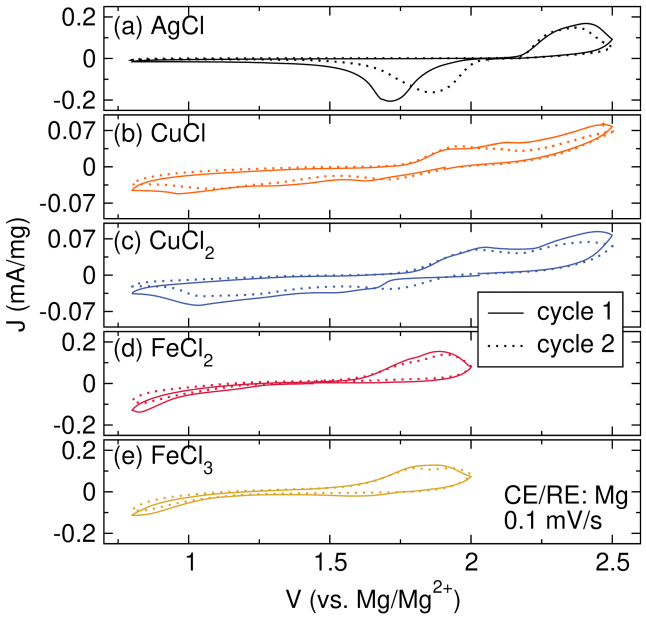

Figure A.2: First and second cyclic voltammagrams of (a) AgCl, (b) CuCl, (c) $CuCl_2$, (d) $FeCl_2$, and (d) $FeCl_3$ with a Mg counter/reference electrode and the APC electrolyte.

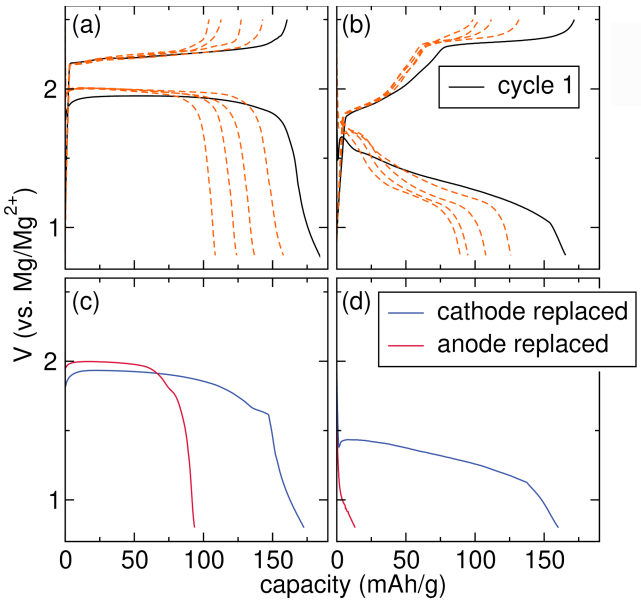

Figure A.3: First five galvanostatic cycles at 0.12C for an (a) AgCl cathode and a (b) $CuCl_2$ cathode. Cells were disassembled after five cycles, and one electrode was replaced. Subsequent discharge curves are shown for (c) AgCl and (d) $CuCl_2$.

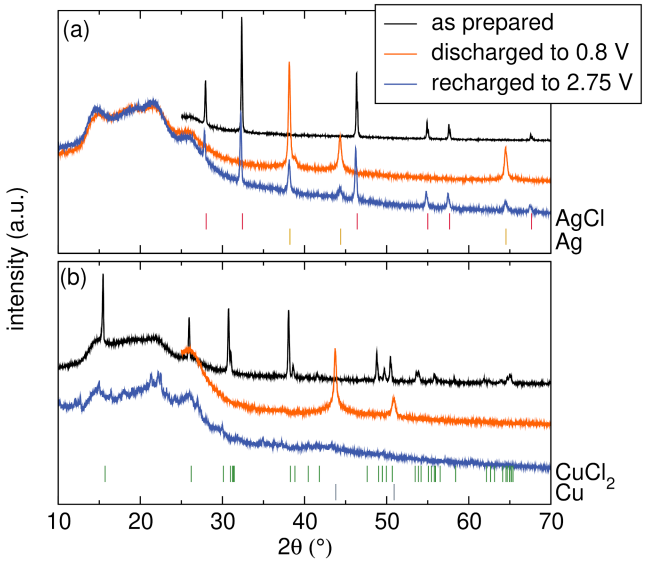

Figure A.4: Ex situ pXRD patterns of (a) AgCl and (b) $CuCl_2$ cathodes at various states of charge.

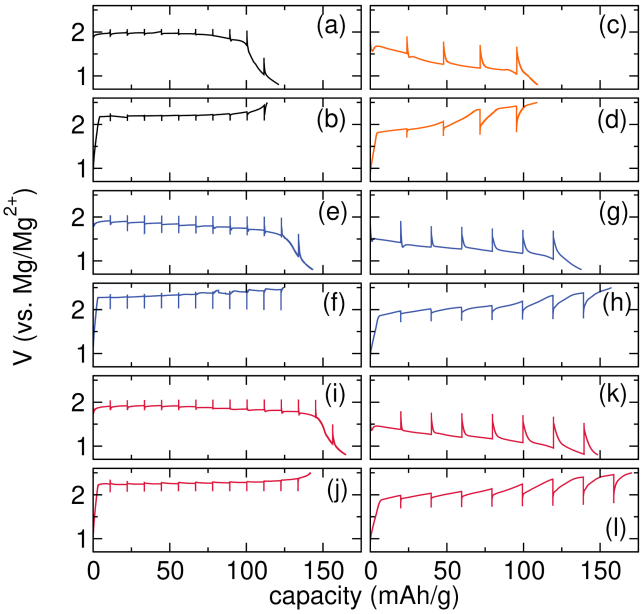

Figure A.5: GITT curves at 0.12C of (left) AgCl and (right) $CuCl_2$ cathodes with various processing techniques: (a) and (b) AgCl synthesized in the presence of C; (c) and (d) $CuCl_2$ processed in a planetary mill; (e) and (f) AgCl and (g) and (h) $CuCl_2$ processed in a high energy ball mill; and (i) and (j) AgCl and (k) and (l) $CuCl_2$ ground by hand.

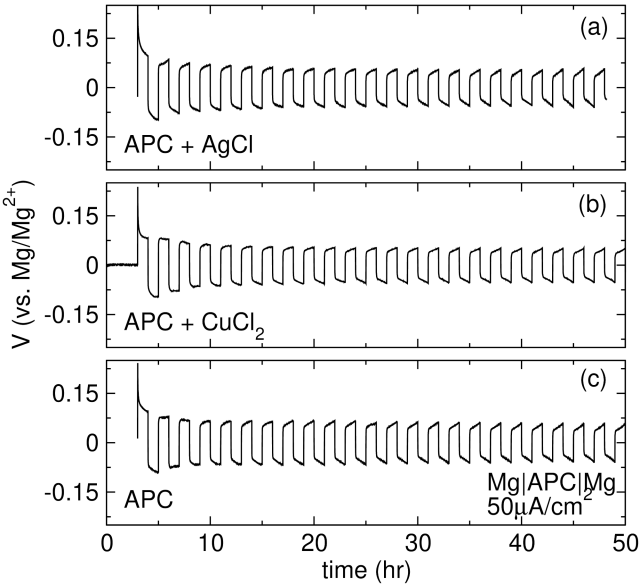

Figure A.6: Chronopotentiometry traces of Mg|Mg symmetric cells with the APC electrolyte. The Mg foils have been soaked for 7 days in (a) APC + saturated AgCl, (b) APC + saturated $CuCl_2$, and (c) APC.

Appendix B

SUPPLEMENTARY INFORMATION FOR ELECTROCHEMICAL AND ANALYTICAL CHARACTERIZATION OF A HIGHLY STABLE, HALIDE FREE MG ELECTROLYTE BASED ON WEAKLY COORDINATING SILICATE ANIONS

Appendix B contains supplementary information for Chapter 3: Electrochemical and analytical characterization of a highly stable, halide free Mg electrolyte based on weakly coordinating silicate anions. It includes cyclic volammetry of 0.25 M $Mg[^{Me}Si^{F}_{24}]_2$ with various additive concentrations, Coulombic efficiency as a function of cycle index for the same, Chronopotentiometry of Mg|Mg symmetric cells at various current densities, SEM micrographs of deposited Mg from 0.25 M $Mg[^{Me}Si^{F}_{24}]_2$, Coulombic efficiencies as a function of cycle index for 0.25 M $Mg[^{Me}Si^{F}_{24}]_2$ with a 3MPA cosolvent, cyclic voltammetry of a structural variant featuring a Ph axial ligand, structures of electrolyte variants, voltammetry showing the effect of working electrode reuse, SEM/EDS of a used and cleaned Pt working electrode, voltammetry with increasing additive levels to achieve reproducible electrochemical results, and finally voltammetry comparing results in different glovebox atmospheres.

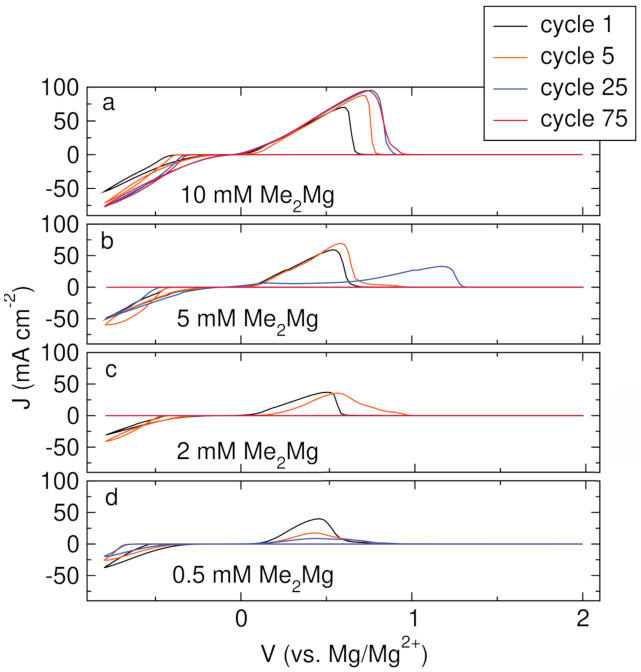

Figure B.1: Selected cyclic voltammograms of 0.25 M $Mg[^{Me}Si^{F}{}_{24}]_2$ electrolyte with (a) 10 mM, (b) 5 mM, (c) 2 mM, and (d) 0.5 mM Me_2Mg additive. WE: Pt, CE: Mg, RE: Mg, 25 mV/s.

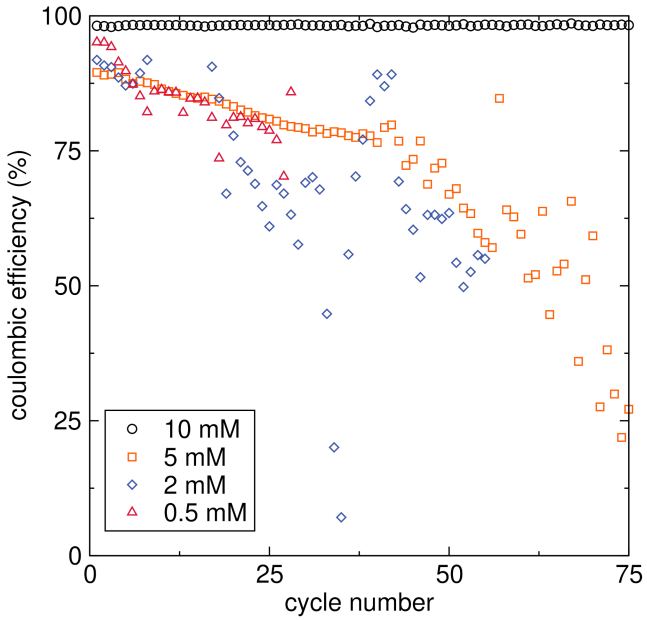

Figure B.2: Coulombic efficiency as a function of cycle number for the cyclic voltammograms illustrated in S1.

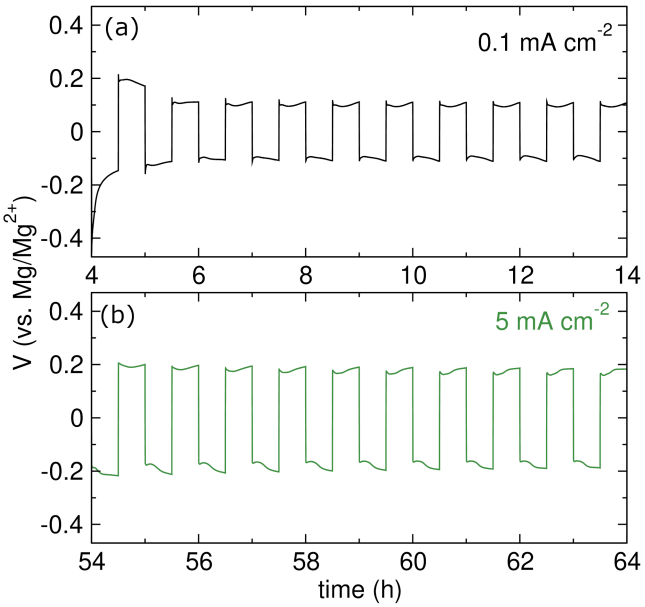

Figure B.3: Chronopotentiometry traces of symmetric Mg|0.25 M $Mg[^{Me}Si^{F}{}_{24}]_2$ + 10 mM Me_2Mg|Mg at (a) 0.1 mA cm^{-2} and (b) 5 mA cm^{-2}.

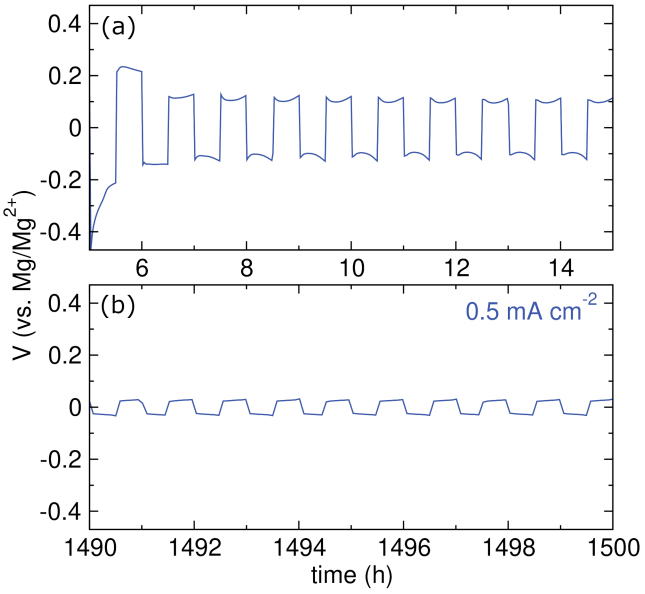

Figure B.4: Chronopotentiometry traces of symmetric Mg|0.25 M $Mg[^{Me}Si^{F}{}_{24}]_2$ + 20 mM Bu_2Mg|Mg during hours (a) 5 - 15 and (b) 1490 - 1500.

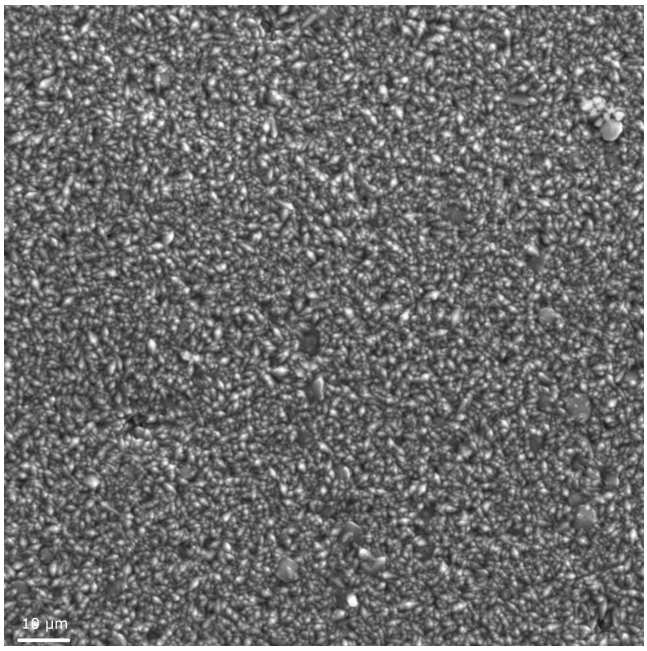

Figure B.5: SEM micrograph of deposition at -0.5 mA cm^{-2} from 0.25 M $Mg[^{Me}Si^{F}_{24}]_2$ + 20 mM Bu_2Mg for 5 hours on Pt.

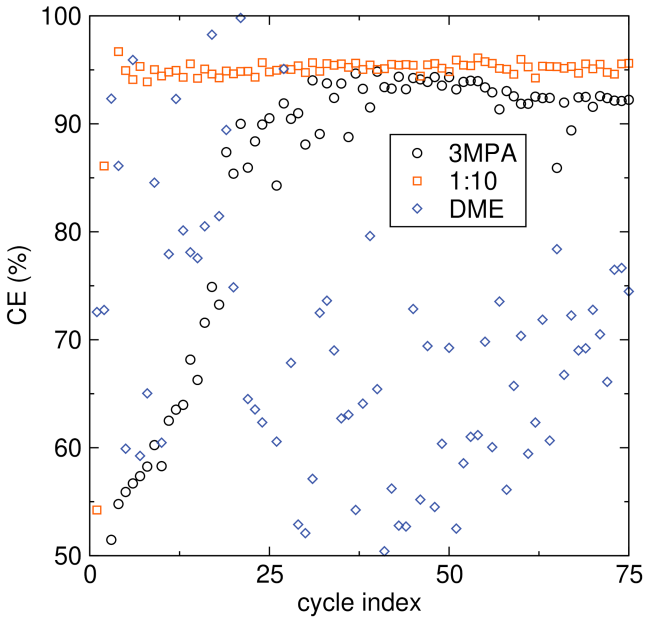

Figure B.6: Coulombic efficiency as a function of cycle index for 0.25 M $Mg[^{Me}Si^{F}_{24}]_2$ dissolved in 3MPA, DME, and DME:3MPA 1:10 vol:vol.

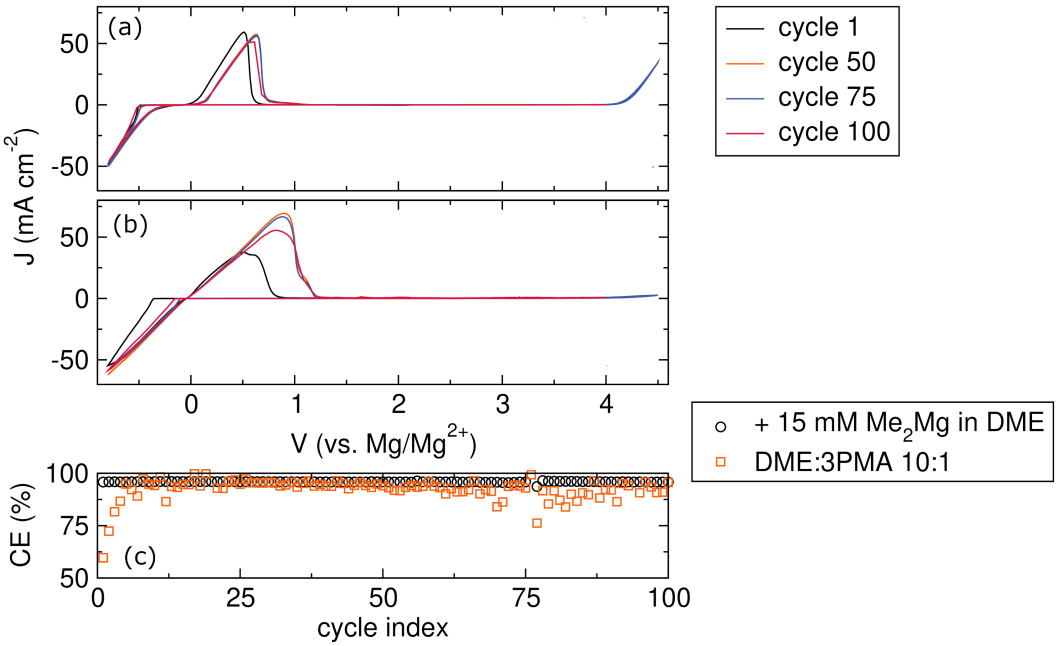

Figure B.7: Selected cyclic voltammograms of 0.25 M Mg[^{Ph}Si$^{F}_{24}$]$_2$ dissolved in DME + 15 mM Me_2Mg (a), in DME:3MPA 1:10 (b), and (c) their corresponding Coulombic efficiencies.

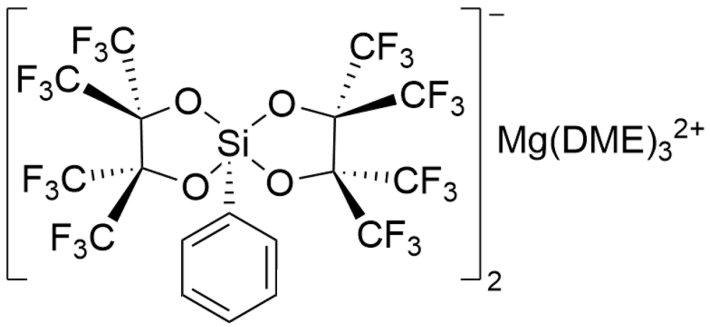

Figure B.8: Structure of Mg[^{Ph}Si$^{F}_{24}$]$_2$

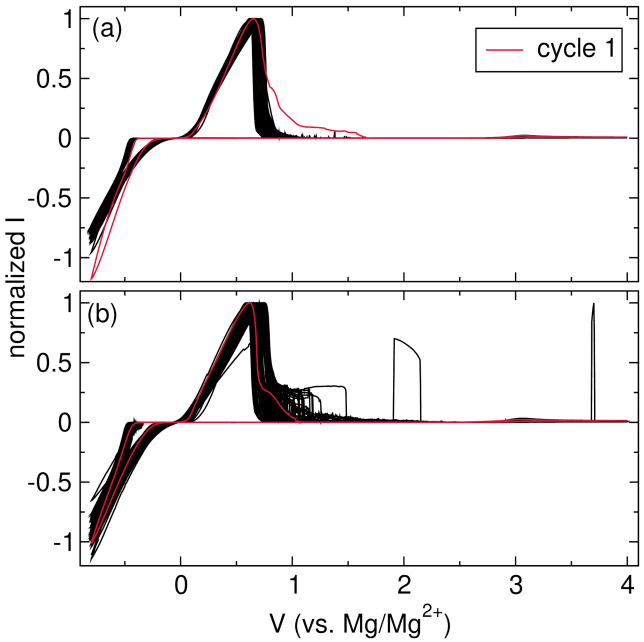

Figure B.9: Cyclic voltammograms of 0.25 M $Mg[^{Me}Si^{F}_{24}]_2$ dissolved in DME + 10 mM Me_2Mg on a (a) new Pt working electrode and a (b) used Pt working electrode.

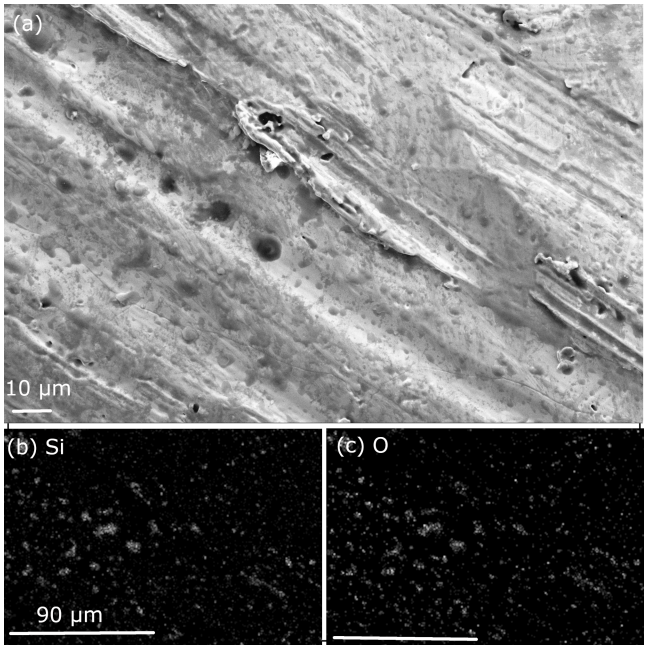

Figure B.10: (a) SEM micrograph of a used Pt working electrode post treatment with nitric acid and H_2 flame and corresponding EDS maps for (b) Si and (c) O.

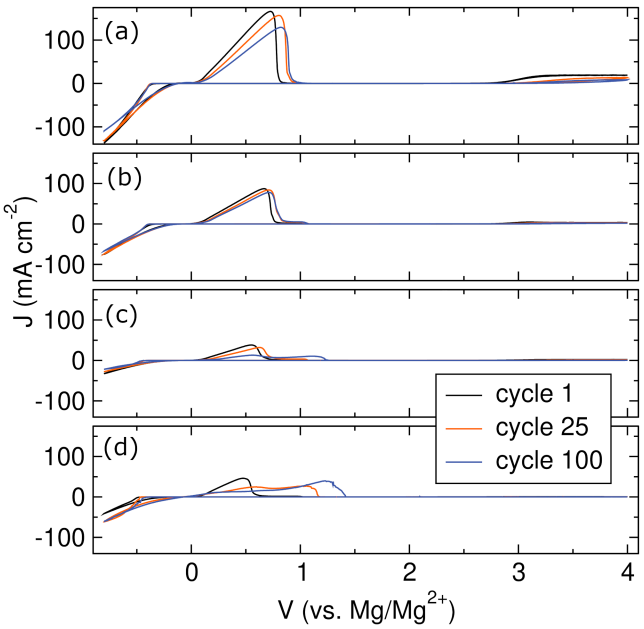

Figure B.11: Selected cyclic voltammograms of 0.25 M $Mg[^{Me}Si^{F}{}_{24}]_2$ dissolved in DME with variable concentrations of Me_2Mg: (a) 15 mM, (b) 25 mM, (c) 50 mM, (d) 100 mM. WE: Pt, CE: Mg, RE: Mg. 25 mV s^{-1}.

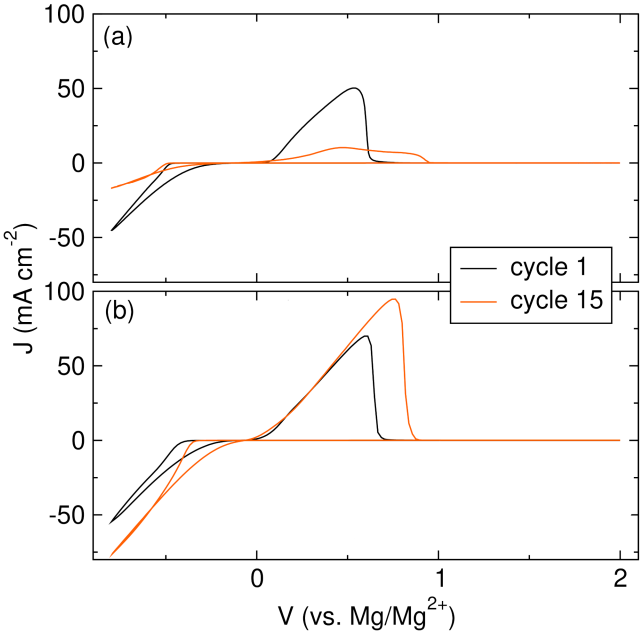

Figure B.12: Selected cyclic voltammograms of 0.25 M $Mg[^{Me}Si^{F}{}_{24}]_2$ dissolved in DME + 10 mM Me_2Mg in (a) a "standard" battery lab glovebox purged for 45 minutes and (b) a vacant glovebox purged for 15 minutes. WE: Pt, CE: Mg, RE: Mg. 25 mV s^{-1}.

Appendix C

SUPPLEMENTARY INFORMATION FOR ELECTROCHEMICAL AND ANALYTICAL CHARACTERIZATION OF A MG ELECTROLYTE

Appendix C contains supplementary information for Chapter 4: Electrochemical and analytical characterization of a Mg electrolyte. It includes Coulombic efficiency as function of cycle number for various electrolyte concentrations for WCA-1 in DME, an EDS sum spectrum for Mg deposits from WCA-1, Coulombic efficiency as a function of cycle number for WCA-2 in DME, and an EDS sum spectrum for Mg deposits from WCA-2.

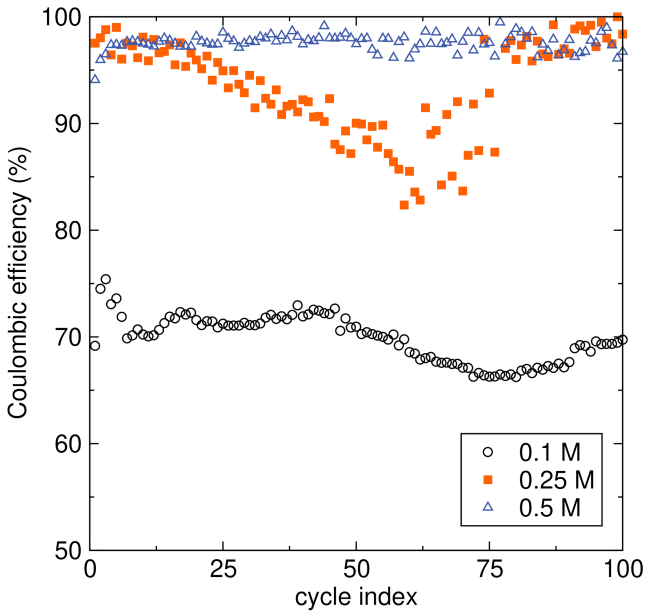

Figure C.1: Coulombic efficiency as a function of cycle number for the cyclic voltammograms shown in Figure 4.1.

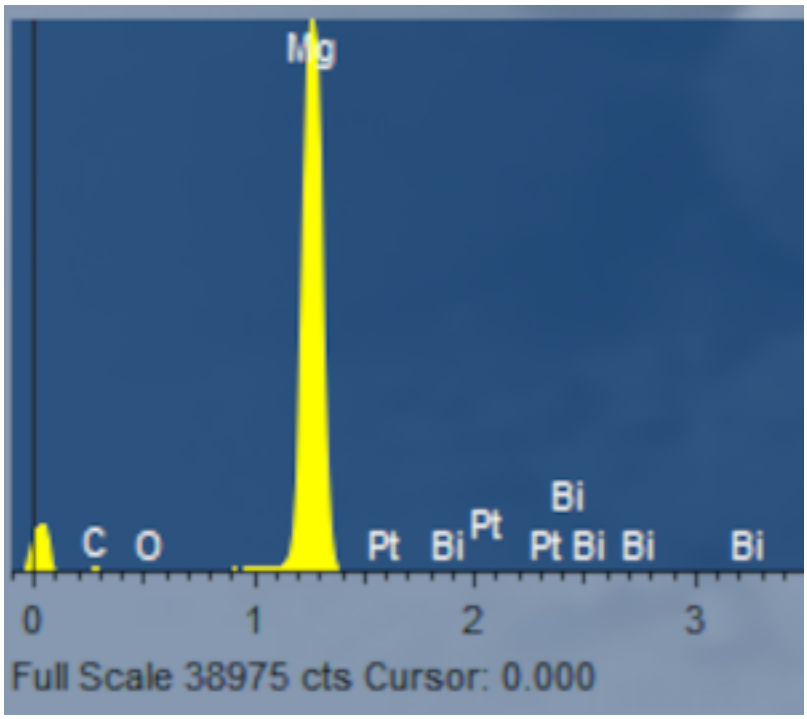

Figure C.2: EDS sum spectrum for the deposition shown in Figure 4.3.

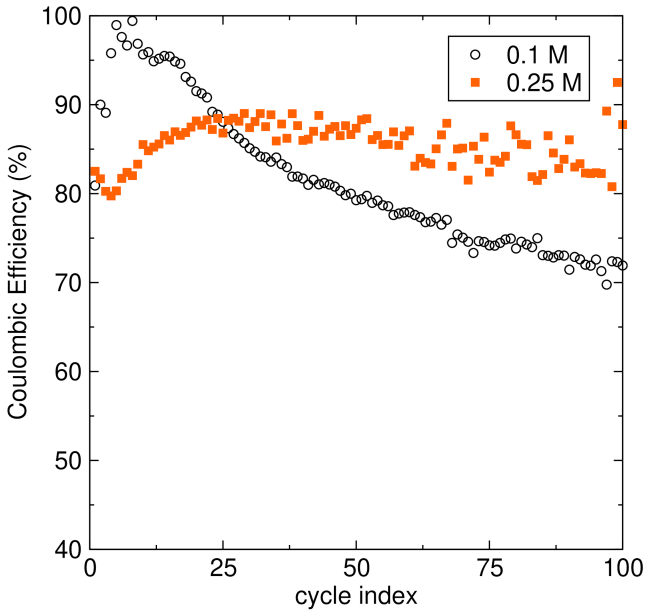

Figure C.3: Coulombic efficiency as a function of cycle number for the cyclic voltammograms shown in Figure 4.5.

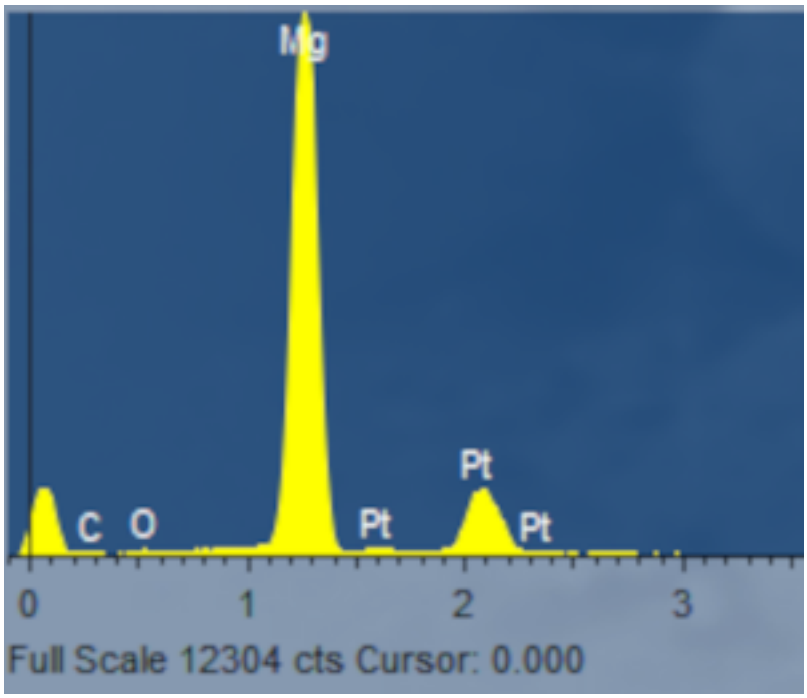

Figure C.4: EDS sum spectrum for the deposition shown in Figure 4.6.

Appendix D

SUPPLEMENTARY INFORMATION FOR REALIZING AL AS A WATER-RESISTANT MG HOST FOR ENERGY STORAGE

Appendix D presents supplementary information for Chapter 5: Realizing Al as a water-resistant Mg host for energy storage. It includes lattice parameters calculated from Rietveld refinements of alloy phases; cyclic voltammetry of an Al powder composite electrode; EDS sum spectra of the ABX alloy series; SEM/EDS maps of ABX alloys; fitted XRD patterns for certain ABX alloys; normalized CV curves for the ABX alloy series; full cycling data for the ABX alloy series, cyclic voltammetry of AB40 with a modified cycling protocol; SEM micrographs showing AB40 composite electrodes after cycling; SEM micrographs of certain ABX alloys compared to the starting materials; XRD and CV data of milled Al60Sn40; EDS spectra of sites from a reduced AB40 electrode; galvanostatic reduction curves and corresponding XRD patterns of AB40 and Bi; EIS spectra for AB40, Mg, and Pt with and without added H_2O; and finally Tafel plots for the same electrodes with and without water.

Table D.1: Calculated lattice parameters from Rietveld refinements in Figure C4

		a (Å)	c (Å)
AB60	Al	4.071	-
	Bi	4.543	11.851
AB40	Al	4.063	-
	Bi	4.536	11.841

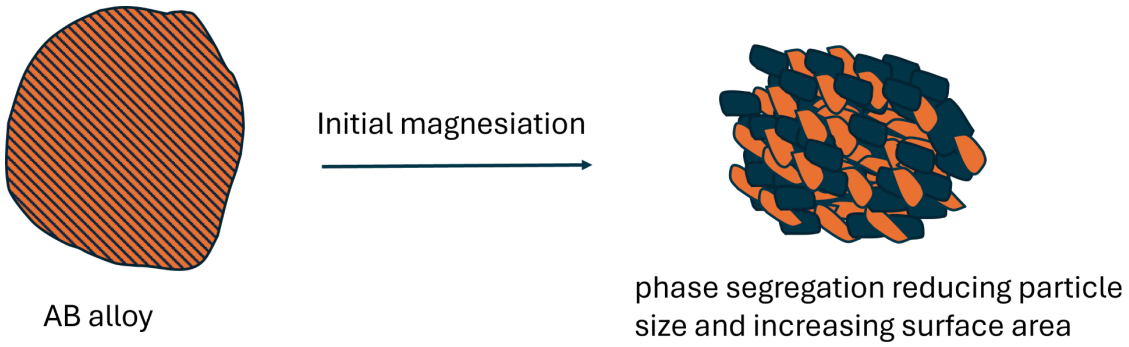

Figure D.1: Cartoon illustrating phase segregation of an "AB" alloy into distinct Mg_xA_y and Mg_wB_v intermetallics upon magnesiation

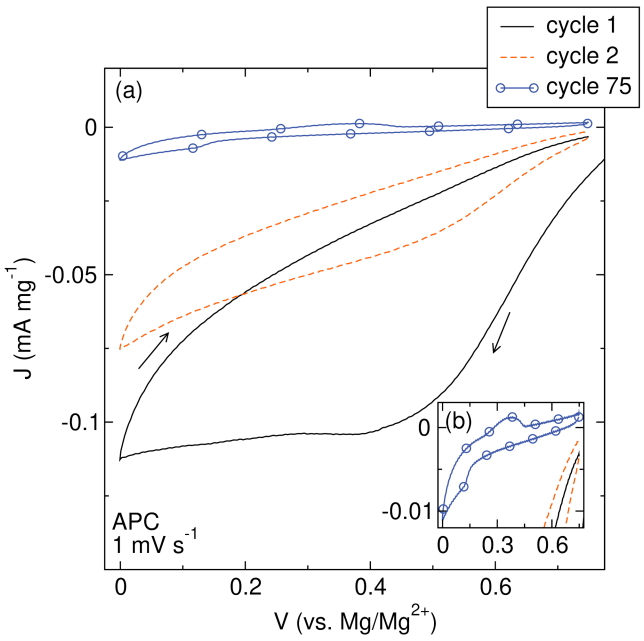

Figure D.2: First, second, and seventy-fifth cyclic voltammograms of an Al powder composite electrode with the APC electrolyte. CE: Mg, RE: Mg. 1 mV s^{-1} No Faradaic features are observed on cycles 1 or 2. After several cycles, a reduction occurs around 0.11 V. This feature is paired with an oxidation around 0.375 V. These features show very low current densities.

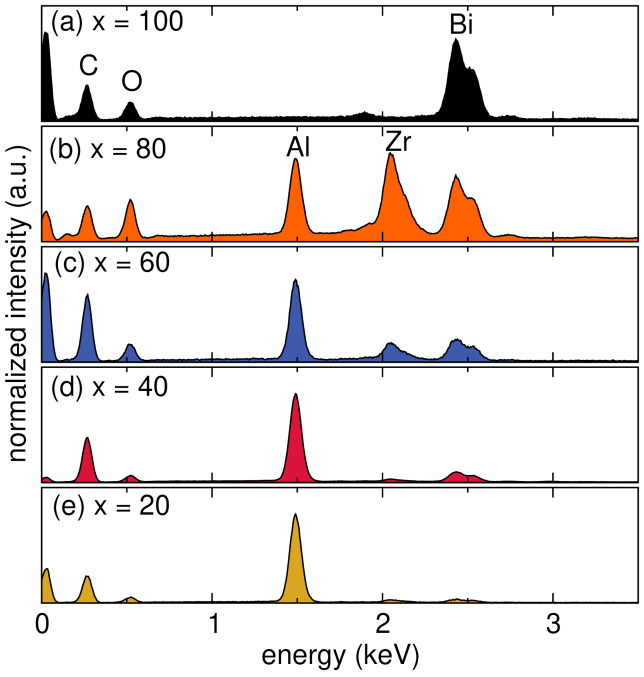

Figure D.3: EDS spectra for the ABX ($20 \leq x \leq 100$) alloy series. (a) Bi, (b) AB80, (c) AB60, (d) AB40, (e) AB20. The Zr impurity trends with Bi concentration in milled alloys.

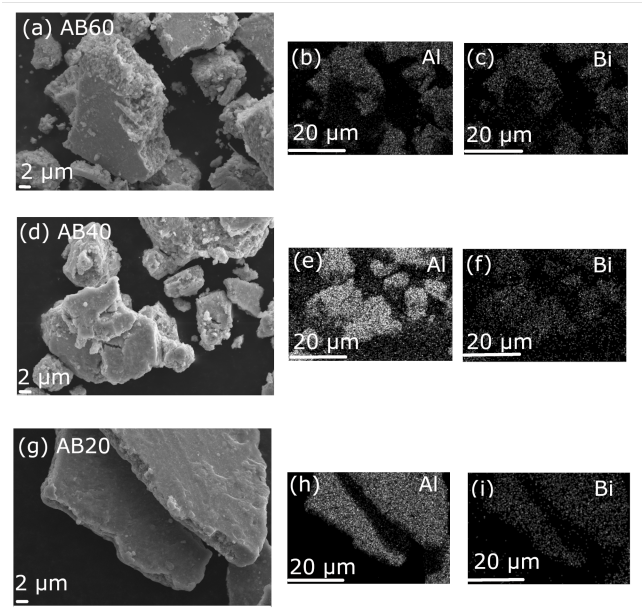

Figure D.4: SEM micrographs and corresponding Al and Bi EDS maps for (a, b, c) AB60, (d, e, f) AB40, and (g, h, i) AB80. All compositions show a homogenous distribution of Al and Bi on the micron scale.

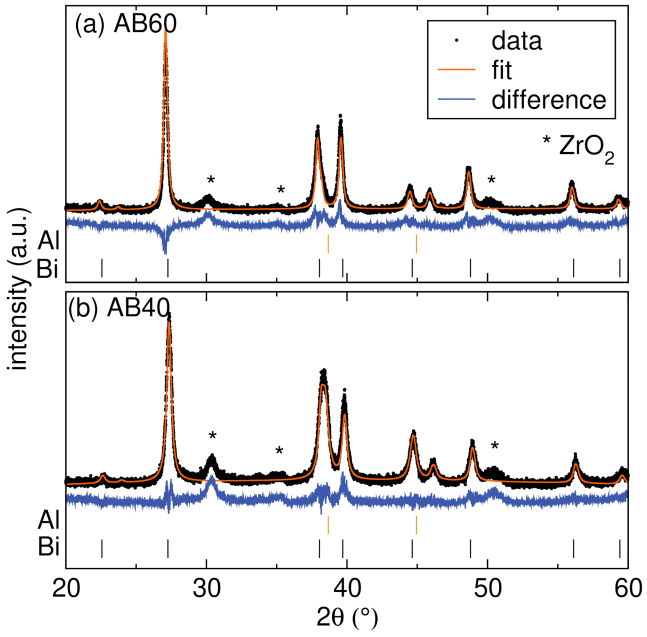

Figure D.5: Rietveld refinements for (a) AB40 and (b) AB60 fitting to distinct Al and Bi phases with reflections for Al and Bi indicated.

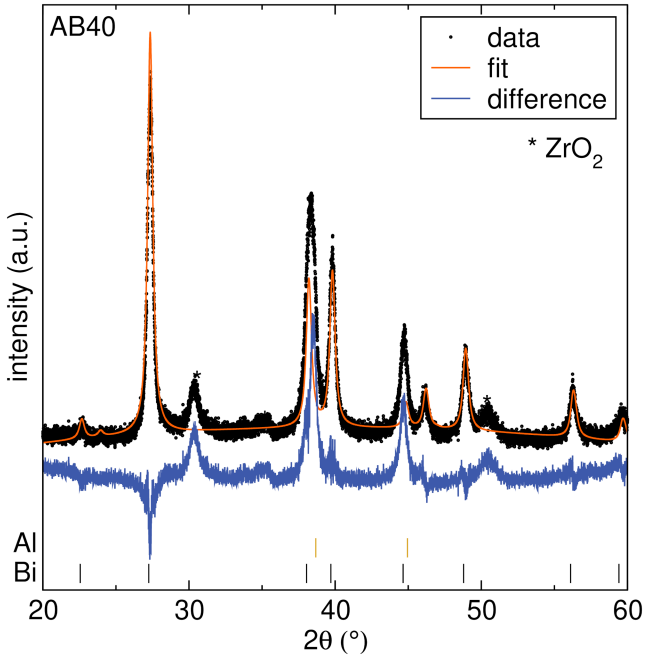

Figure D.6: Rietveld refinements for AB40 fitting to a single Bi phase with reflections for Al and Bi indicated.

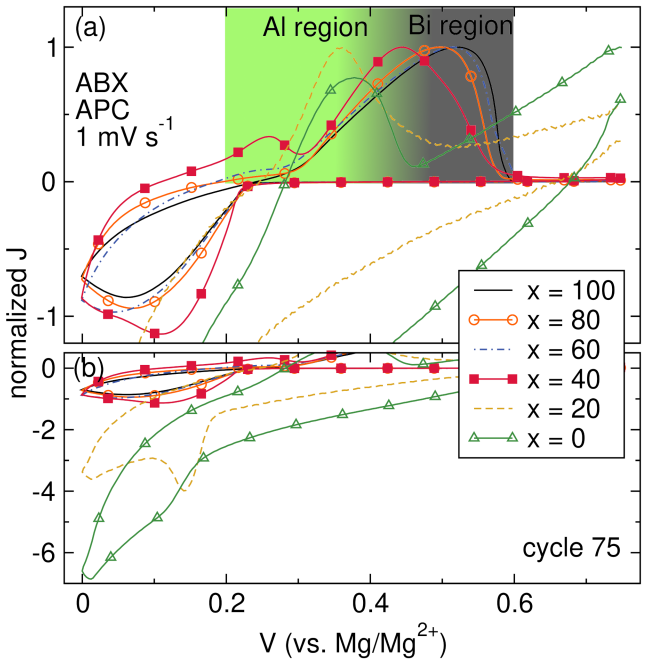

Figure D.7: (a) Cyclic voltammograms of ABX ($0 \leq x \leq 100$) with the APC electrolyte at 1 mV s^{-1} with current densities normalized to peak oxidative current (b) the same curves highlighting the cathodic region.

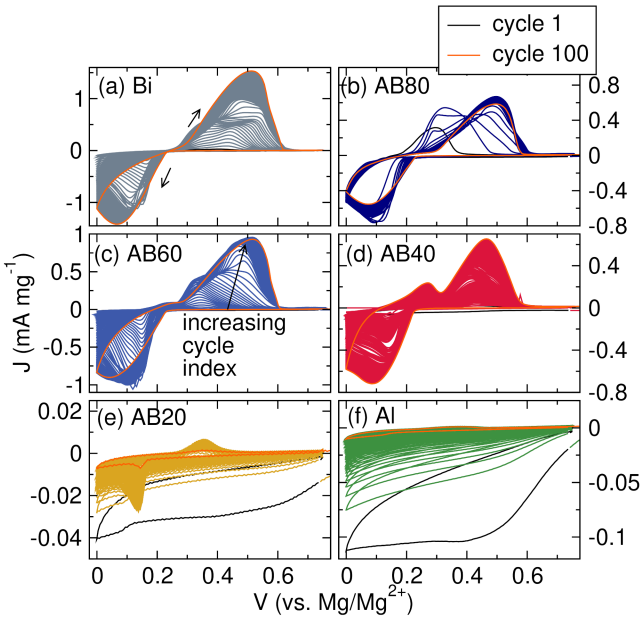

Figure D.8: Cyclic voltammograms of ABX ($0 \leq x \leq 100$) with the APC electrolyte at 1 mV s^{-1} showing cycles 1 - 100.

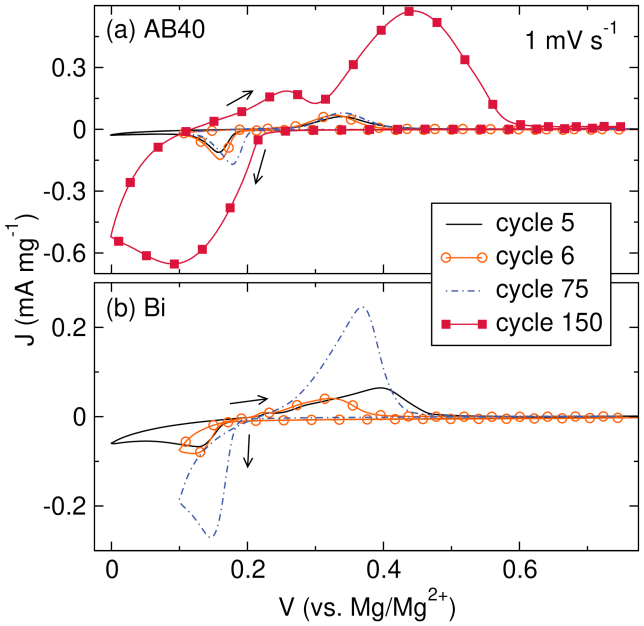

Figure D.9: (a) Selected cyclic voltammograms of AB40 and (b) Bi at 1 mV s^{-1} with the APC electrolyte and varied lower voltage cutoffs: cycles 1-5: 0 V - 0.75 V; cycles 6-75: 0.1 V - 0.75 V; and cycles 76-150: 0 V - 0.75 V.

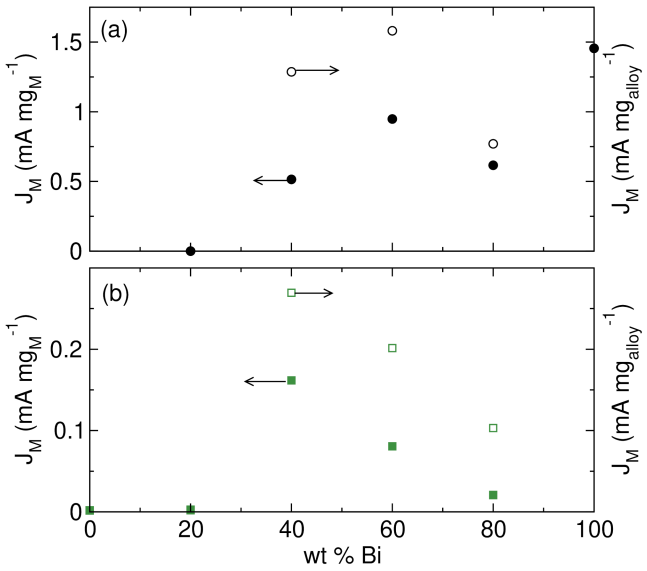

Figure D.10: Peak current densities for (a) Mg-Bi and (b) Mg-Al dealloying. Values of x $\geq$ 40 display enhanced activity in the Mg-Al region. Mg-Bi current density varies directly with Bi content.

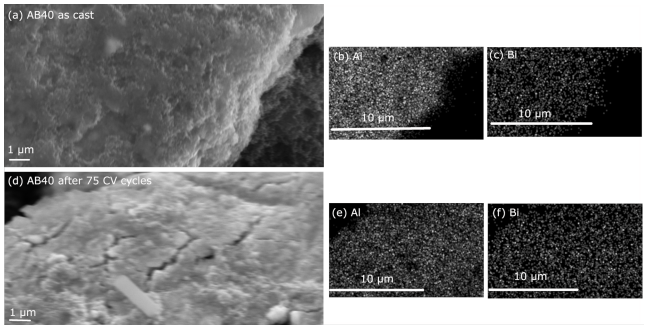

Figure D.11: SEM micrographs and corresponding EDS maps for Al and Bi of AB40 (a - c) as cast and (d - f) after 75 CV cycles. Phase separation is not evident on the micron scale.

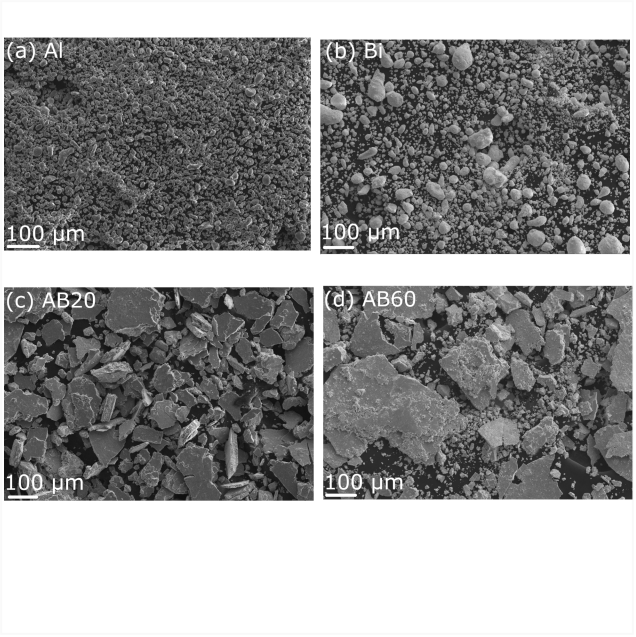

Figure D.12: SEM micrographs of (a) Al as received, (b) Bi as received, (c) AB20 milled 20 hours, and (d) AB60 milled 20 hours. The precursor metal powders have a lower average surface area than the milled alloys.

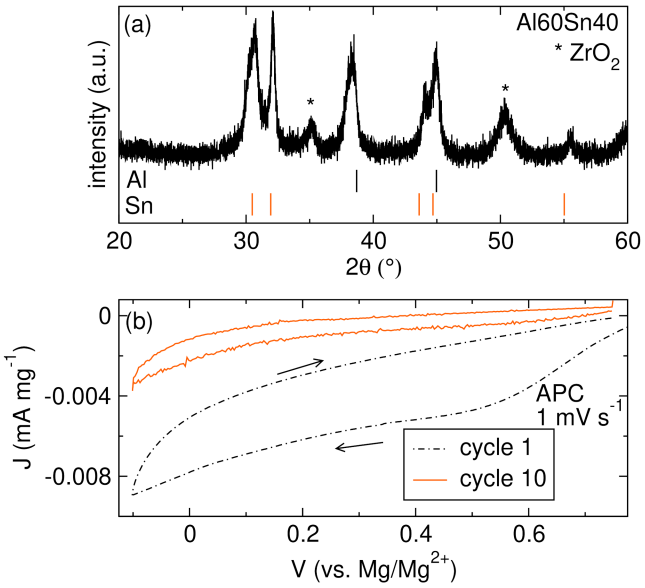

Figure D.13: (a) XRD pattern of Al60Sn40 milled 20 hours with reflections for Al and Sn indicated and (b) first and tenth cyclic voltammograms of Al60Sn40 with the APC electrolyte at 1 mV s^{-1}. No Faradaic features are observed throughout cycling.

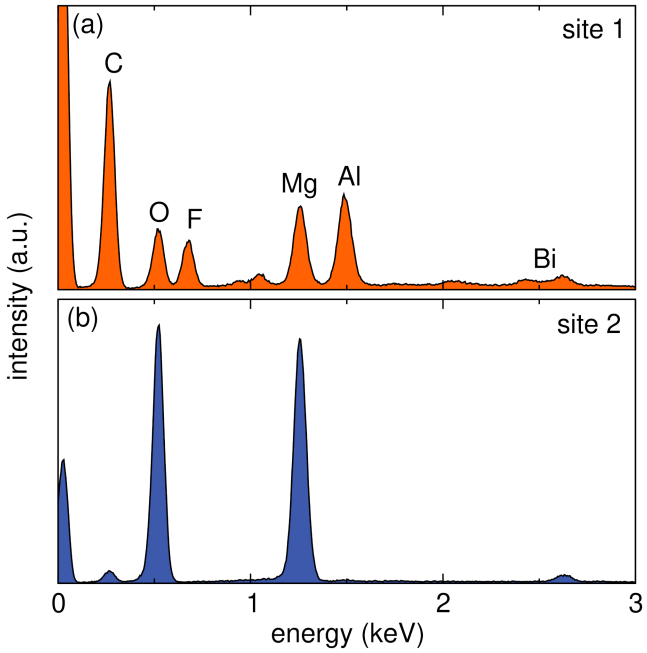

Figure D.14: EDS spectra for (a) site 1 and (b) site 2 of an AB40 electrode reduced at C/100 for 100 hours.

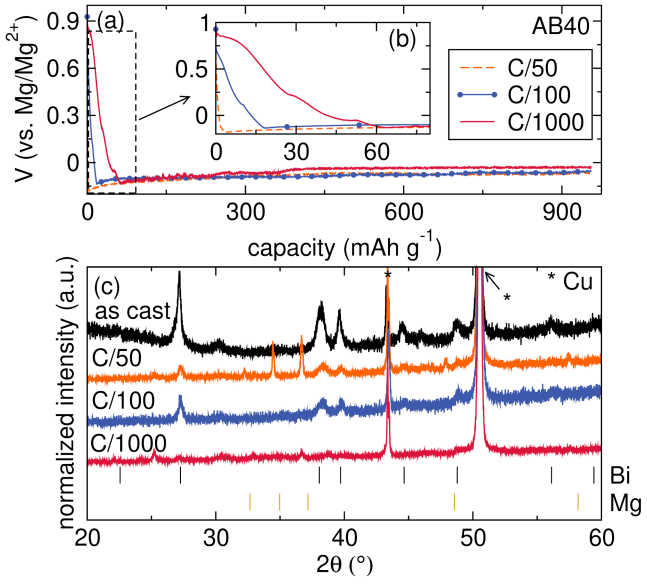

Figure D.15: (a) Galvanostatic traces of AB40 reduced at various rates and (b) corresponding ex situ XRD patterns of the same electrodes with reflections for Bi and Mg indicated.

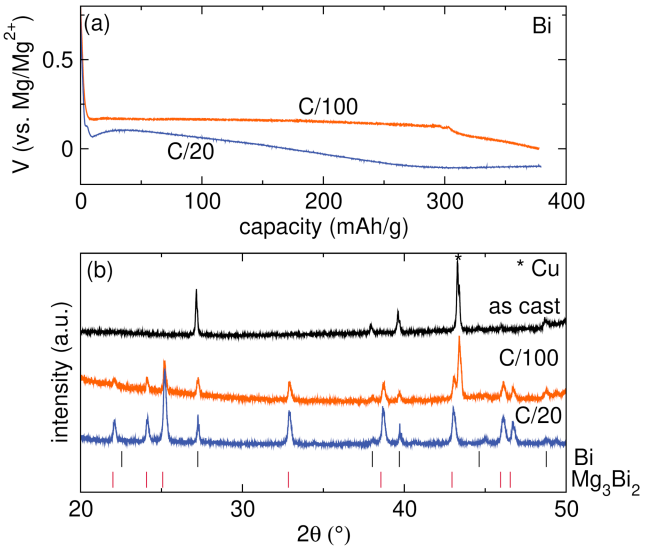

Figure D.16: (a) Chronopotentiometry trace of a Bi electrode reduced at C/100 and C/20 with the APC electrolyte and (b) ex situ XRD patterns of the reduced electrodes presented with that of the as prepared electrode for reference. Reflection positions for Bi and Mg_3Bi_2 are indicated.

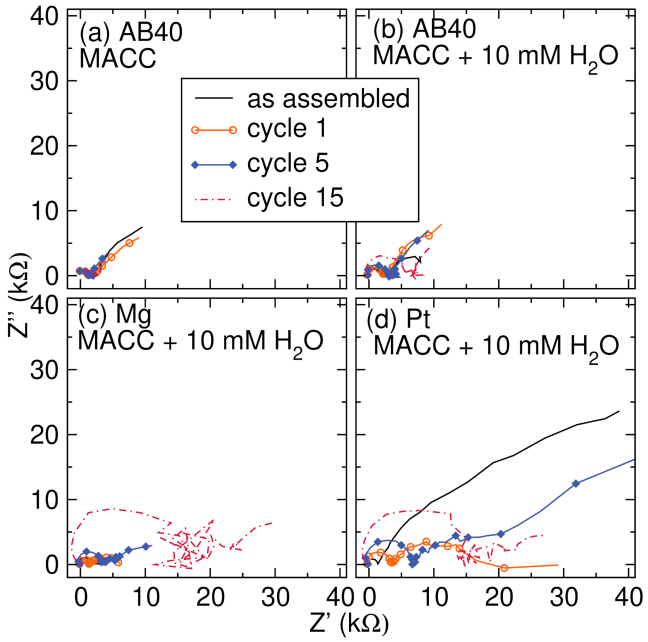

Figure D.17: Selected EIS spectra measured following a 60s OCV rest after the working electrode potential is swept to the lower voltage cutoff for (a) an AB40 working electrode in MACC and (b) AB40, (c) Mg, and (d) Pt working electrodes in MACC + 10 mM H_2O. Following EIS, the potential is swept positive to 0.75 V, and the process is repeated.

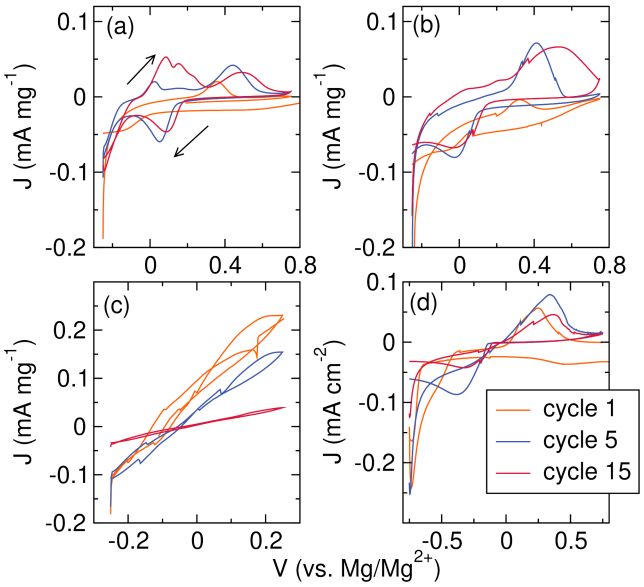

Figure D.18: Selected cyclic voltammograms for (a) an AB40 working electrode in MACC and (b) AB40, (c) Mg, and (d) Pt working electrodes in MACC + 10 mM H_2O.